

REPORT DOCUMENTATION PAGE

AFRL-SR-BL-TR-01-

Public reporting burden for this collection of information is estimated to average 1 hour per response, including gathering and maintaining the data needed, and completing and reviewing the collection of information. Send collection of information, including suggestions for reducing this burden, to Washington Headquarters Service, Paperwork Project, Suite 1204, Arlington, VA 22202-4302, and to the Office of Management and Budget, Paperwork Project, Suite 1204, Arlington, VA 22202-4302.

0464

Source,
of this
person

1. AGENCY USE ONLY (Leave blank)		2. REPORT DATE June 15, 2001		3. REPORT TYPE AND DATES COVERED FINAL 1 AUG 2000-15 JUN 2001	
4. TITLE AND SUBTITLE New Directions in Mask Engineering				5. FUNDING NUMBERS F49620-00-C-0032	
6. AUTHOR(S) Eytan Barouch, David Chrin, Stephen Knodie Steven Orszag, Michael Yeung					
7. PERFORMING ORGANIZATION NAME(S) AND ADDRESS(ES) Cambridge Hydrodynamics, Inc. P.O. Box 1403 Princeton NJ 08742				8. PERFORMING ORGANIZATION REPORT NUMBER	
9. SPONSORING / MONITORING AGENCY NAME(S) AND ADDRESS(ES) Air Force Office of Scientific Research 801 N. Randolph St. Arlington, VA 22203-1977				10. SPONSORING / MONITORING AGENCY REPORT NUMBER	
11. SUPPLEMENTARY NOTES					
12a. DISTRIBUTION / AVAILABILITY STATEMENT Unlimited - Unclassified				12b. DISTRIBUTION CODE	
13. ABSTRACT (Maximum 200 words) The scattering of electromagnetic waves from complex objects coated with lossy materials with negative and positive permittivity embedded in a layered medium is analyzed via new formulations, and a new set of algorithms to implement these formulations is introduced. This new technology is applied here to phase shifted photomasks. The results for various wavelengths and mask thicknesses have been considered carefully and are reported here. <div style="text-align: right; font-size: 2em; font-weight: bold;">20011005 142</div>					
14. SUBJECT TERMS Electromagnetics Lossy materials Permittivity Phase-shifted photomasks Integral equations Green's function Scattering Photolithography				15. NUMBER OF PAGES 77	
				16. PRICE CODE	
17. SECURITY CLASSIFICATION OF REPORT Unclassified	18. SECURITY CLASSIFICATION OF THIS PAGE Unclassified	19. SECURITY CLASSIFICATION OF ABSTRACT Unclassified	20. LIMITATION OF ABSTRACT SAR		

New Directions in Mask Engineering

- A Final Report to the AFOSR/DARPA Under Contract No. F49620-00-C-0032 -

by

Eytan Barouch, David Chrin, Stephen Knodle
Steven Orszag, Michael Yeung

June 2001

Cambridge Hydrodynamics, Inc.
P. O. Box 1403
Princeton, NJ 08542

NEW DIRECTIONS IN
MASK TRANSMISSION ENGINEERING

A FINAL REPORT TO AFOSR/DARPA
CONTRACT NO. F49620-00-C-0032

CAMBRIDGE HYDRODYNAMICS, INC.
PO Box 1403
PRINCETON, NJ 08542

ABSTRACT

The scattering of electromagnetic waves from complex object coated with lossy materials with negative and positive permittivity embedded in a layered medium is analysed via a new formulation, and a new set of algorithms to implement these formulations is introduced. This new technology is applied here to phase shifted photomasks. The results for various wavelengths and mask thicknesses have been considered carefully and are reported here.

1. INTRODUCTION

The problem of accurately computing the electromagnetic scattering from lossy, dispersive objects of complex shapes embedded in a layered dispersive medium has been outstanding for quite some time, despite the large range of potential military applications. These applications include the detection and identification of targets located under a foliage covered earth or airborne targets over the horizon. The difficulties associated with such problems in part originate from the need to model the shapes and inhomogeneities of the objects accurately while simultaneously keeping computational complexity to a manageable level.

The classic finite-difference time-domain (FDTD) method and finite-element method (FEM) are inadequate for addressing the above mentioned difficulties. This is because FDTD requires a regular computational grid and is therefore not suitable for modeling curved surfaces accurately. On the other hand, FEM can model curved surfaces accurately, but requires the inversion of a large matrix, which is computationally expensive for large problems.

For mask and wafer analysis, in part due to the periodicity of some structures like contact holes and in part due to features complexity, we have elected to employ a new formulation of the basic problem to enhance the necessary hybrid method for such complex problems. The "single integral equation" method was originally based on the scalar Green's function. We have reformulated the "single integral equation" method based on the dyadic Green's functions for the layered wafer substrate. This approach allows each feature on the wafer to be treated as a localized object embedded in a layered medium, resulting in a smaller total number of unknowns along the profile (or surface) of the embedded scattering object only. Furthermore, the dyadic Green's functions for a

given layered structure, wavelength and periodicity need to be computed only once. The results are stored in interpolation tables for use on different feature shapes. This leads to a particularly efficient methodology for investigating the effect of change of the feature shape on the diffraction efficiency for fixed layered structure, wavelength and periodicity, presenting a very powerful tool for generating libraries for the desired analysis.

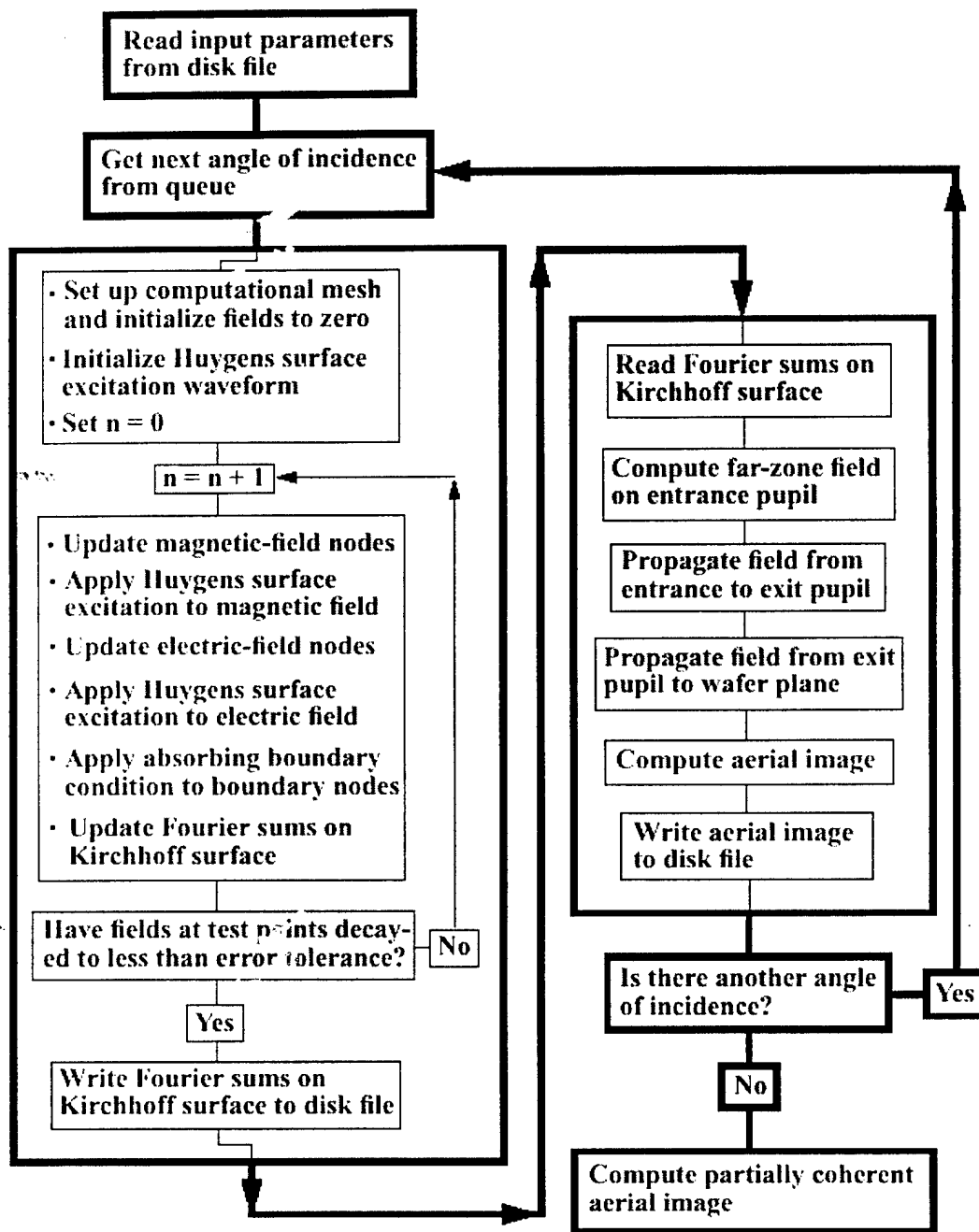
The embedded object representing the photoresist feature under study behaves like a cavity trapping an oscillatory wave, enabling the generation of a resonance. This resonance expresses itself in various ways, such as a vanishing eigenvalue or a discontinuous derivative, leading to a potentially non-unique solution for some specific frequencies. The "single integral equation" can be formulated in terms of either the electric field or the magnetic field expression, the two formulations being completely equivalent in determining the fields. However, a unique solution of all frequencies, including the resonant frequencies of the embedded object representing the wafer feature under study, is obtained by employing a linear combination of the magnetic-field and electric-field expressions.

We have demonstrated the formulation stability for all frequencies, as well as the potential pitfalls associated with naïve coding ignoring this most subtle point. We demonstrate these considerations on several test pattern of photoresist structure.

This report is organized as follows:

1. In the remainder of this Section, a program flowchart and vertical versus horizontal critical dimension results are presented (numerical data, intensity plots, and aerial images).
2. In Section 2, a basic formulation of the problem is presented.
3. In the Appendix, a preprint of the paper, "Application of the Hybrid Finite-Difference Time-Domain Method to Modeling Curved Surfaces in Three-Dimensional Lithography Simulation" is presented for background on the present approach.

PROGRAM FLOW CHART



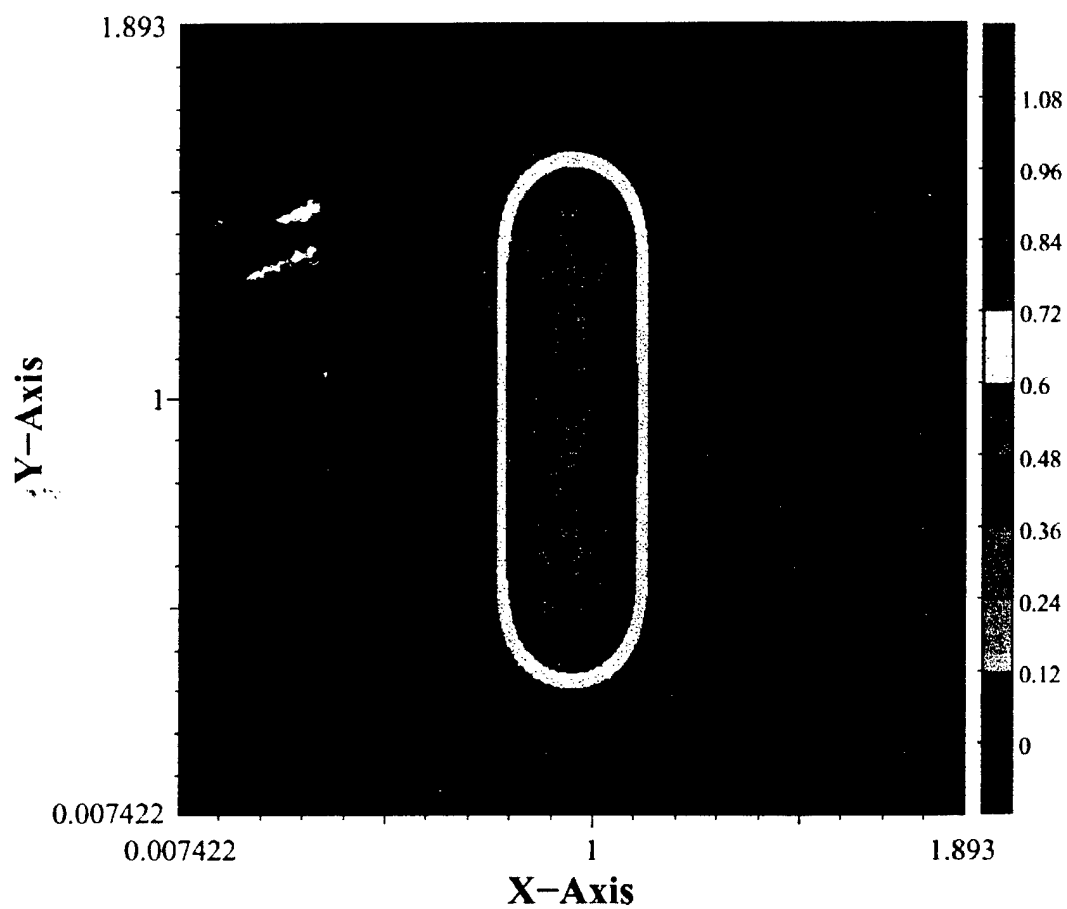
Vertical versus Horizontal CD Nominal CD = $157/2 = 78.5$ nm				
Dark Field				
	(Circular light)-Mask-QWP-Analyzer-QWP		(Y light)-Mask-Analyzer-QWP	
	CD	Threshold	CD	Threshold
Vertical line	78.5 nm	0.2114	78.5 nm	0.2198
Horizontal line	79.1 nm	0.2114	72.4 nm	0.2198
Bright Field				
	(Circular light)-Mask-QWP-Analyzer-QWP		(Y light)-Mask-Analyzer-QWP	
	CD	Threshold	CD	Threshold
Vertical line	78.5 nm	0.4524	78.5 nm	0.4501
Horizontal line	77.8 nm	0.4524	75.3 nm	0.4501

Vertical versus Horizontal CD 110 nm by 660 nm isolated feature 193 nm wavelength						
Chromium Thickness = 85 nm Defocus = 0						
	Circular		TE		TM	
	CD	Threshold	CD	Threshold	CD	Threshold
Vertical line	70.0 nm	0.3330	70.0 nm	0.3370	70.0 nm	0.3316
Horizontal line	69.0 nm	0.3330	71.6 nm	0.3370	66.7 nm	0.3316
Chromium Thickness = 97 nm Defocus = 0						
	Circular		TE		TM	
	CD	Threshold	CD	Threshold	CD	Threshold
Vertical line	70.0 nm	0.3276	70.0 nm	0.3322	70.0 nm	0.3264
Horizontal line	68.9 nm	0.3276	71.8 nm	0.3322	66.4 nm	0.3264

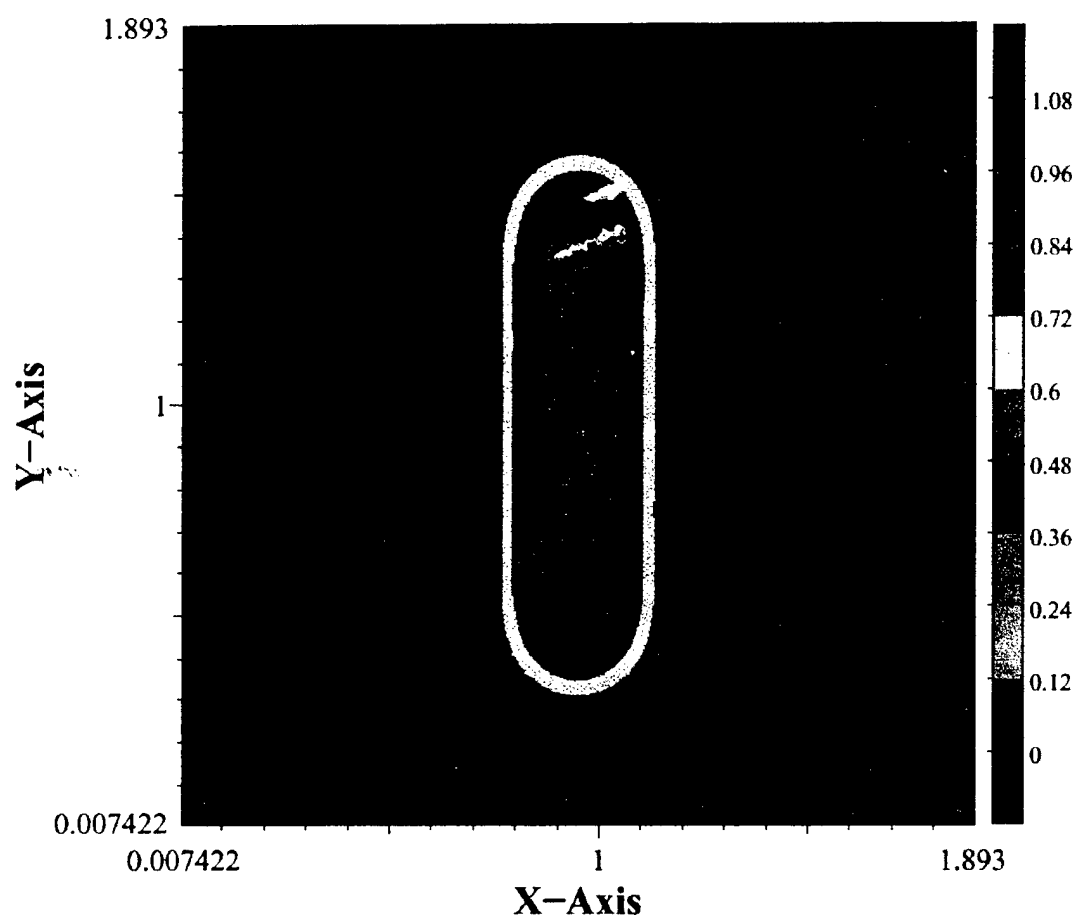
Vertical versus Horizontal CD 110 nm by 660 nm isolated feature 193 nm wavelength						
Chromium Thickness = 85 nm Nominal CD = 70 nm						
Defocus = 0						
	Circular		TE		TM	
	CD	Threshold	CD	Threshold	CD	Threshold
Vertical line	70.0 nm	0.3334	70.0 nm	0.3370	70.0 nm	0.3316
Horizontal line	69.5 nm	0.3334	71.6 nm	0.3370	66.7 nm	0.3316
Defocus = 100 nm						
	Circular		TE		TM	
	CD	Threshold	CD	Threshold	CD	Threshold
Vertical line	65.1 nm	0.3334	68.7 nm	0.3370	61.8 nm	0.3316
Horizontal line	64.4 nm	0.3334	63.2 nm	0.3370	63.8 nm	0.3316
Defocus = 200 nm						
	Circular		TE		TM	
	CD	Threshold	CD	Threshold	CD	Threshold
Vertical line	17.8 nm	0.3334	--	0.3370	--	0.3316
Horizontal line	15.7 nm	0.3334	--	0.3370	26.3 nm	0.3316

Vertical versus Horizontal CD 190 nm by 1140 nm isolated feature 248 nm wavelength				
Chromium Thickness = 100 nm Nominal CD = 140 nm				
Defocus = 0				
	Circular		Linear	
	CD	Threshold	CD	Threshold
Vertical line	140.0 nm	0.2513	140.0 nm	0.2423
Horizontal line	139.8 nm	0.2513	125.0 nm	0.2423
Defocus = 100 nm				
	Circular		Linear	
	CD	Threshold	CD	Threshold
Vertical line	147.7 nm	0.2513	146.1 nm	0.2423
Horizontal line	147.6 nm	0.2513	137.0 nm	0.2423
Defocus = 200 nm				
	Circular		Linear	
	CD	Threshold	CD	Threshold
Vertical line	146.6 nm	0.2513	143.1 nm	0.2423
Horizontal line	146.3 nm	0.2513	137.2 nm	0.2423
Defocus = 300 nm				
	Circular		Linear	
	CD	Threshold	CD	Threshold
Vertical line	135.8 nm	0.2513	129.6 nm	0.2423
Horizontal line	135.6 nm	0.2513	126.2 nm	0.2423
Defocus = 400 nm				
	Circular		Linear	
	CD	Threshold	CD	Threshold
Vertical line	107.6 nm	0.2513	93.8 nm	0.2423
Horizontal line	107.4 nm	0.2513	97.7 nm	0.2423

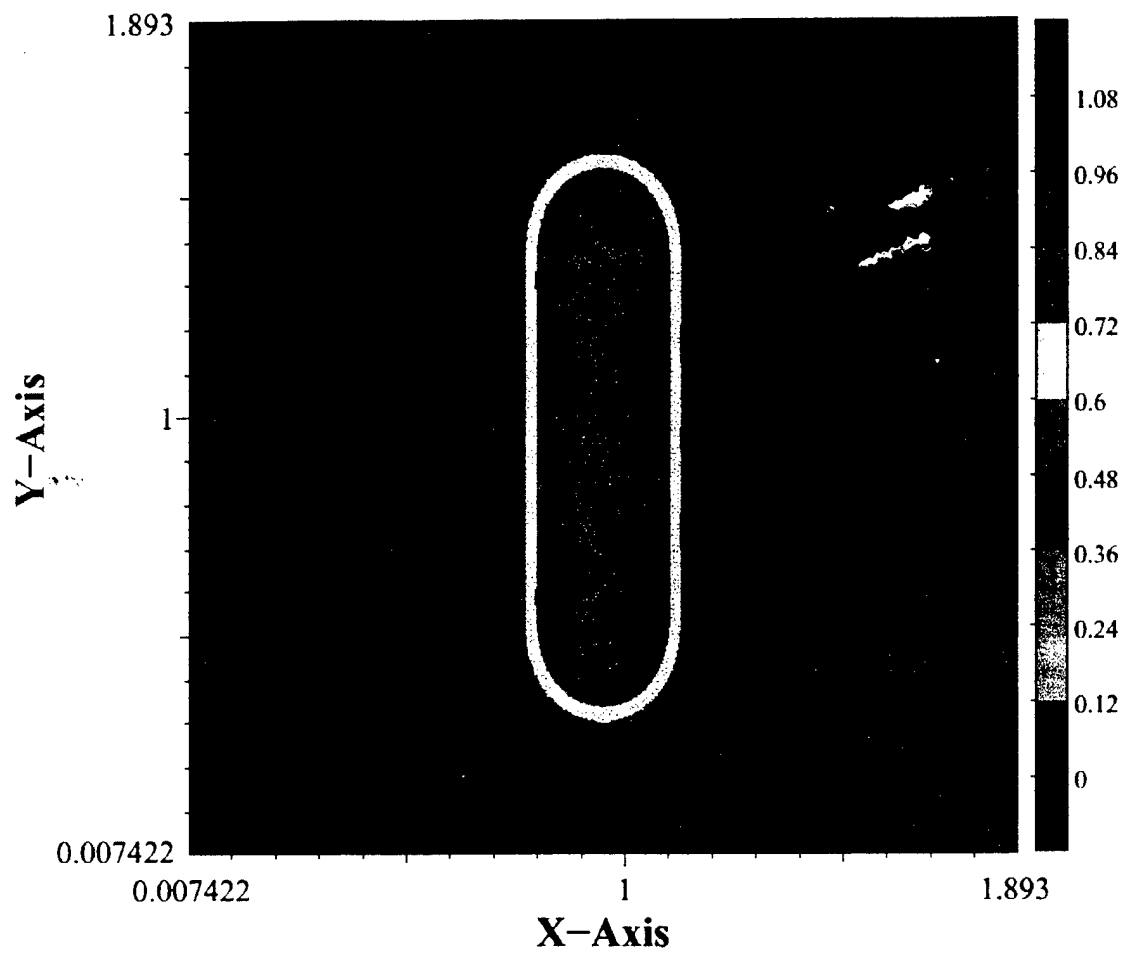
248 nm, Linear, Defocus = 400 nm



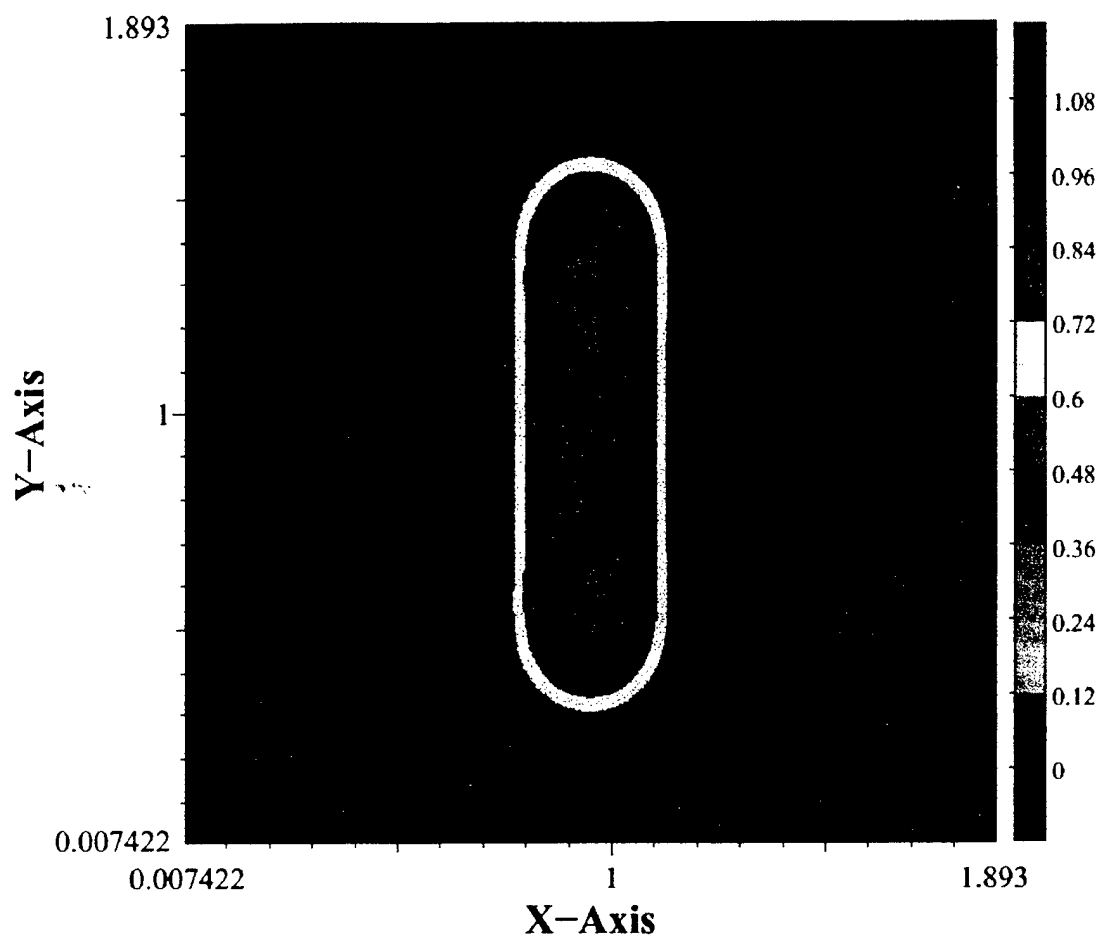
248 nm, Circular, Defocus = 400 nm



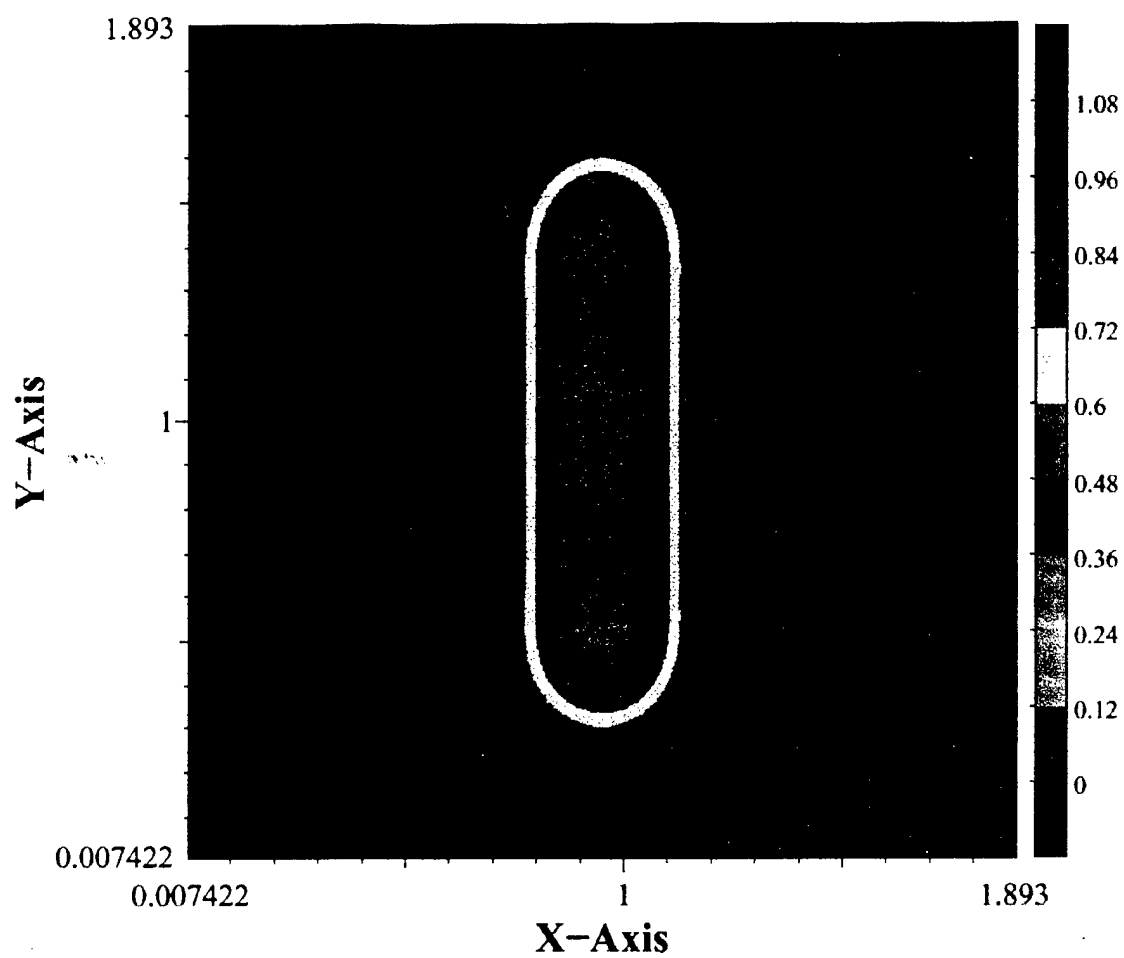
248 nm, Linear, Defocus = 300 nm



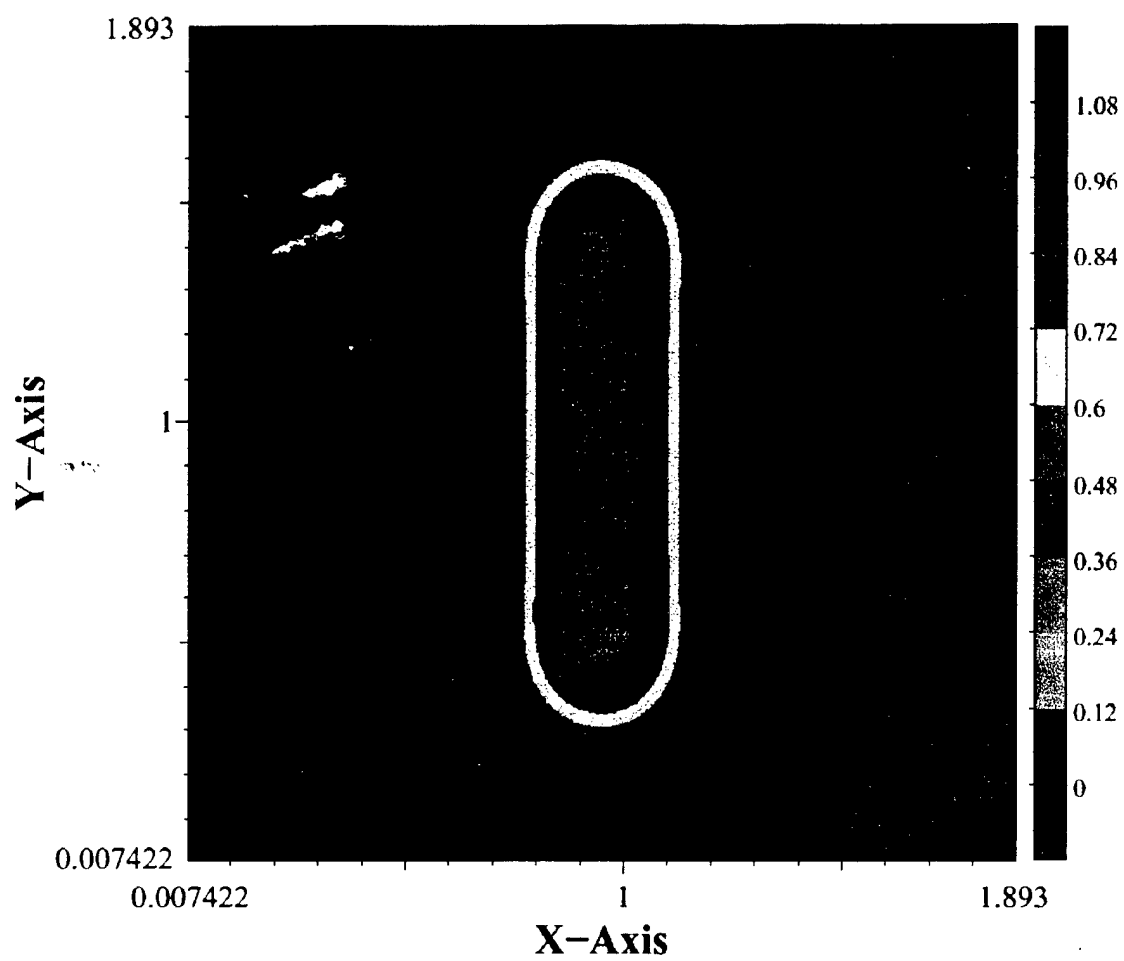
248 nm, Circular, Defocus = 300 nm



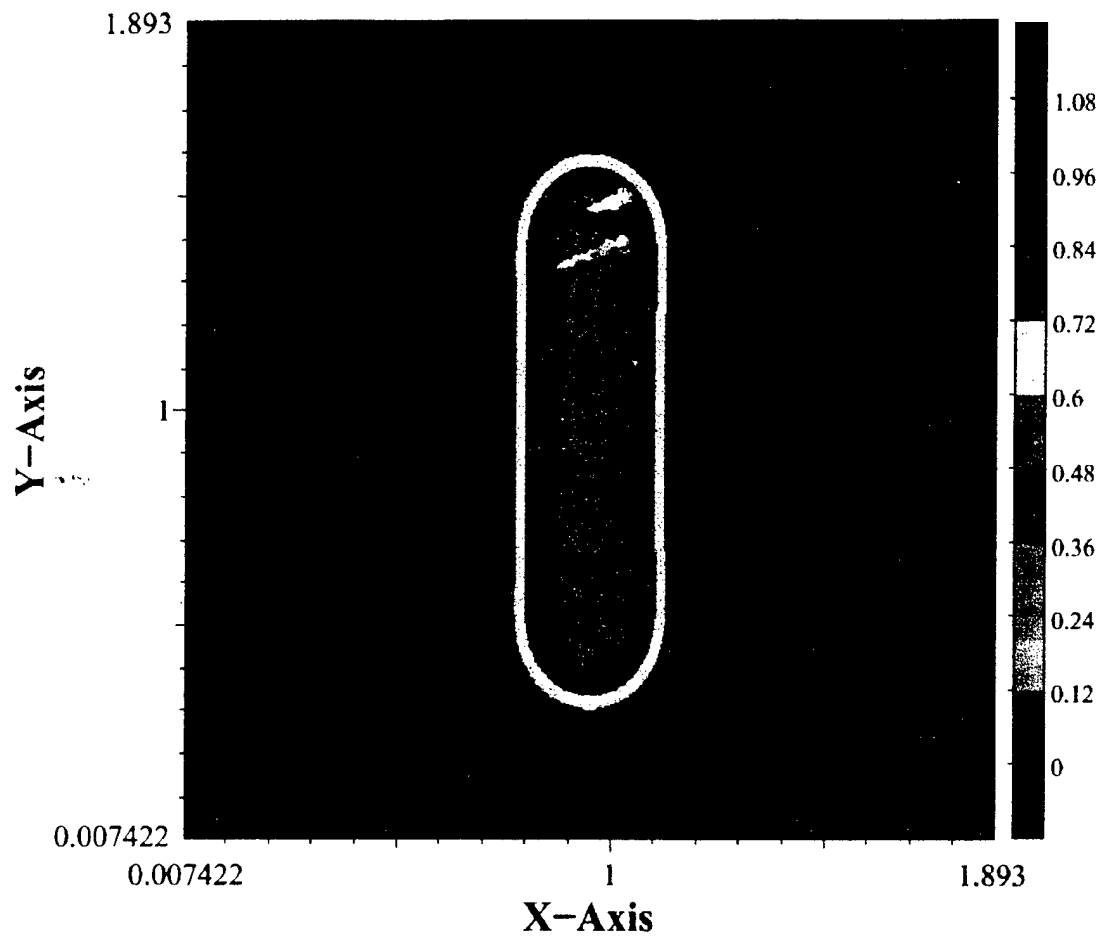
248 nm, Linear, Defocus = 200 nm



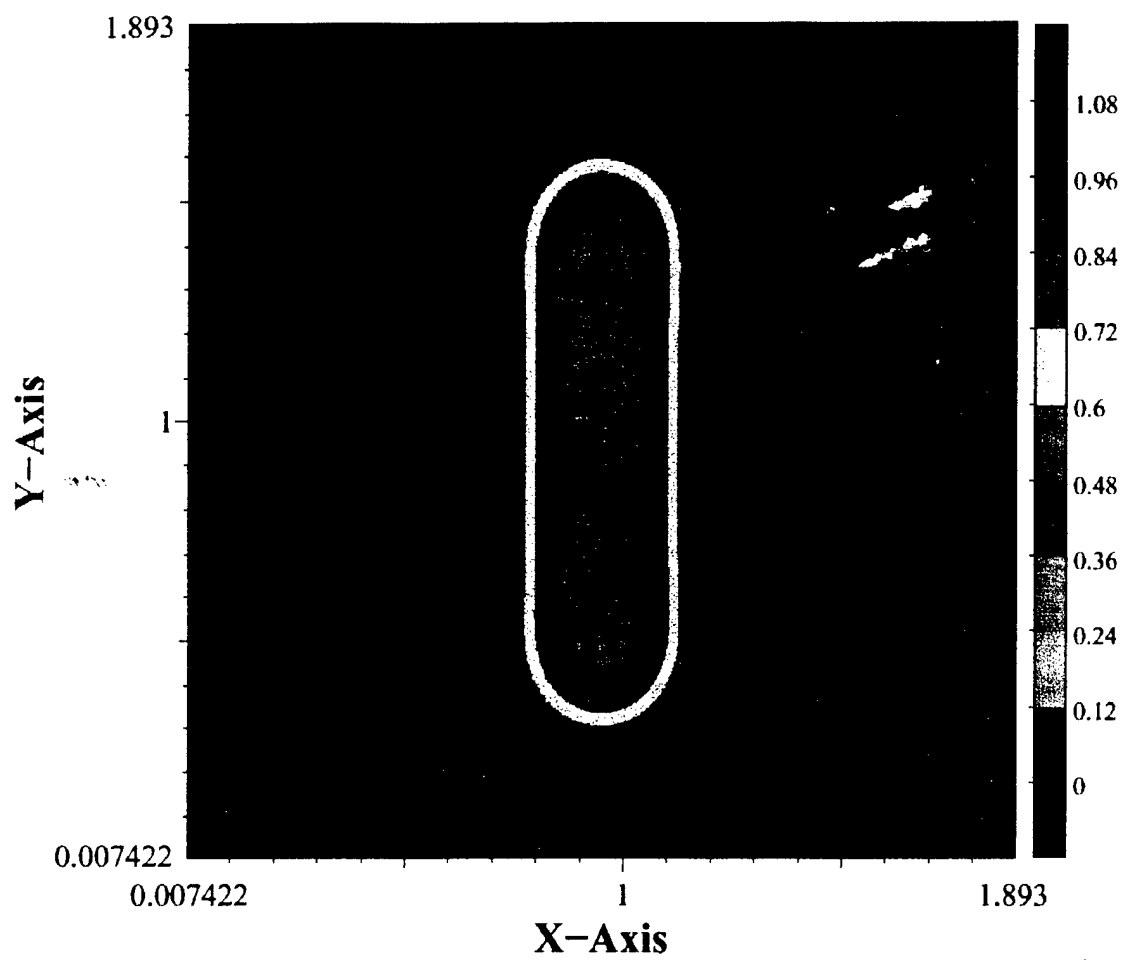
248 nm, Circular, Defocus = 200 nm



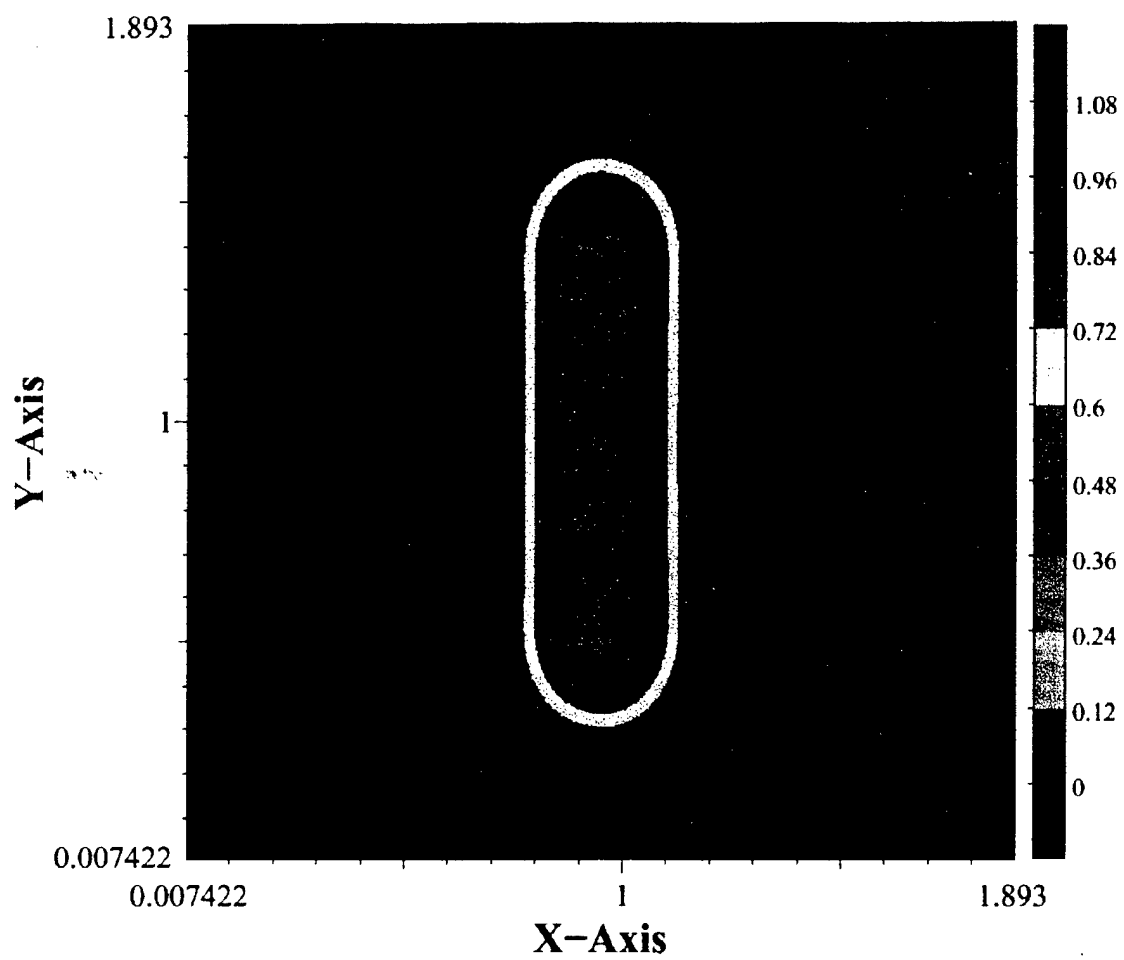
248 nm, Linear, Defocus = 100 nm



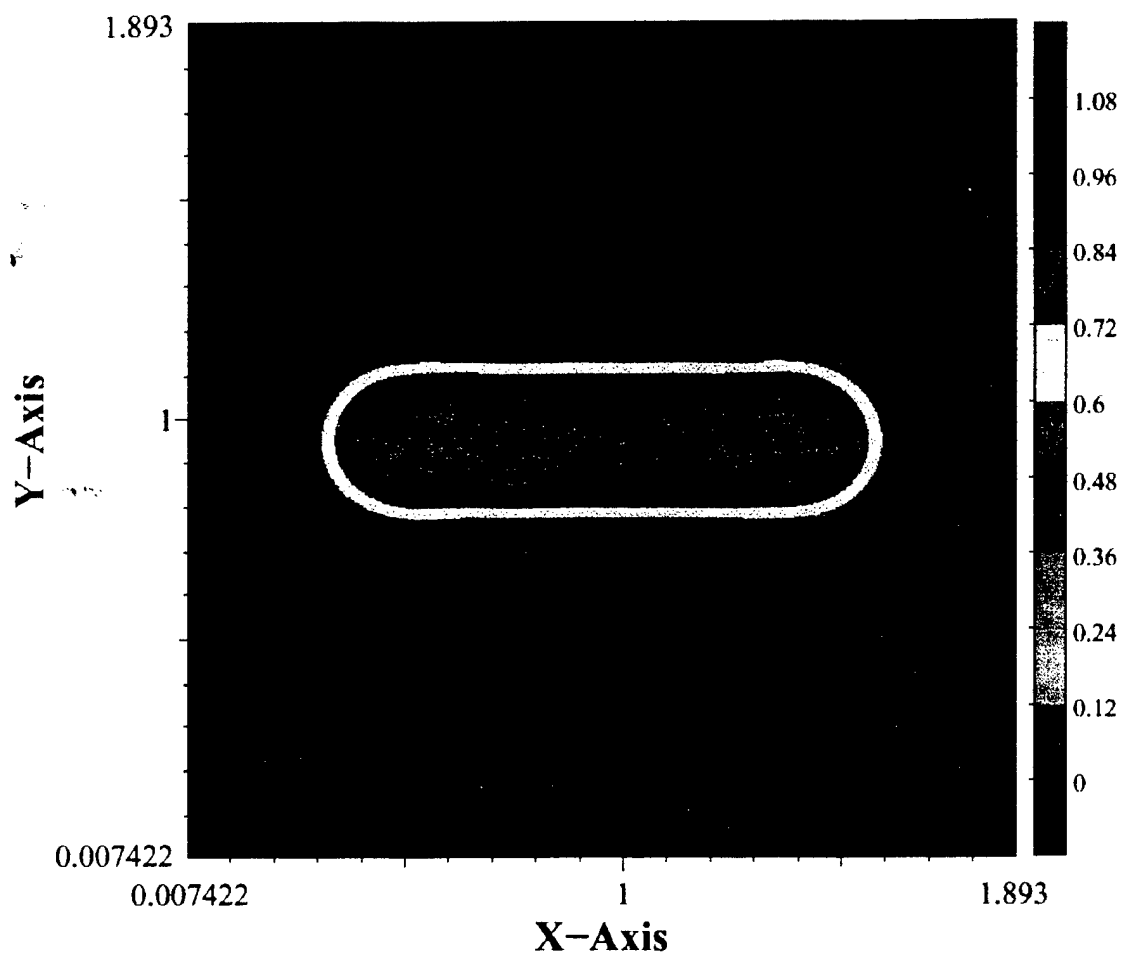
248 nm, Circular, Defocus = 100 nm



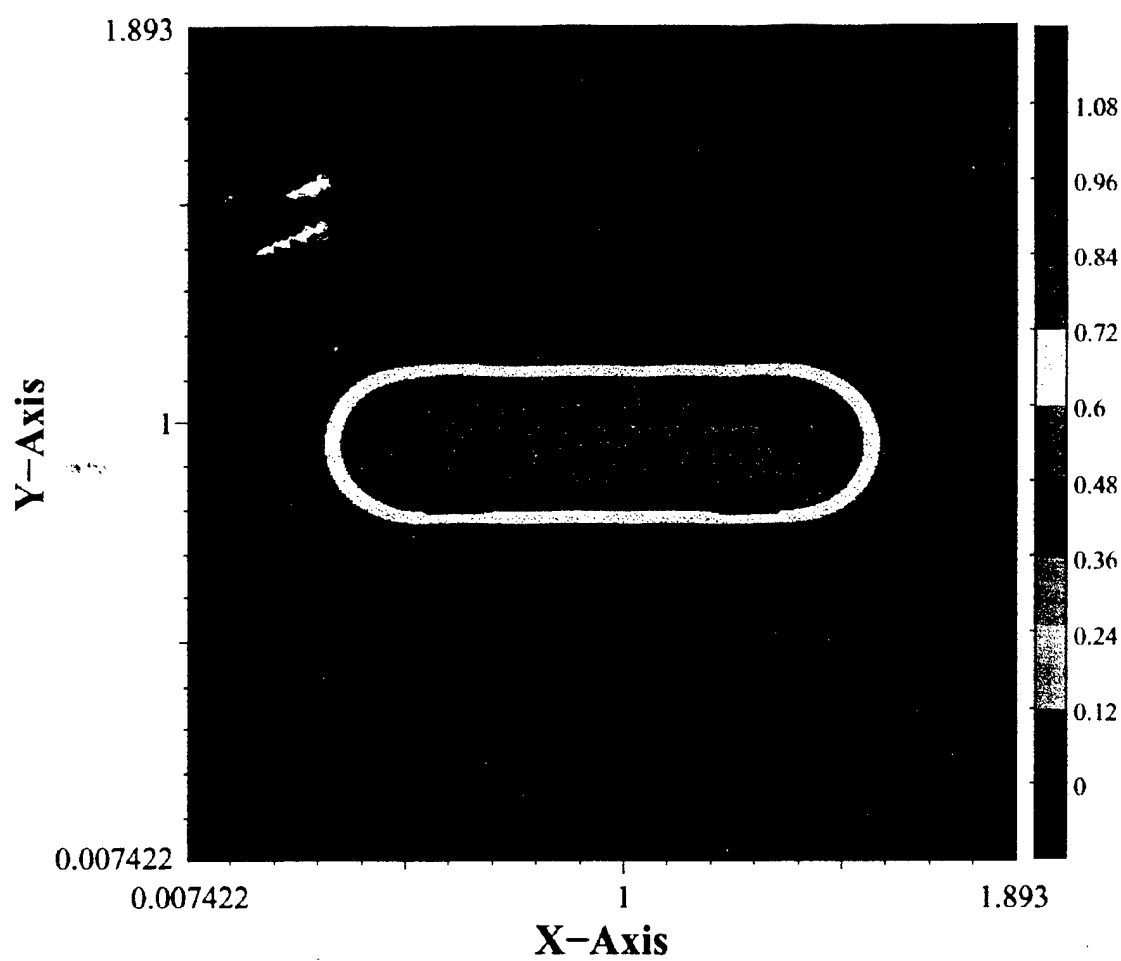
248 nm, Linear, Defocus = 0



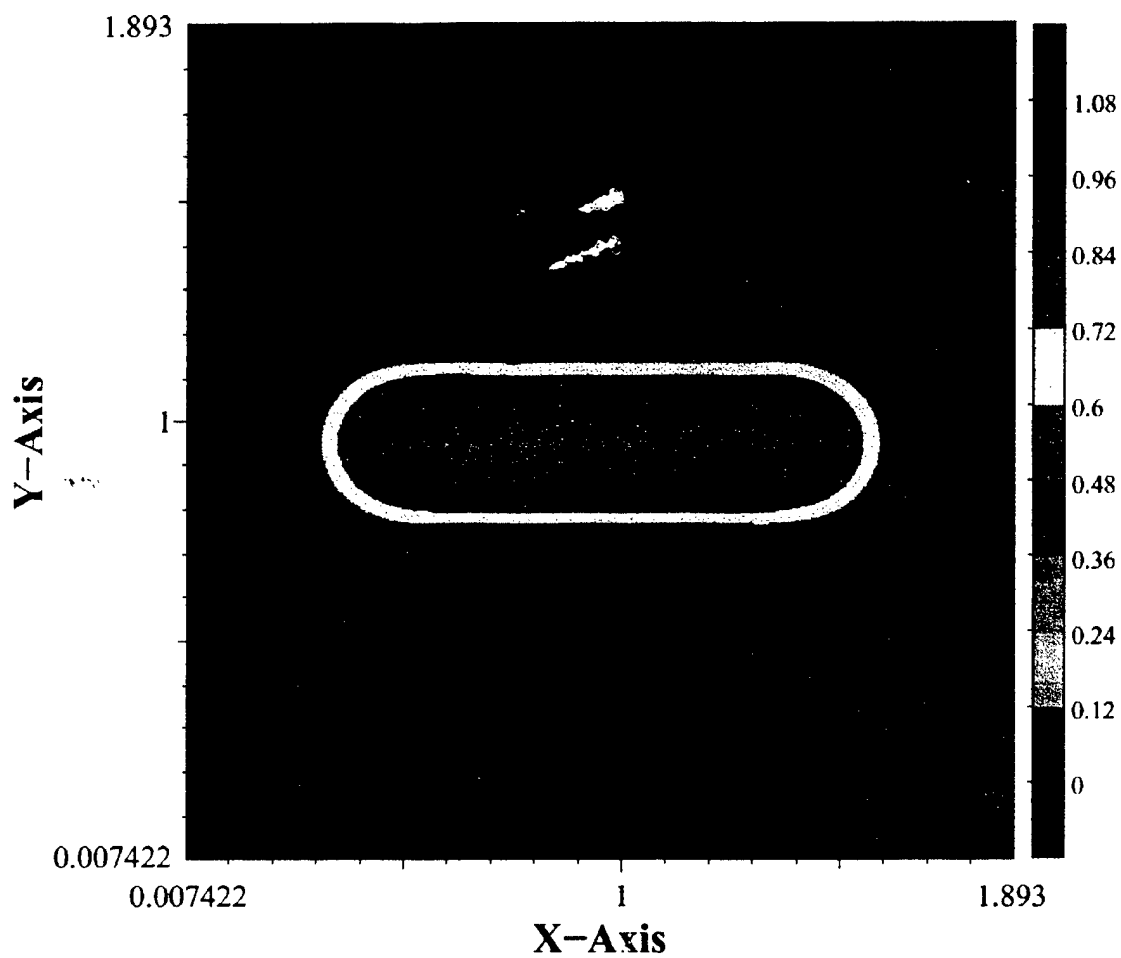
248 nm, Circular, Defocus = 0



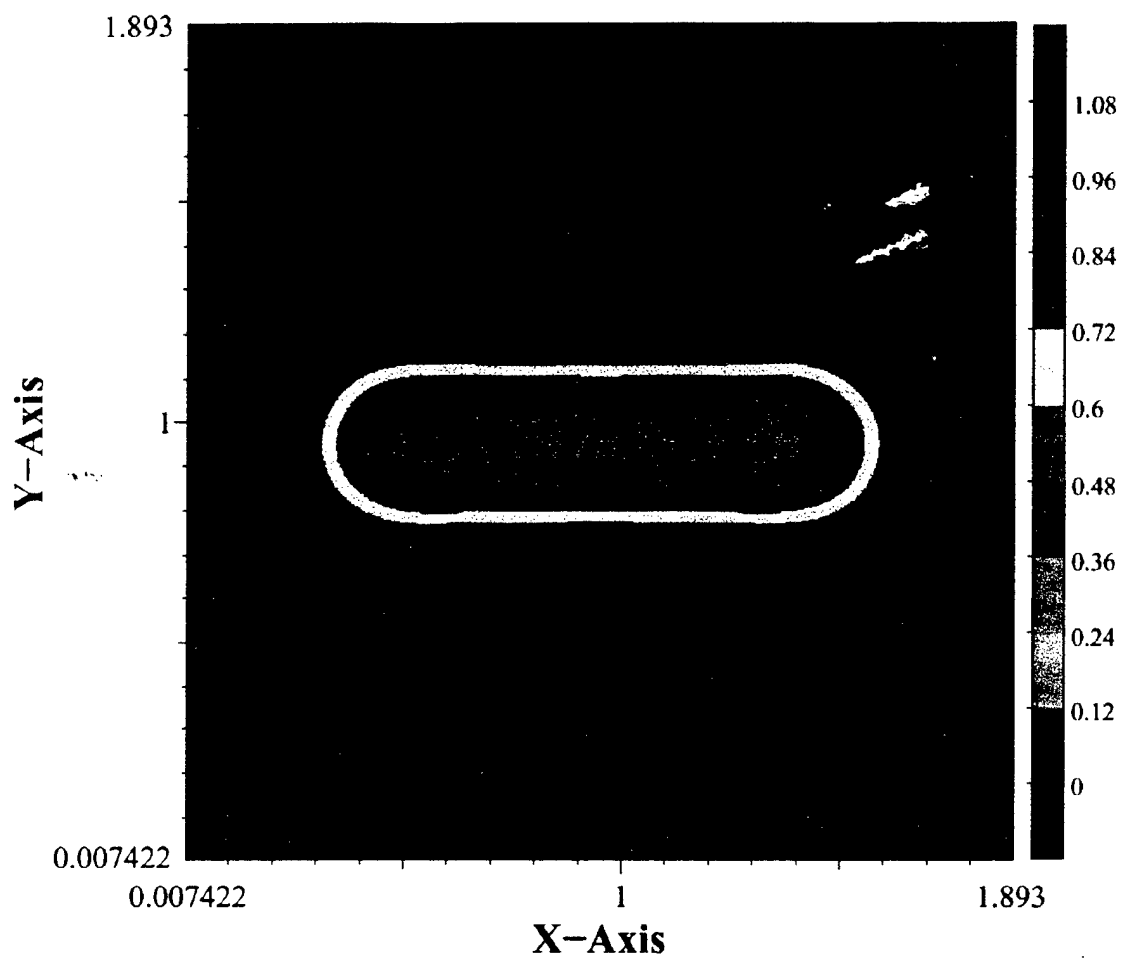
248 nm, Linear, Defocus = 400 nm



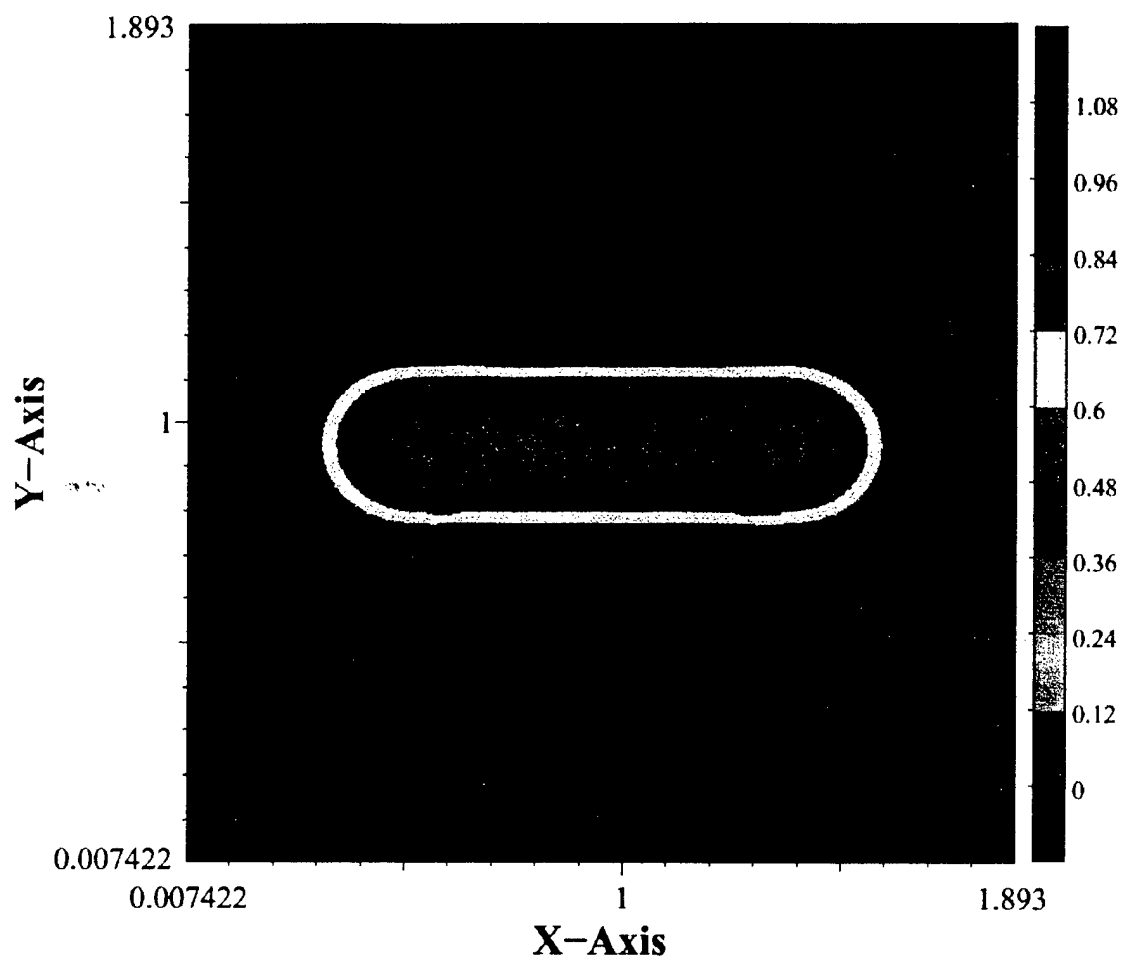
248 nm, Circular, Defocus = 400 nm



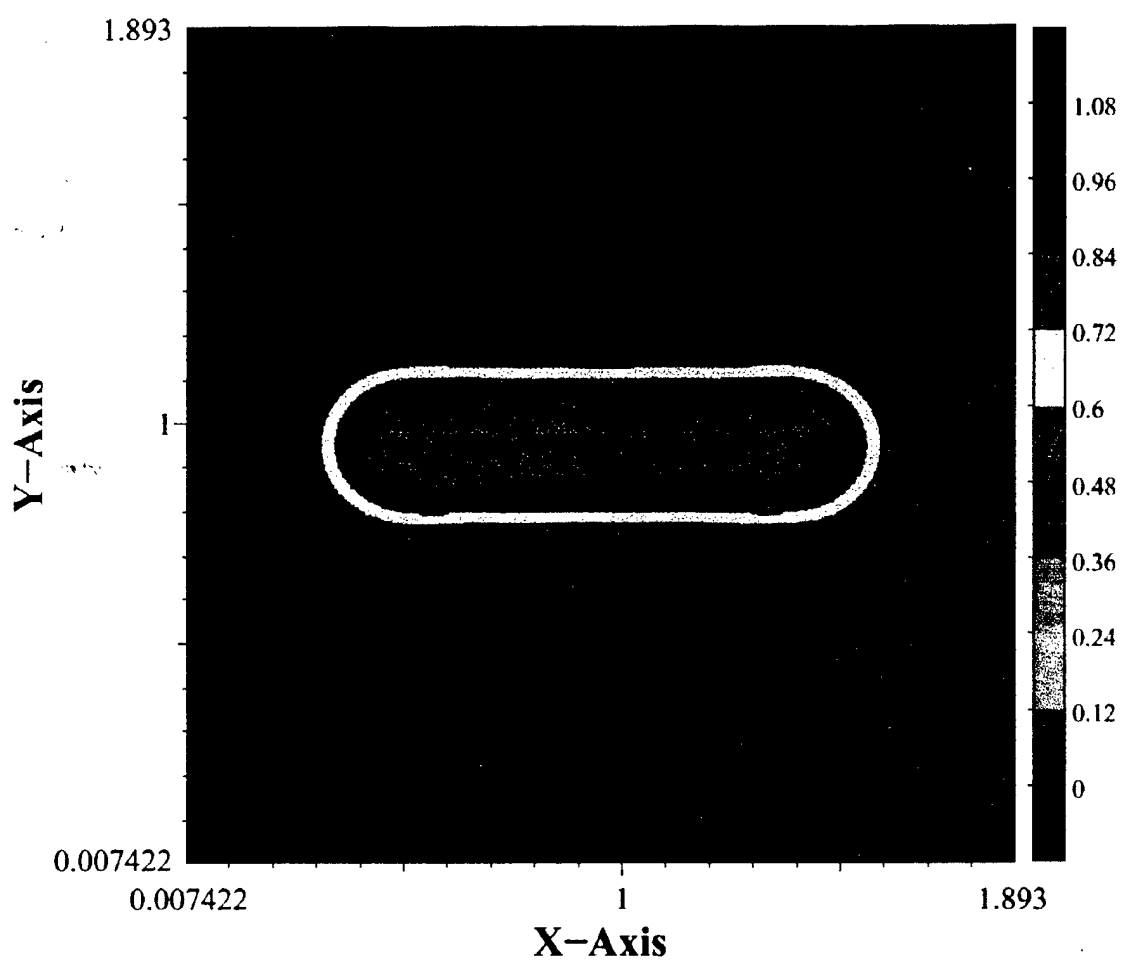
248 nm, Linear, Defocus = 300 nm



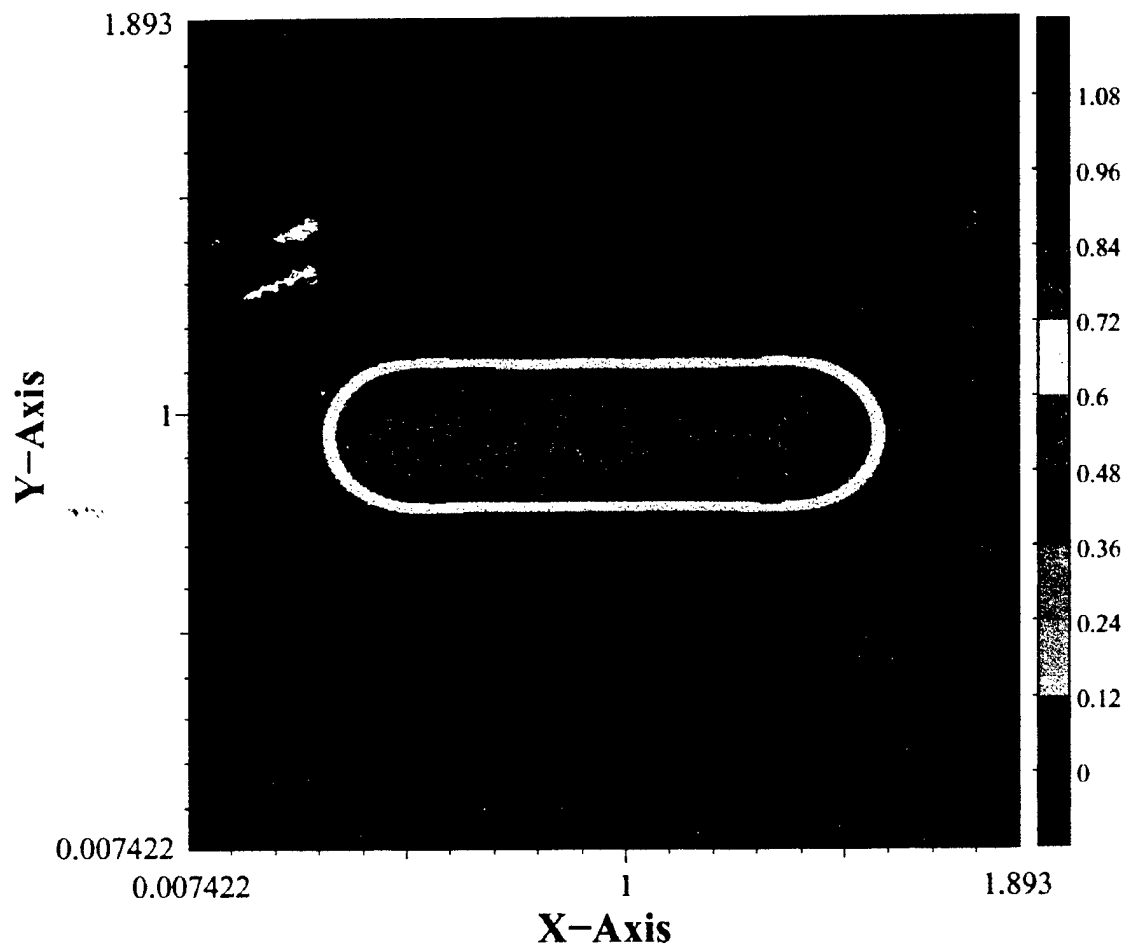
248 nm, Circular, Defocus = 300 nm



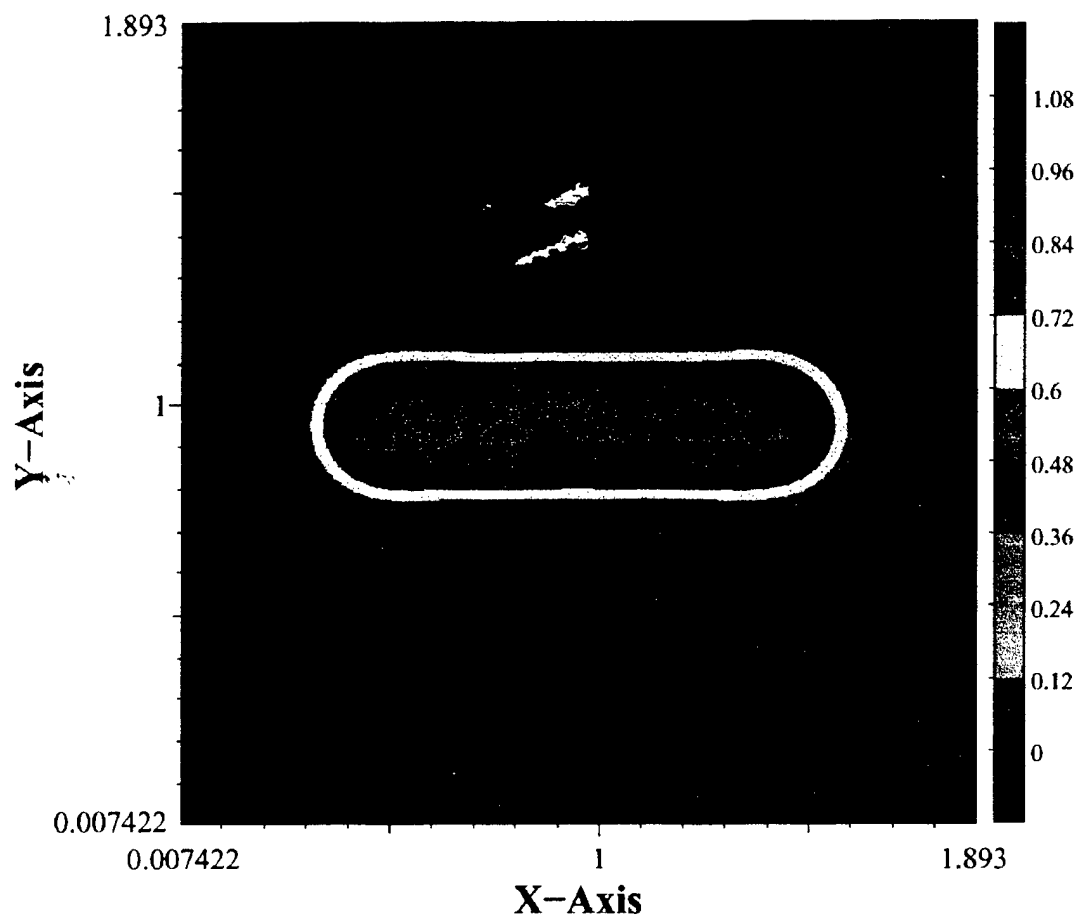
248 nm, Linear, Defocus = 200 nm



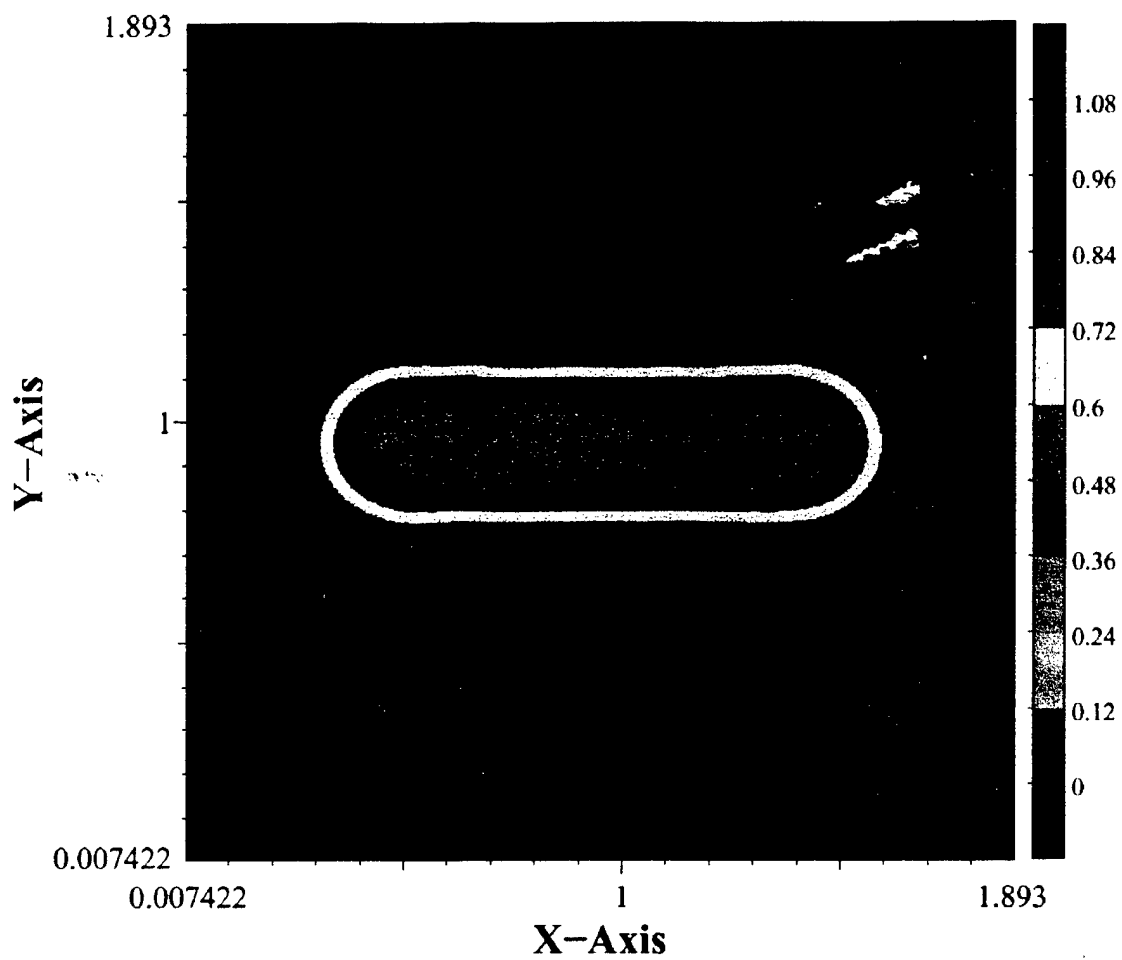
248 nm, Circular, Defocus = 200 nm



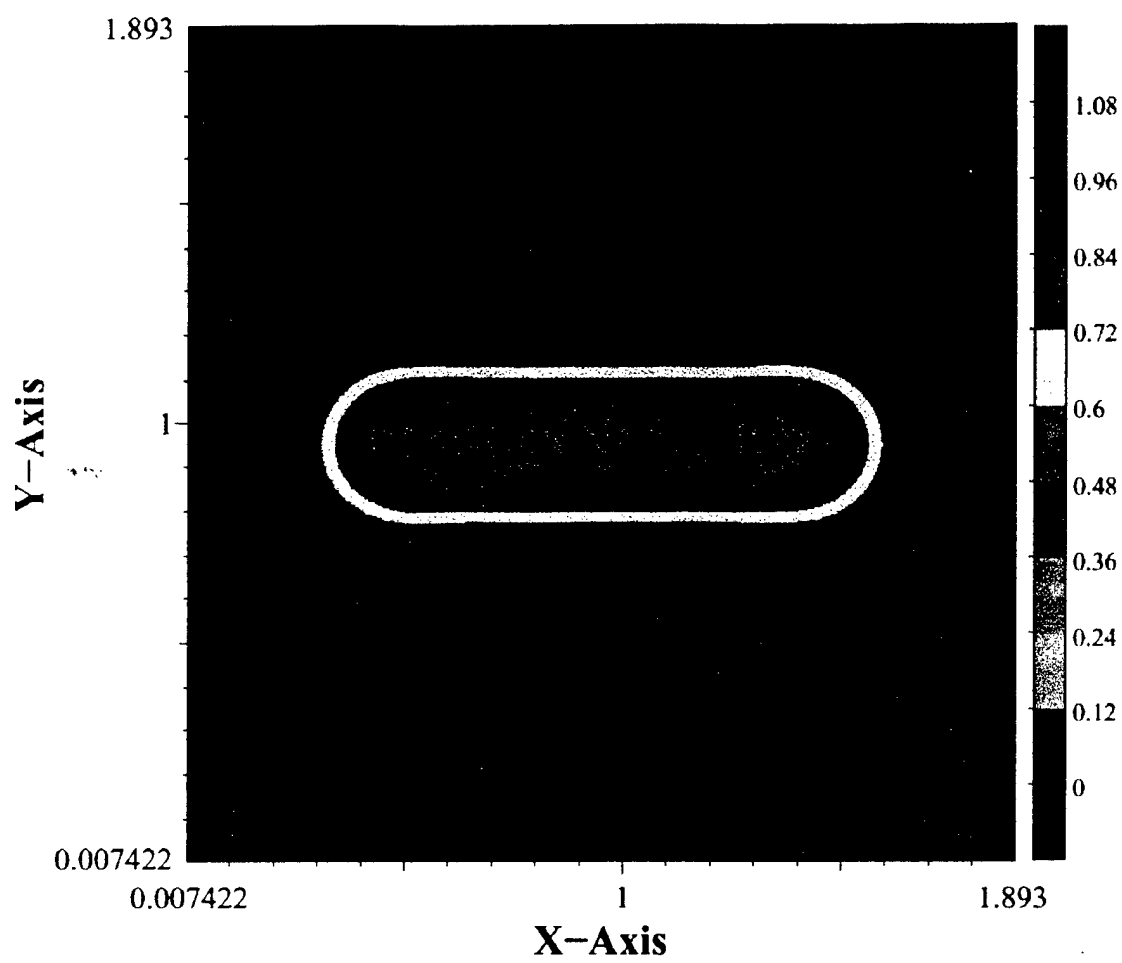
248 nm, Linear, Defocus = 100 nm



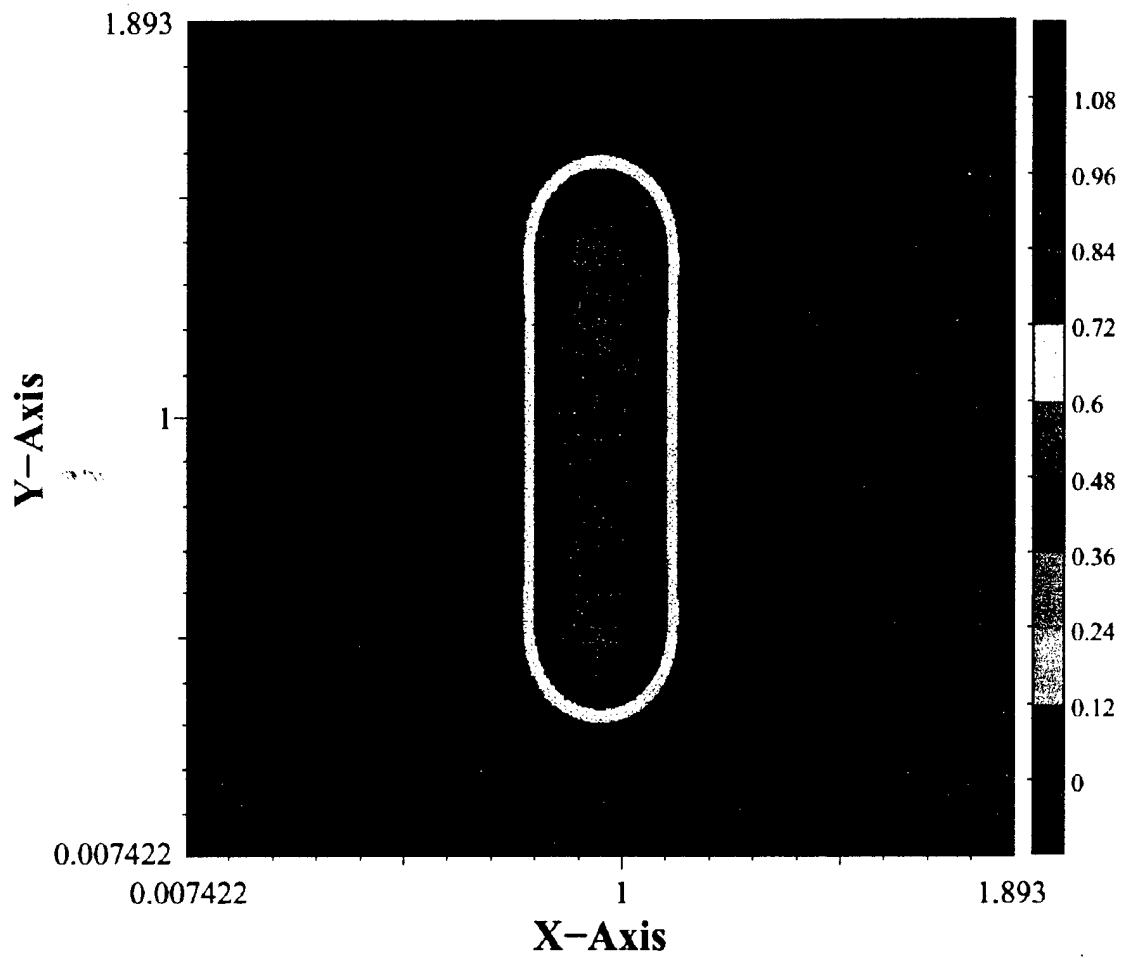
248 nm, Circular, Defocus = 100 nm



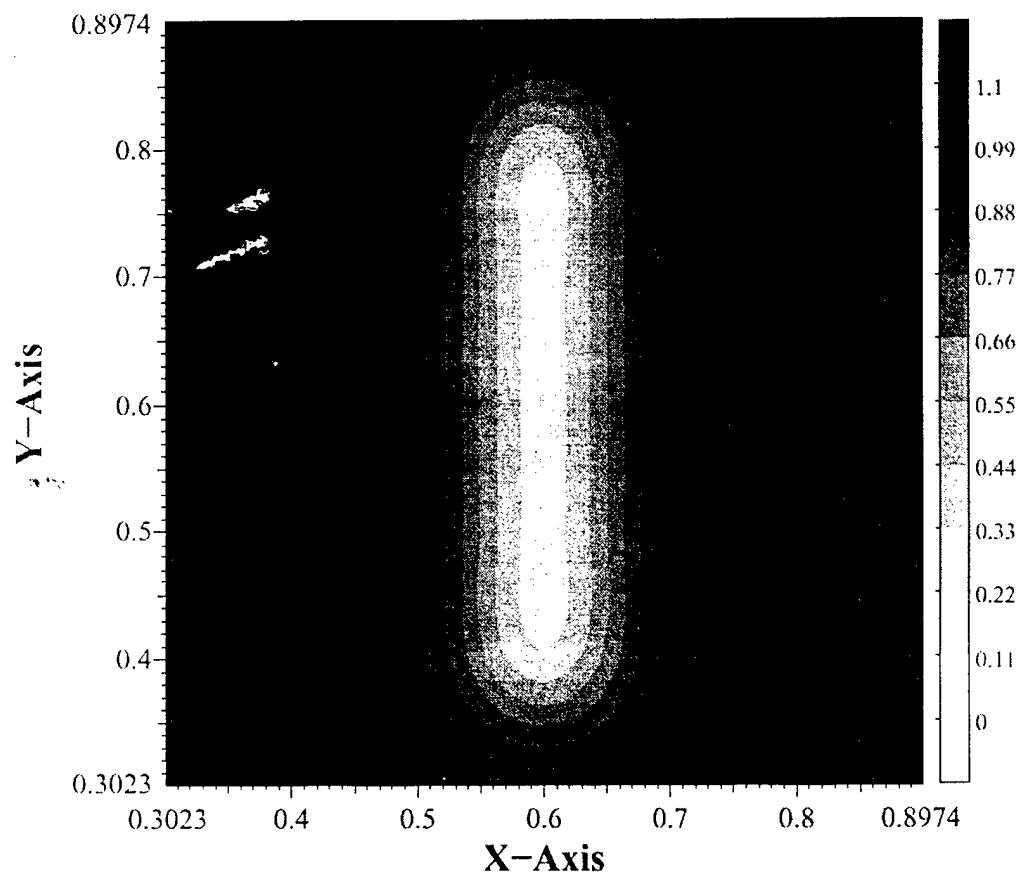
248 nm, Linear, Defocus = 0



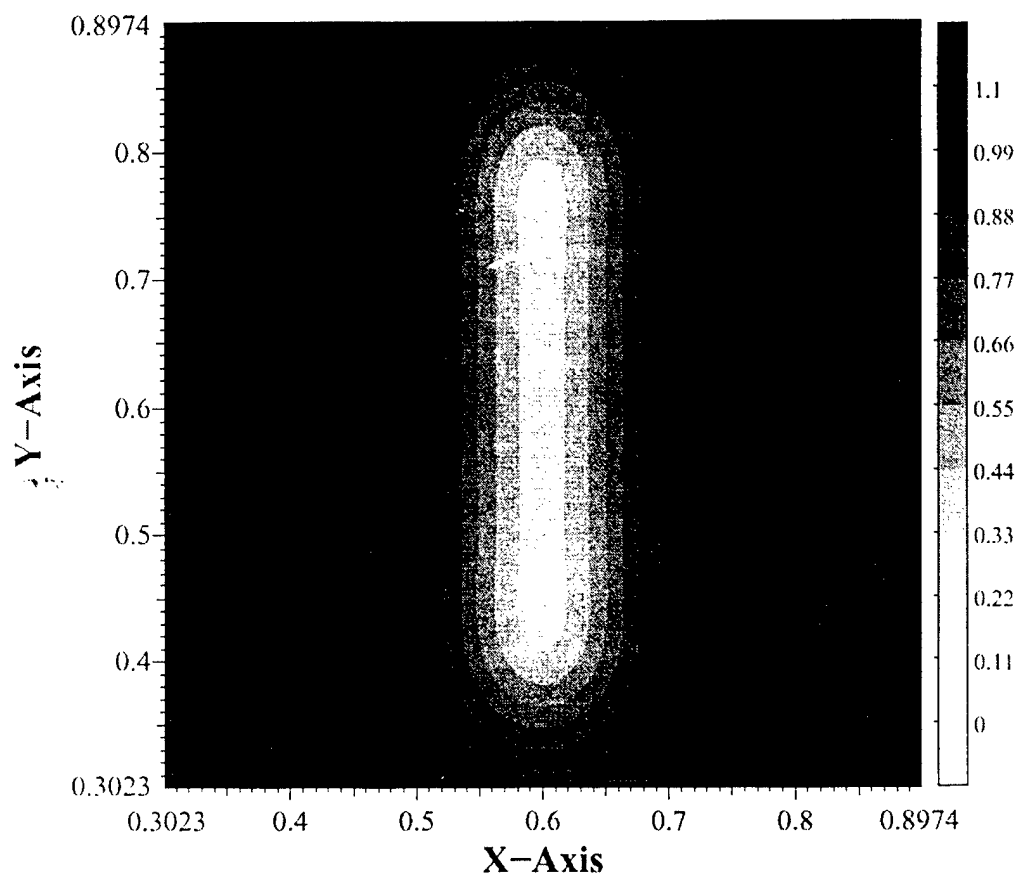
248 nm, Circular, Defocus = 0



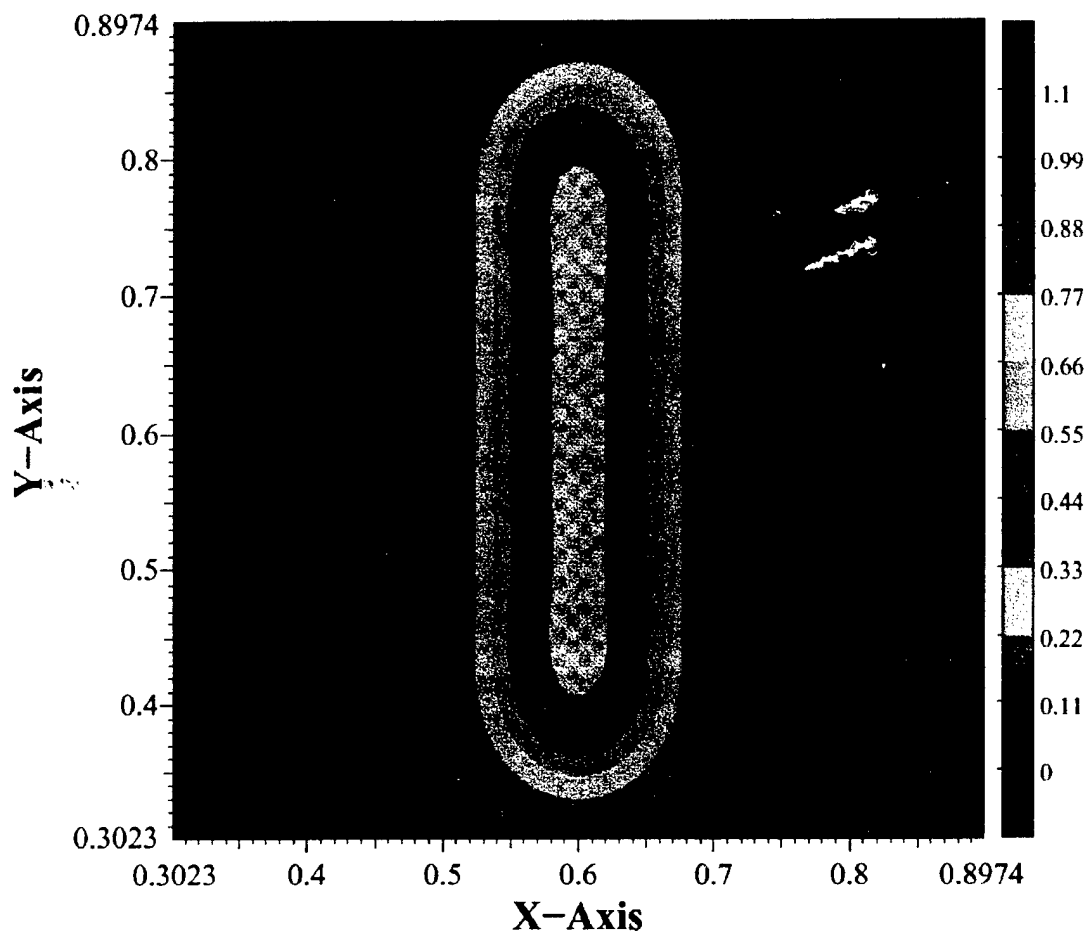
(Circular – 10 deg)–Mask–(QWP + 10 deg)–AN–QWP



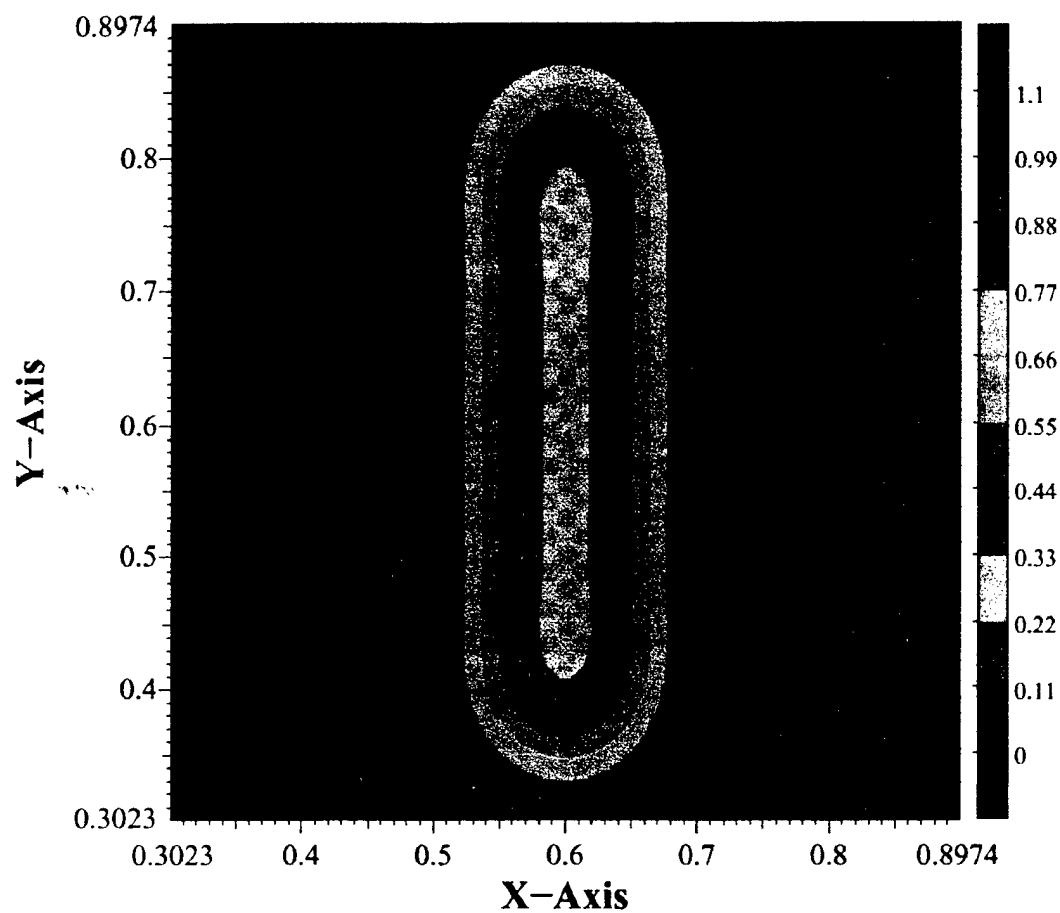
(Circular + 10 deg)–Mask–(QWP + 10 deg)–AN–QWP



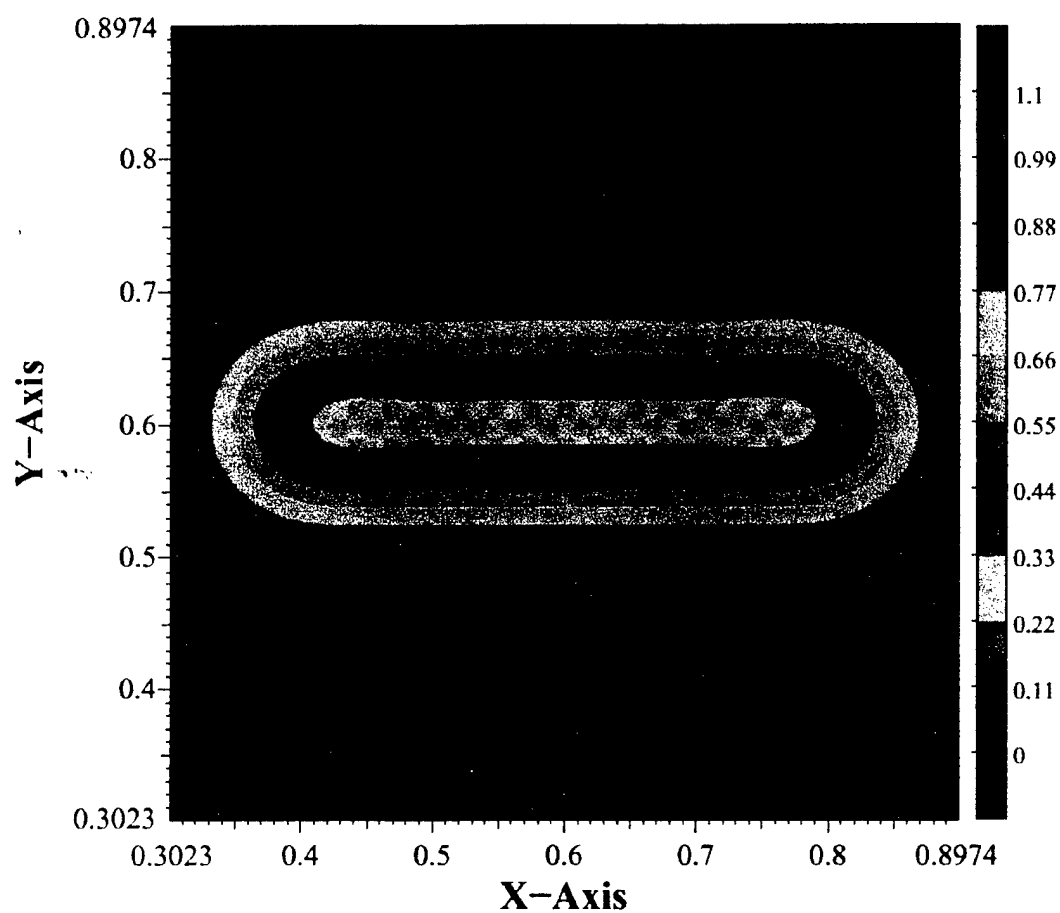
Y light)-(Mask in Y)-Analyzer-QWP



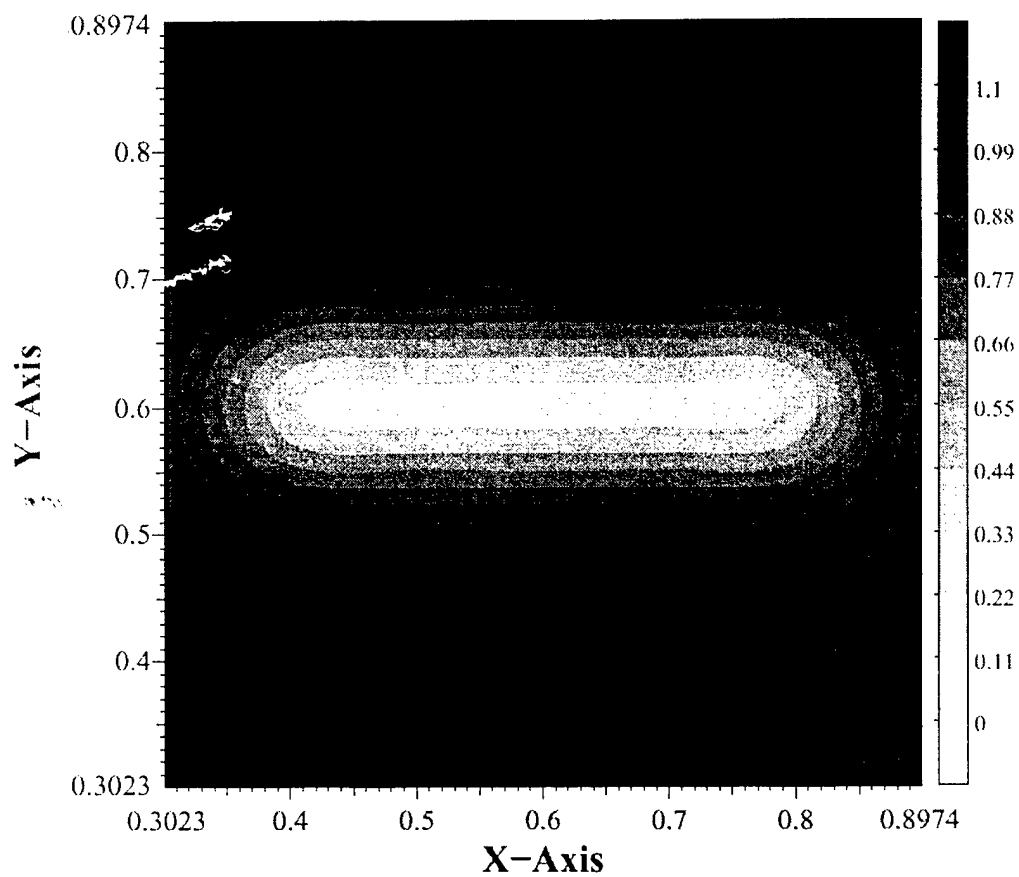
Circular light)-(Mask in Y)-QWP-Analyzer-QWP



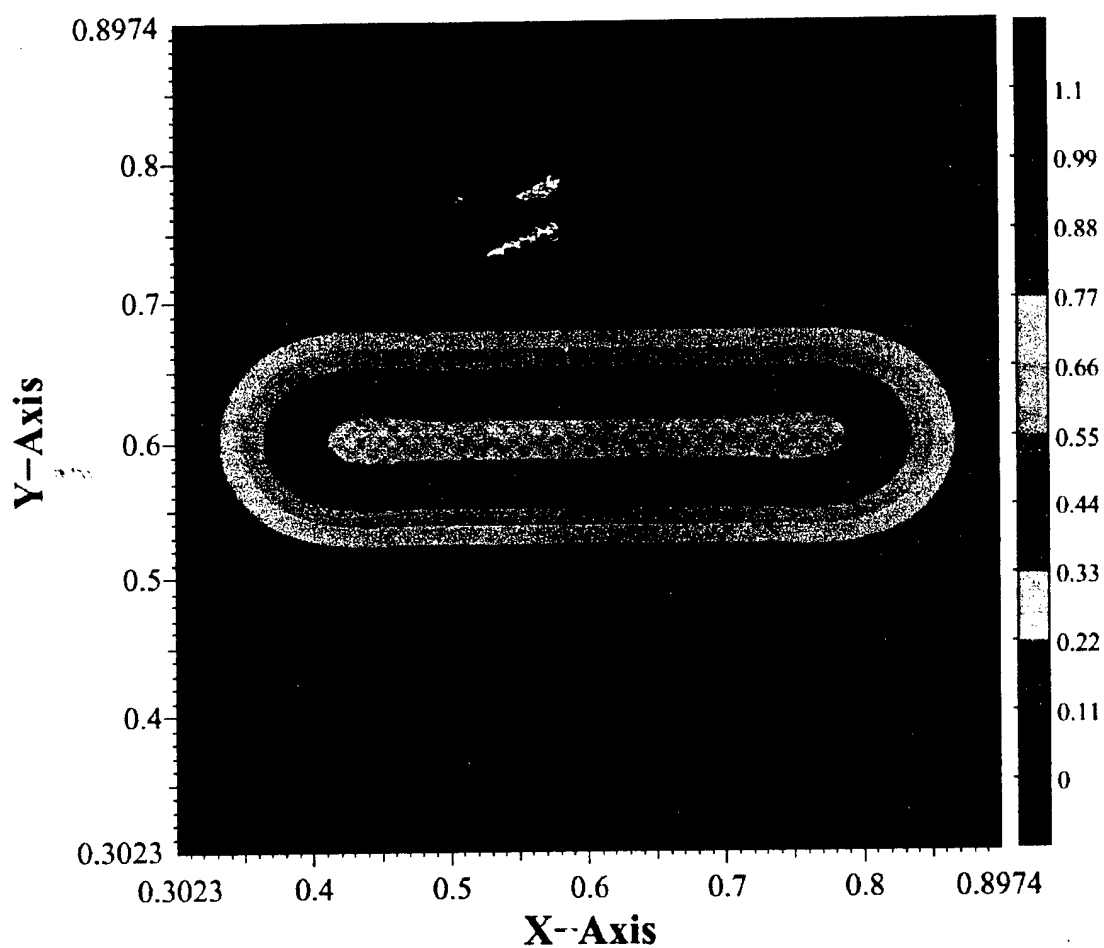
Circular light)–(Mask in X)–QWP–Analyzer–QWP



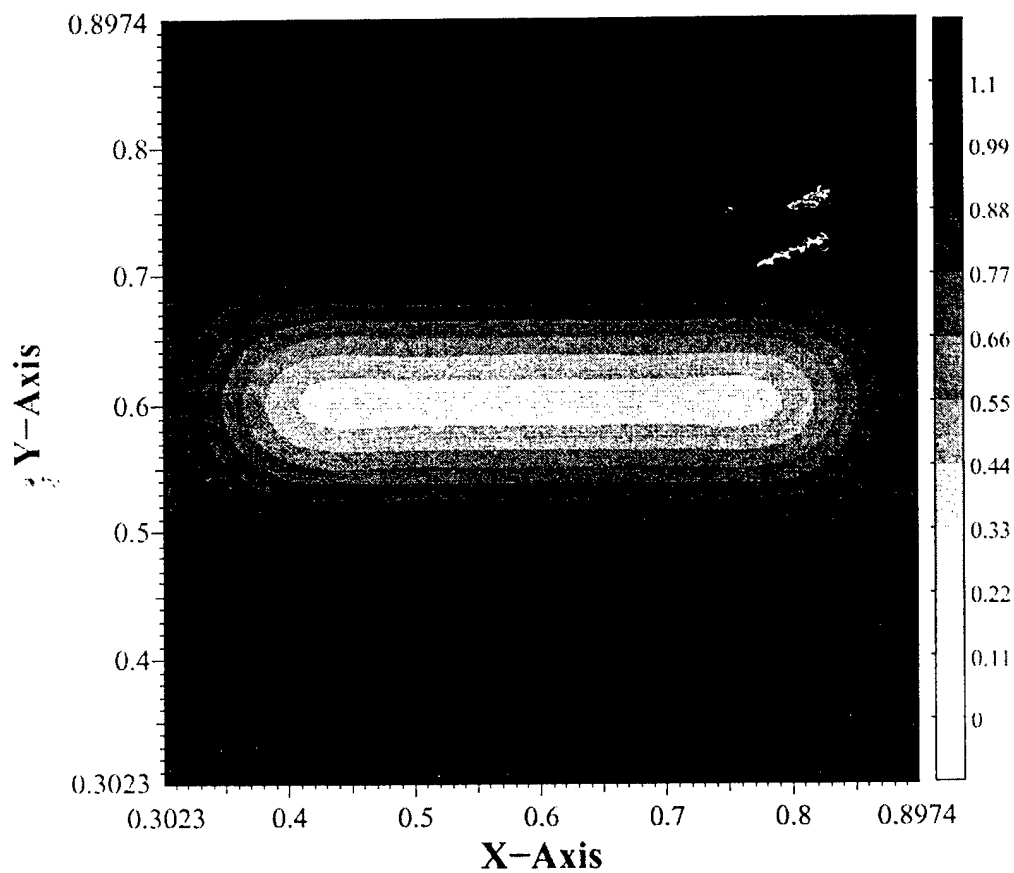
(Circular + 10 deg)–Mask–(QWP + 10 deg)–AN–QWP



Y light)-(Mask in X)-Analyzer-QWP

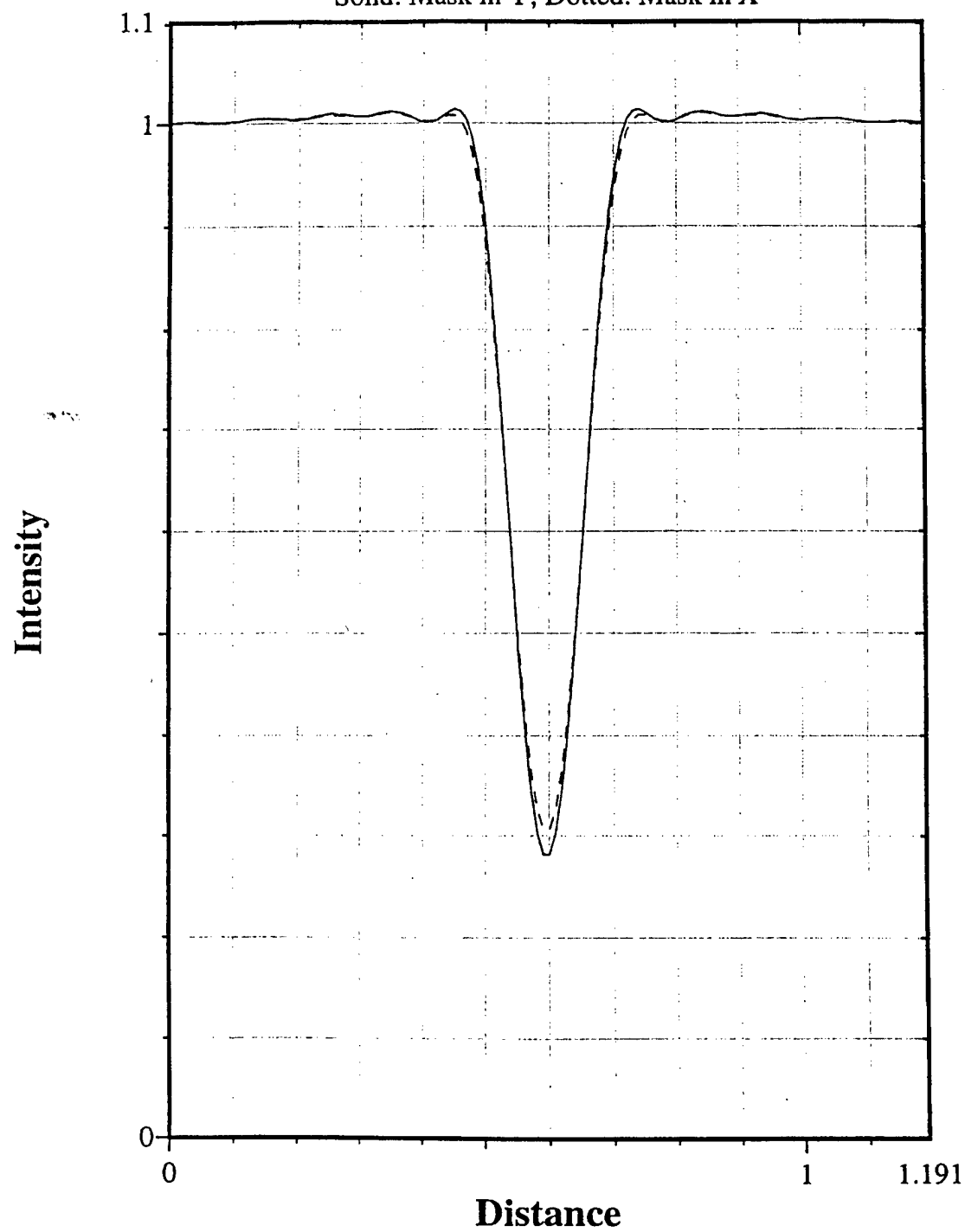


(Circular - 10 deg)-Mask-(QWP + 10 deg)-AN-QWP



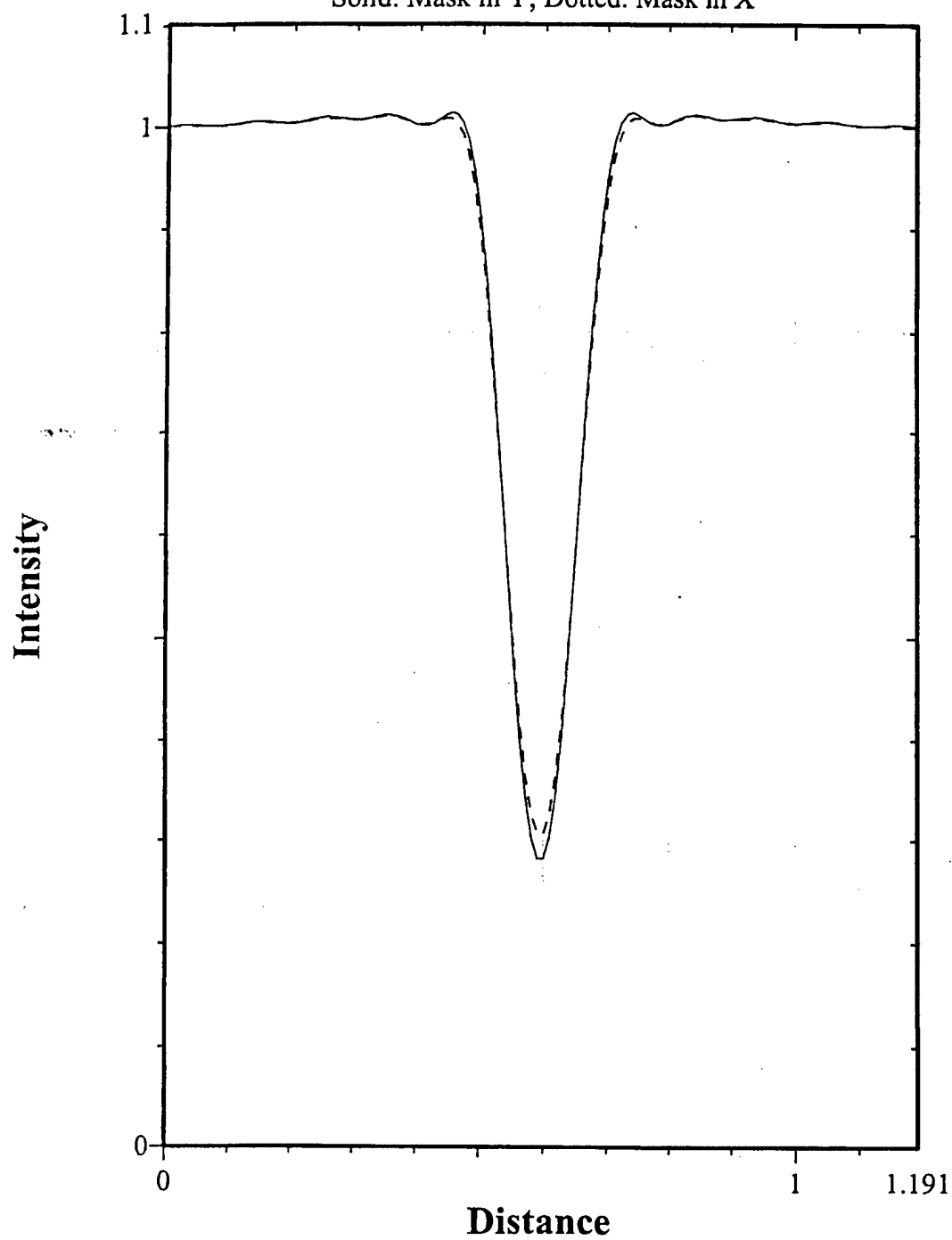
(Y light)–Mask–Analyzer–QWP

Solid: Mask in Y; Dotted: Mask in X



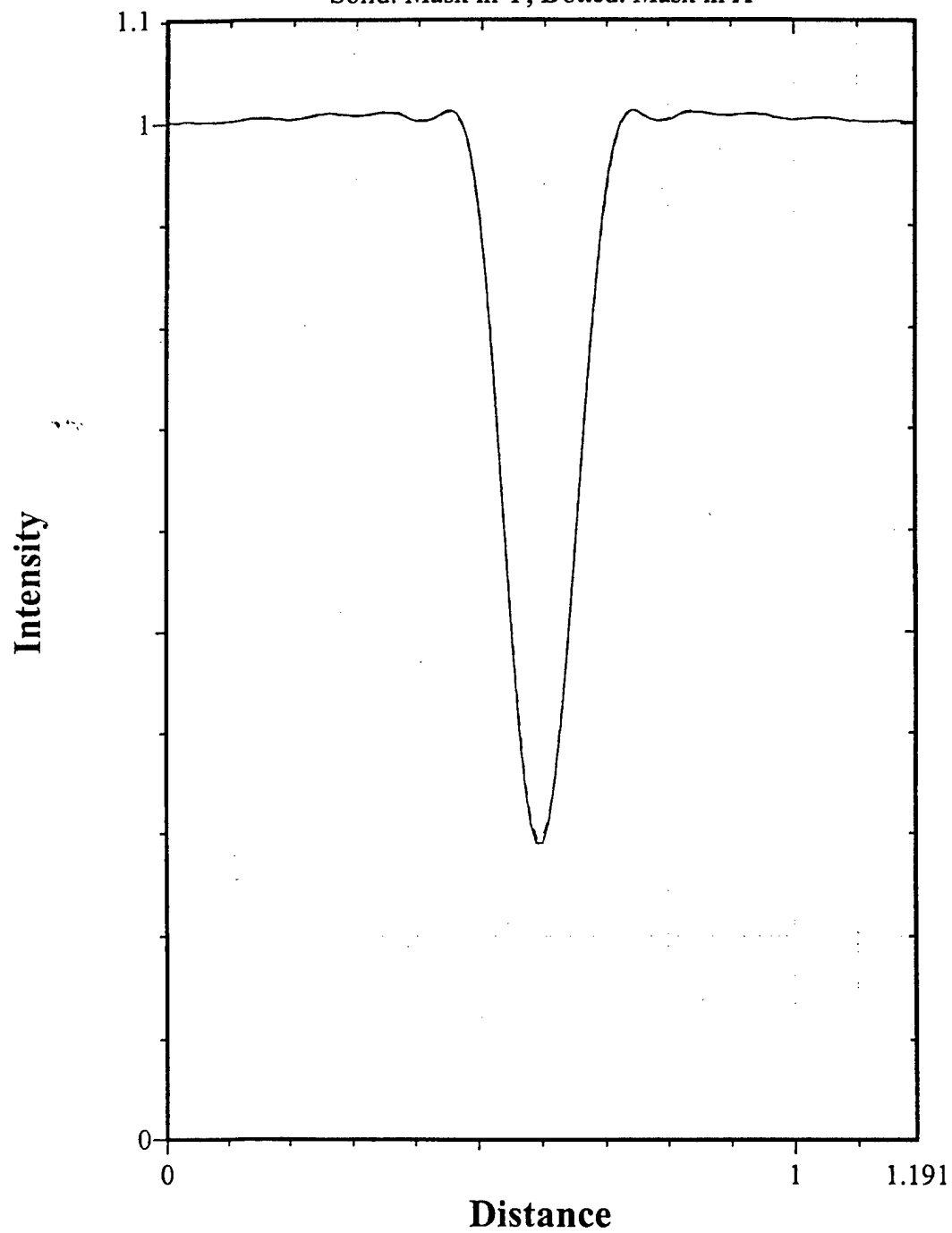
(Y light)–Mask–Analyzer–QWP

Solid: Mask in Y; Dotted: Mask in X



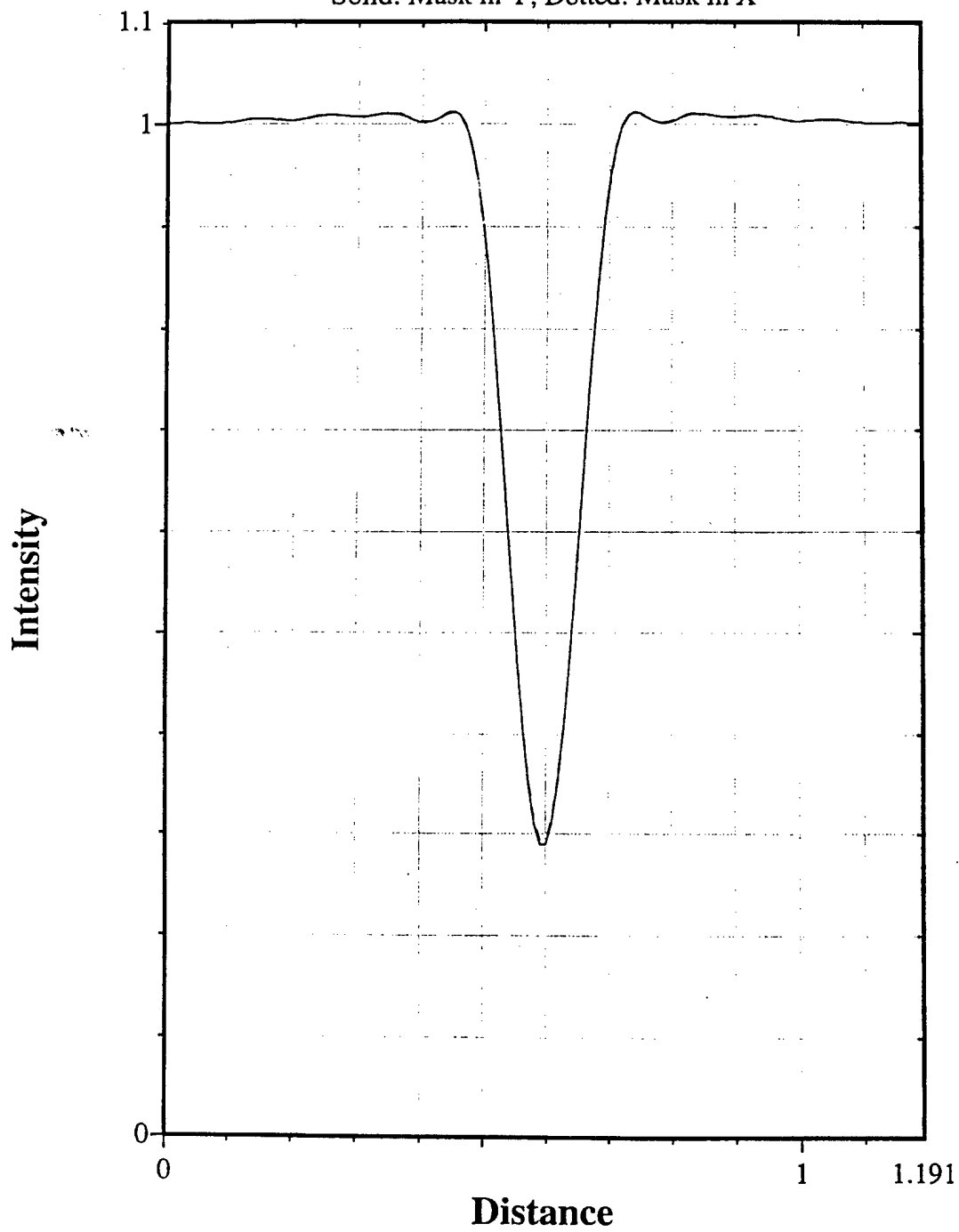
(Circular light)–Mask–QWP–Analyzer–QWP

Solid: Mask in Y; Dotted: Mask in X



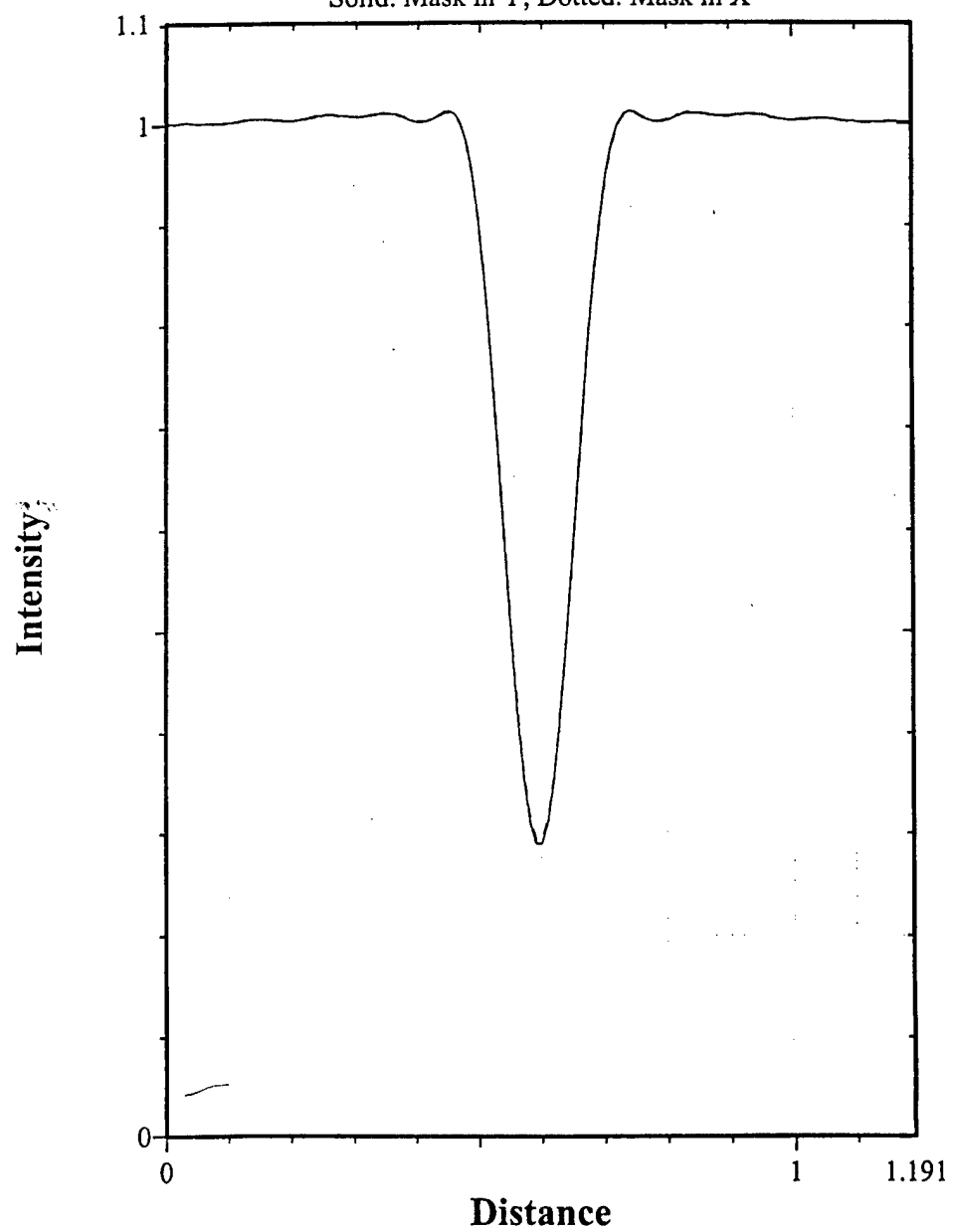
(Circular light)–Mask–QWP–Analyzer–QWP

Solid: Mask in Y; Dotted: Mask in X



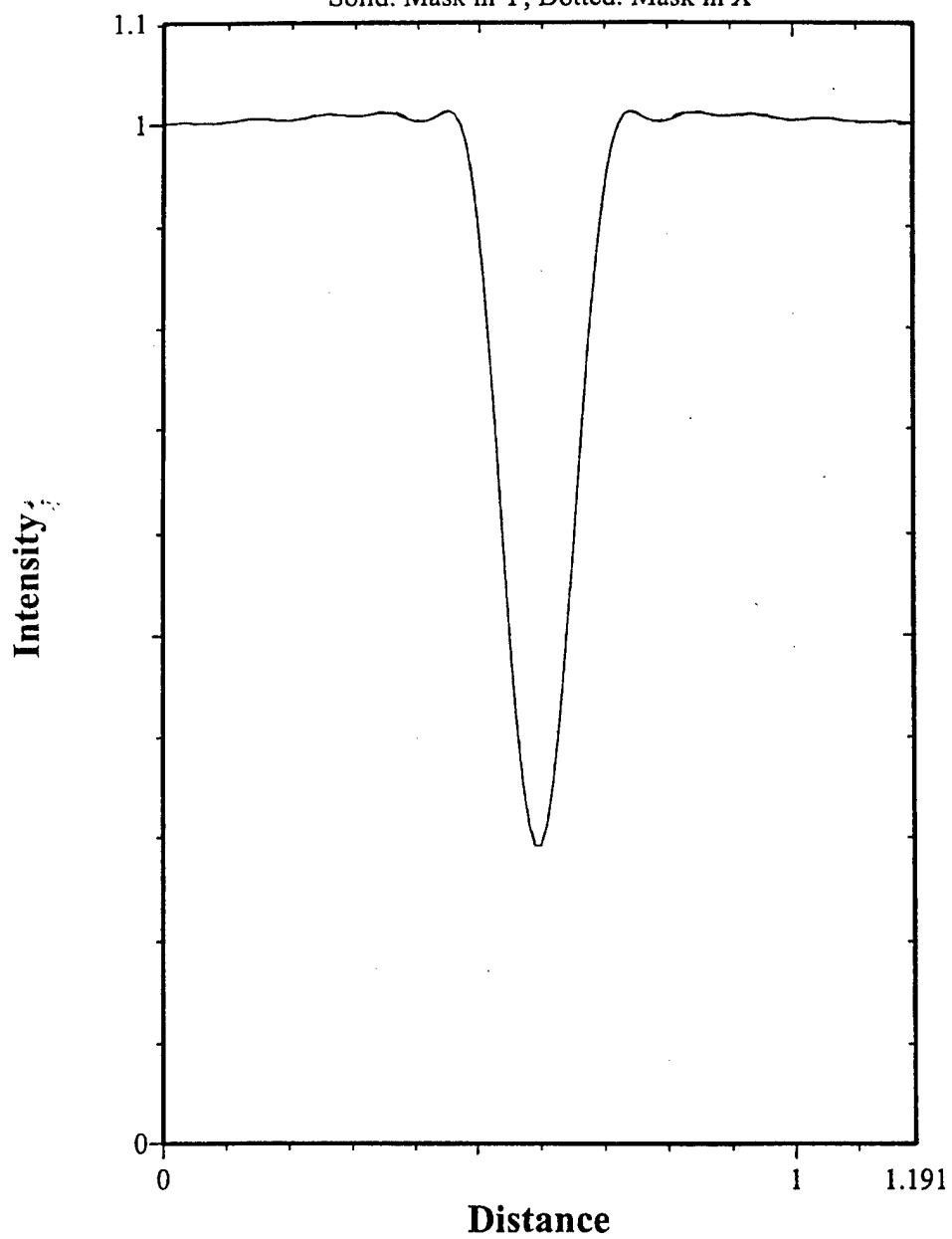
(Circular + 10 deg)-Mask-(QWP + 10 deg)-AN-QWP

Solid: Mask in Y; Dotted: Mask in X

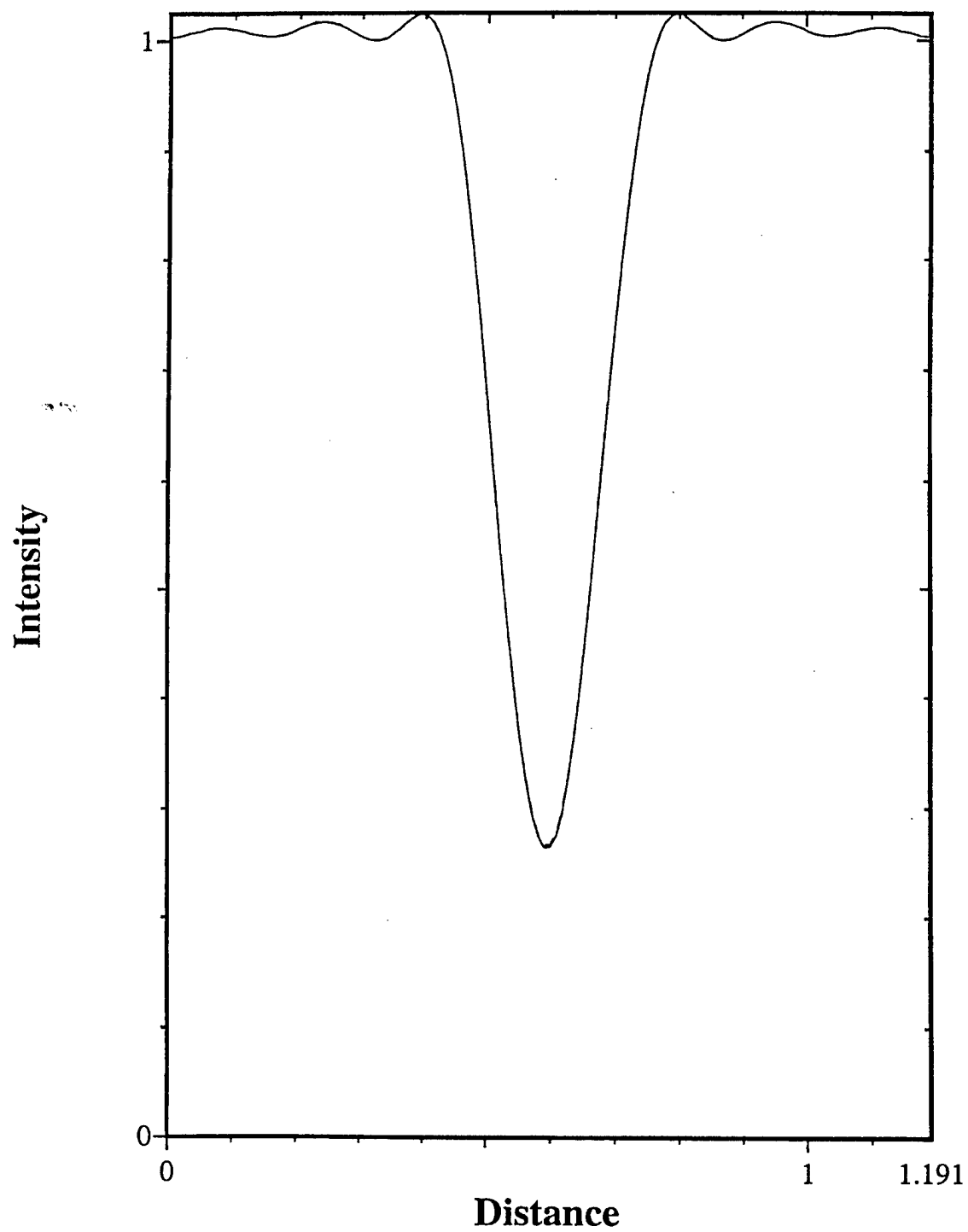


(Circular - 10 deg)-Mask-(QWP + 10 deg)-AN-QWP

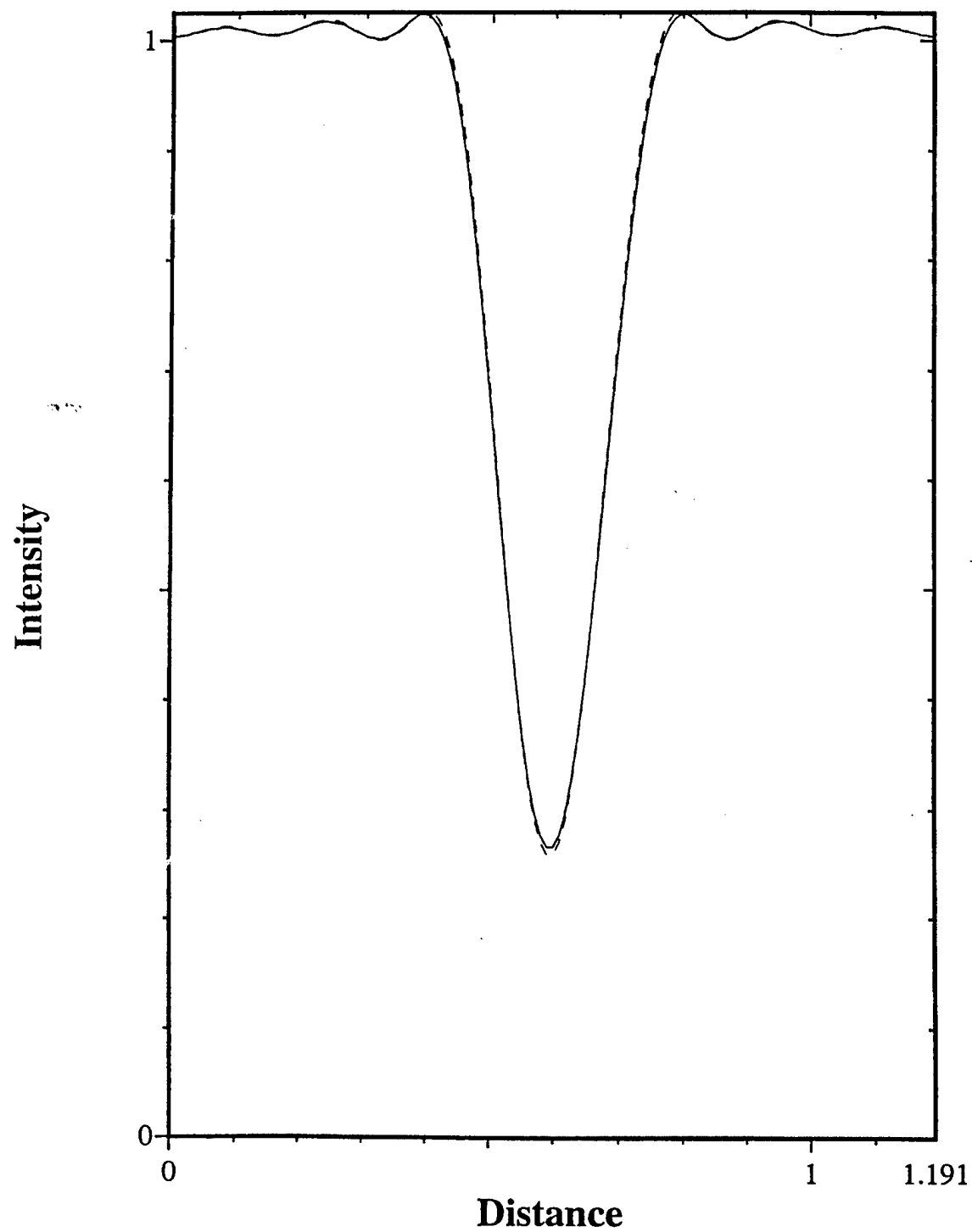
Solid: Mask in Y; Dotted: Mask in X



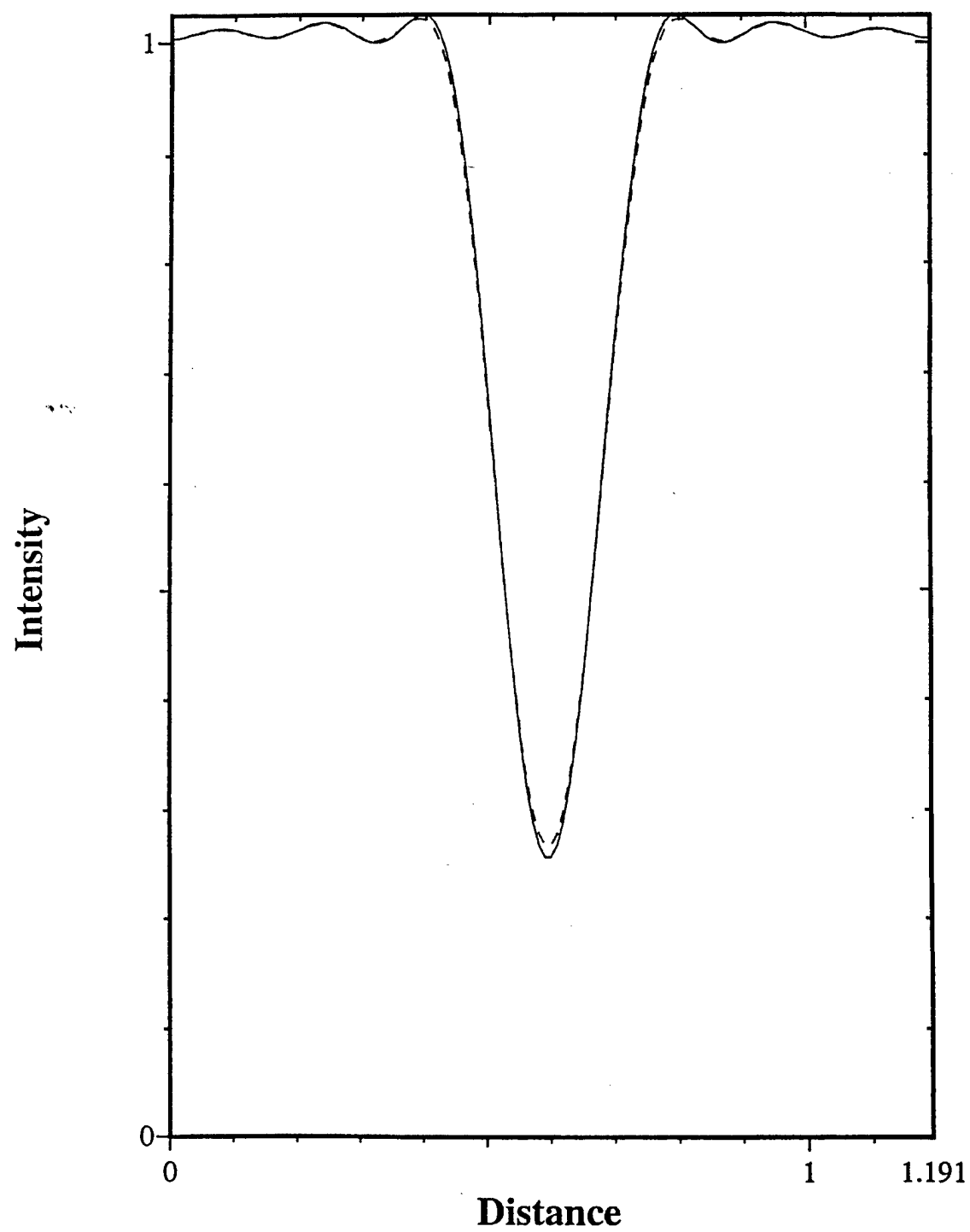
Circular, Chrome = 85 nm, Df = 0



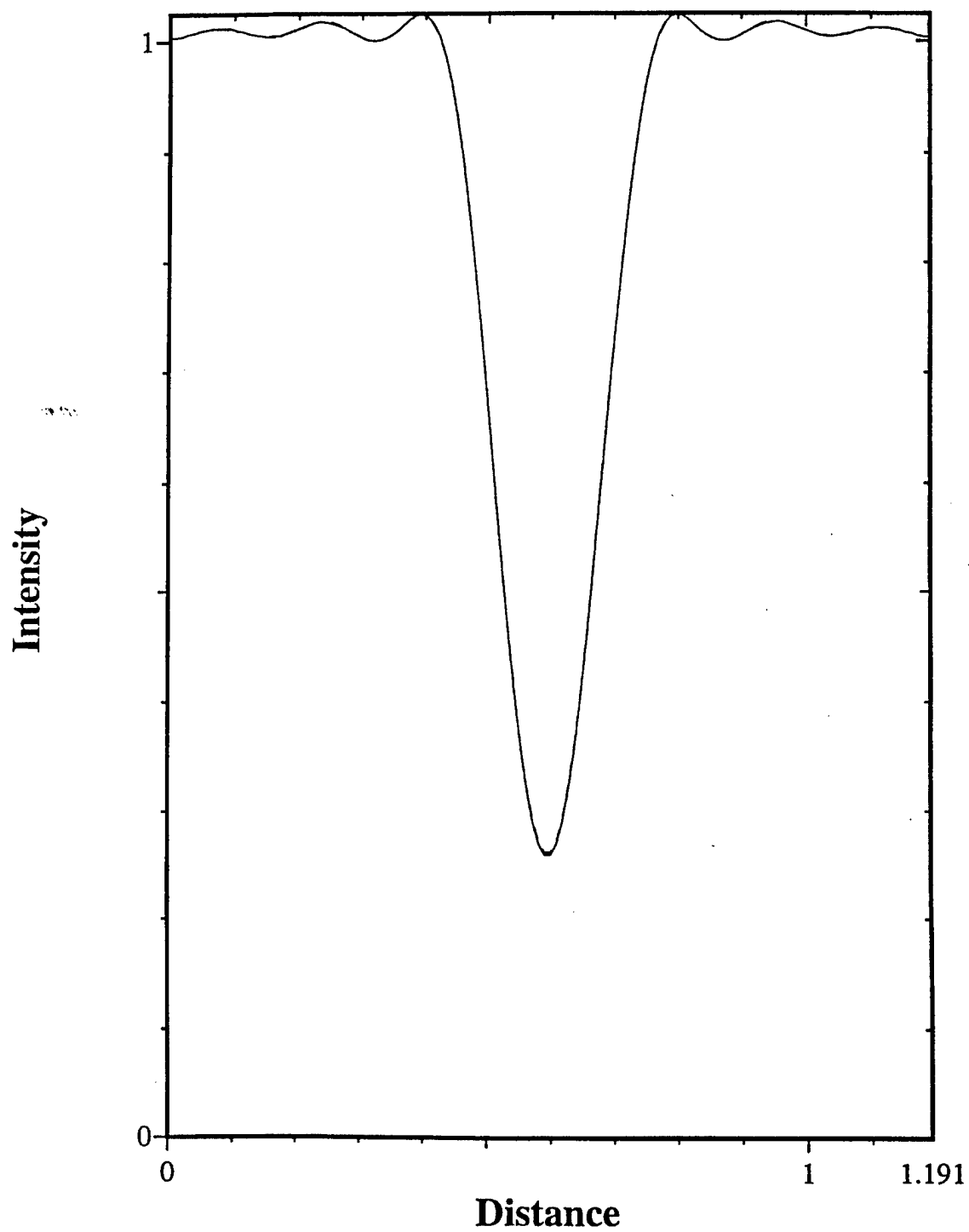
TE, Chrome = 97 nm, Df = 0



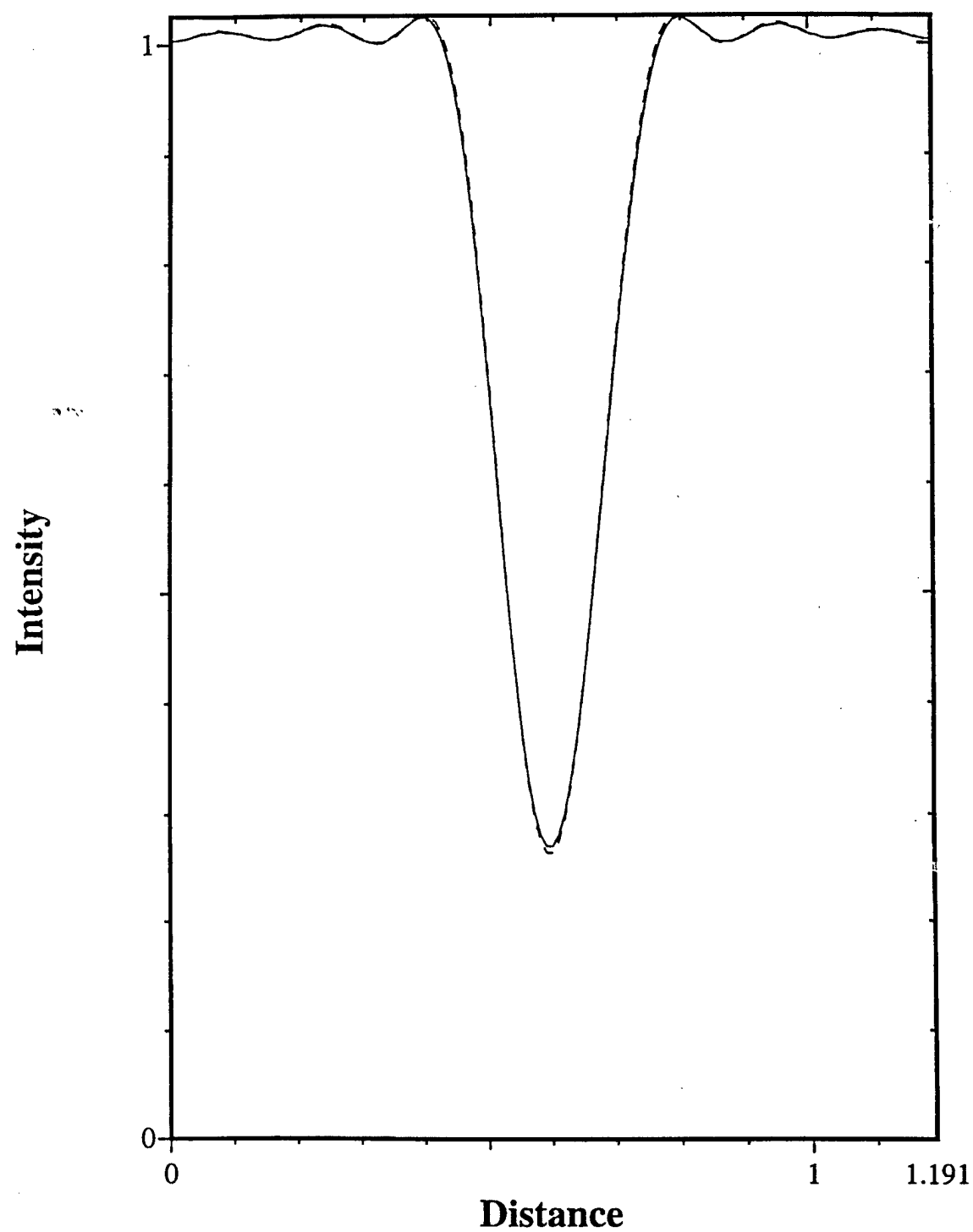
TM, Chrome = 97 nm, Df = 0



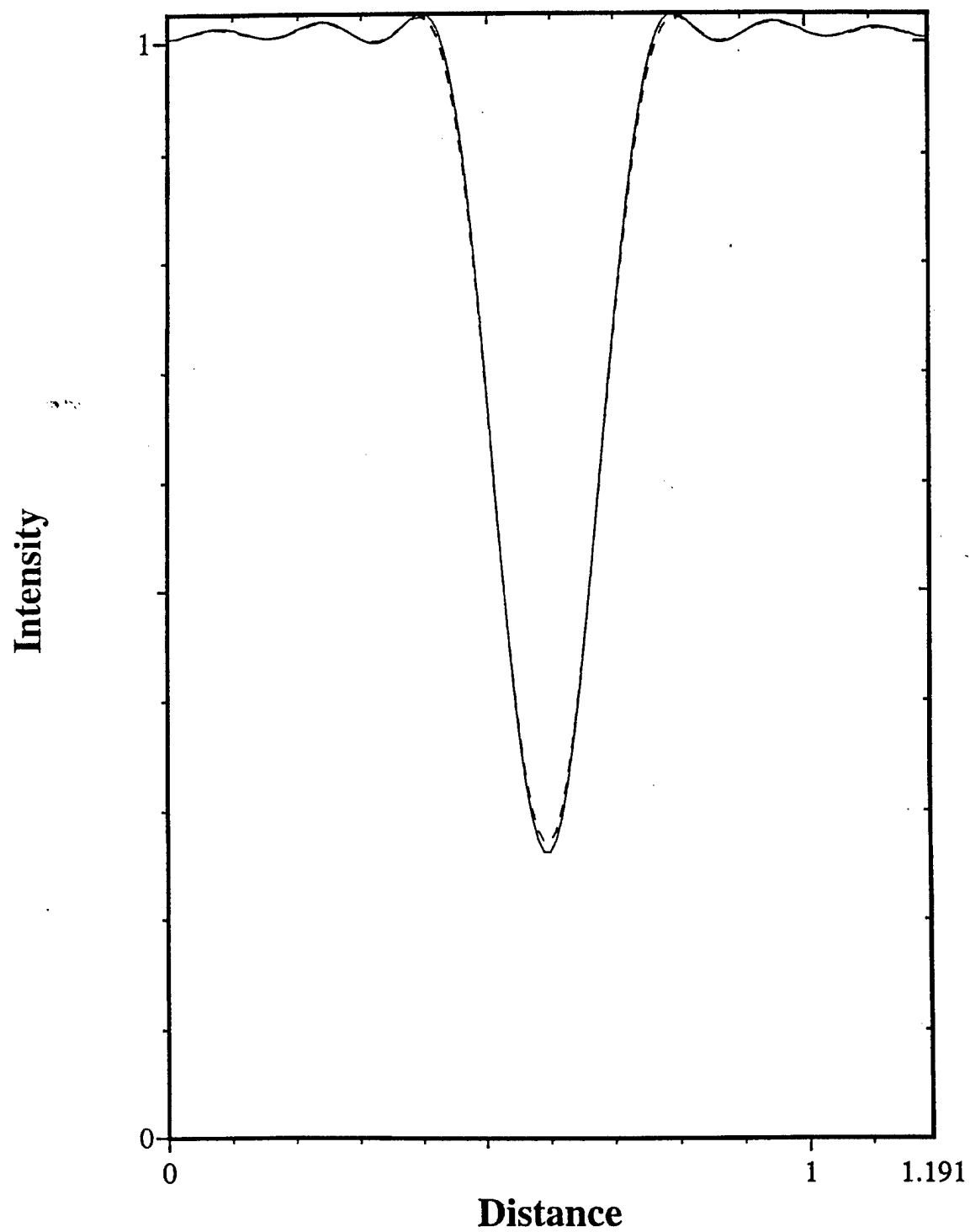
Circular, Chrome = 97 nm, Df = 0

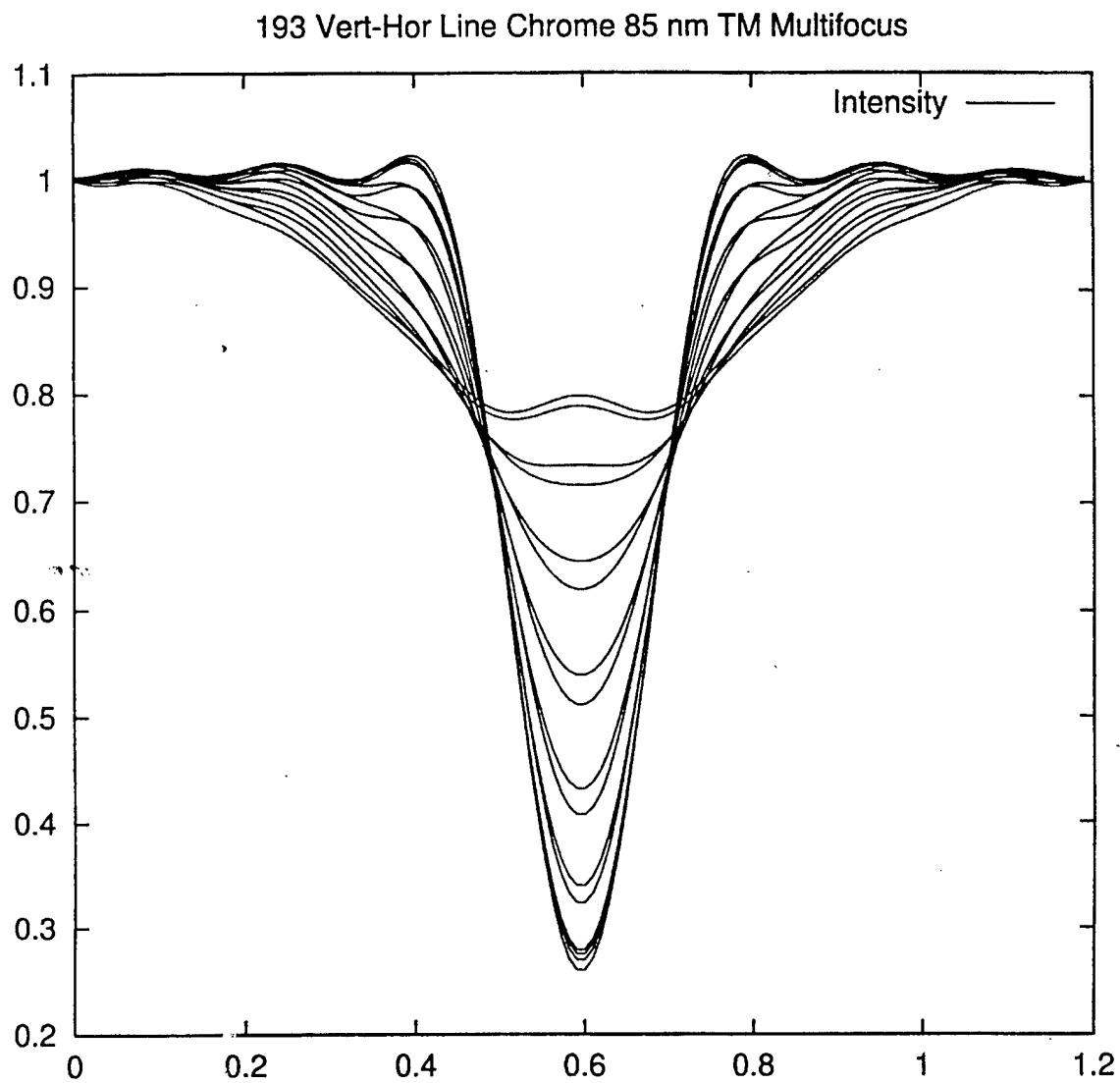


TE, Chrome = 85 nm, Df = 0

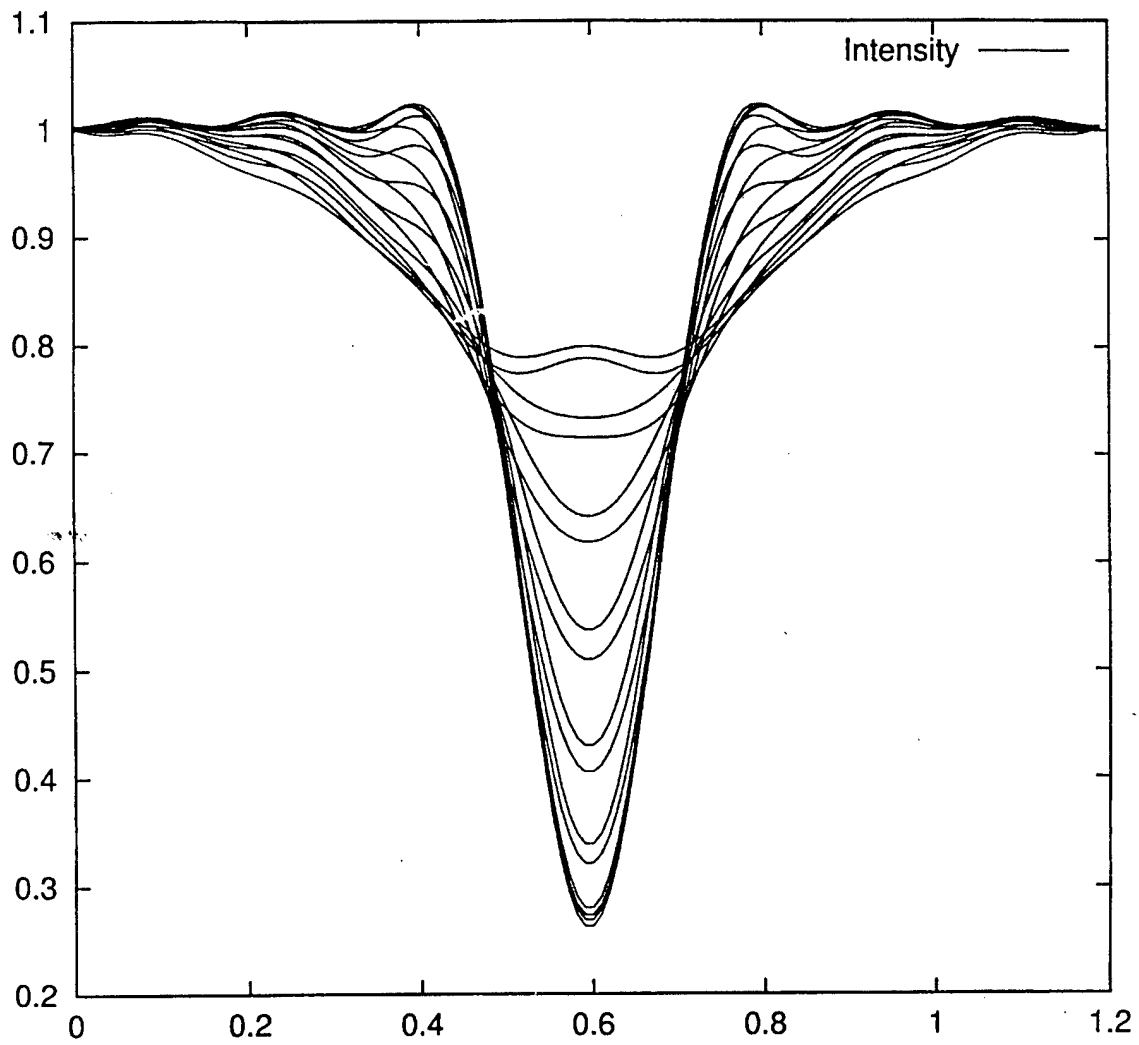


TM, Chrome = 85 nm, Df = 0

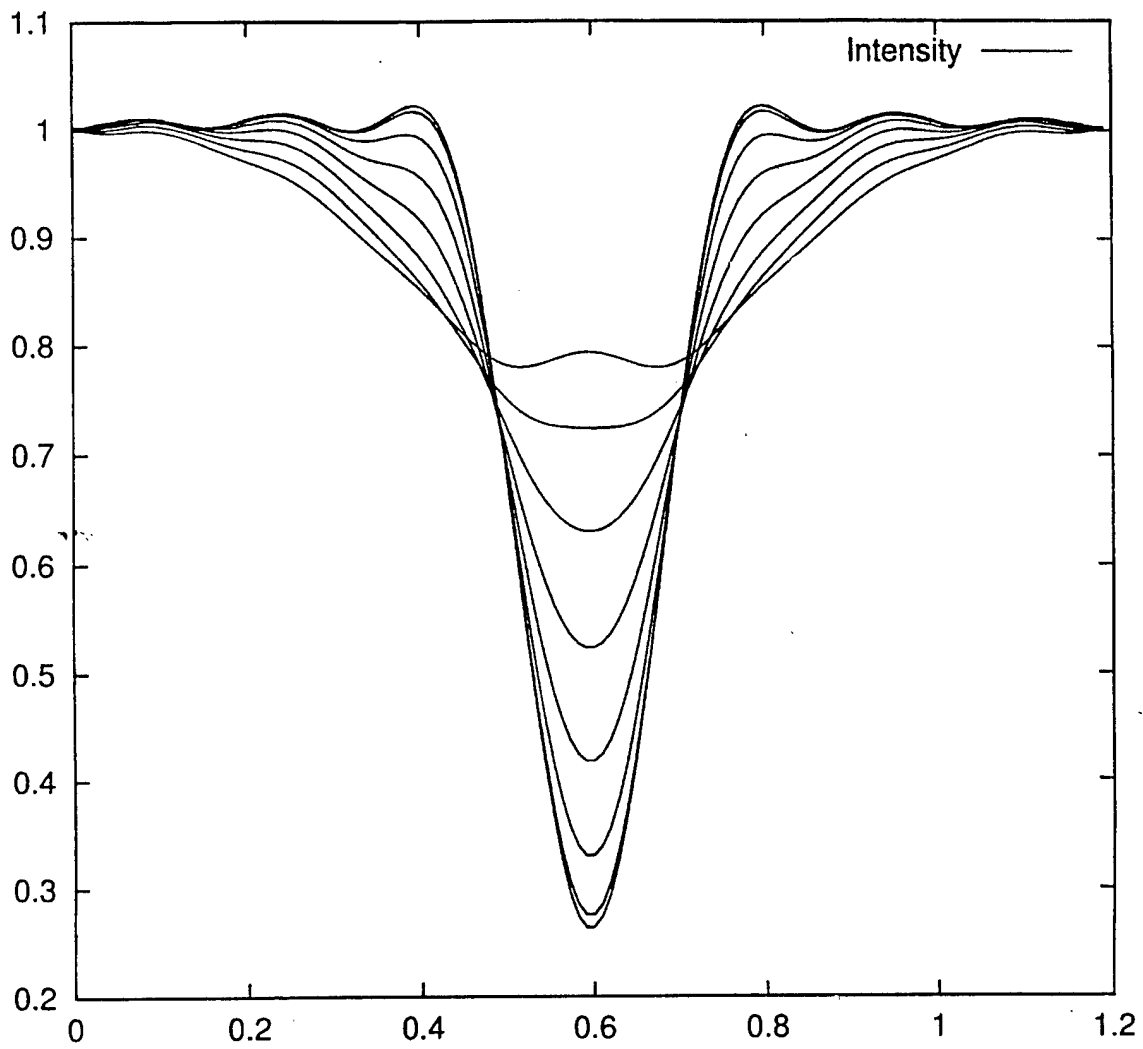




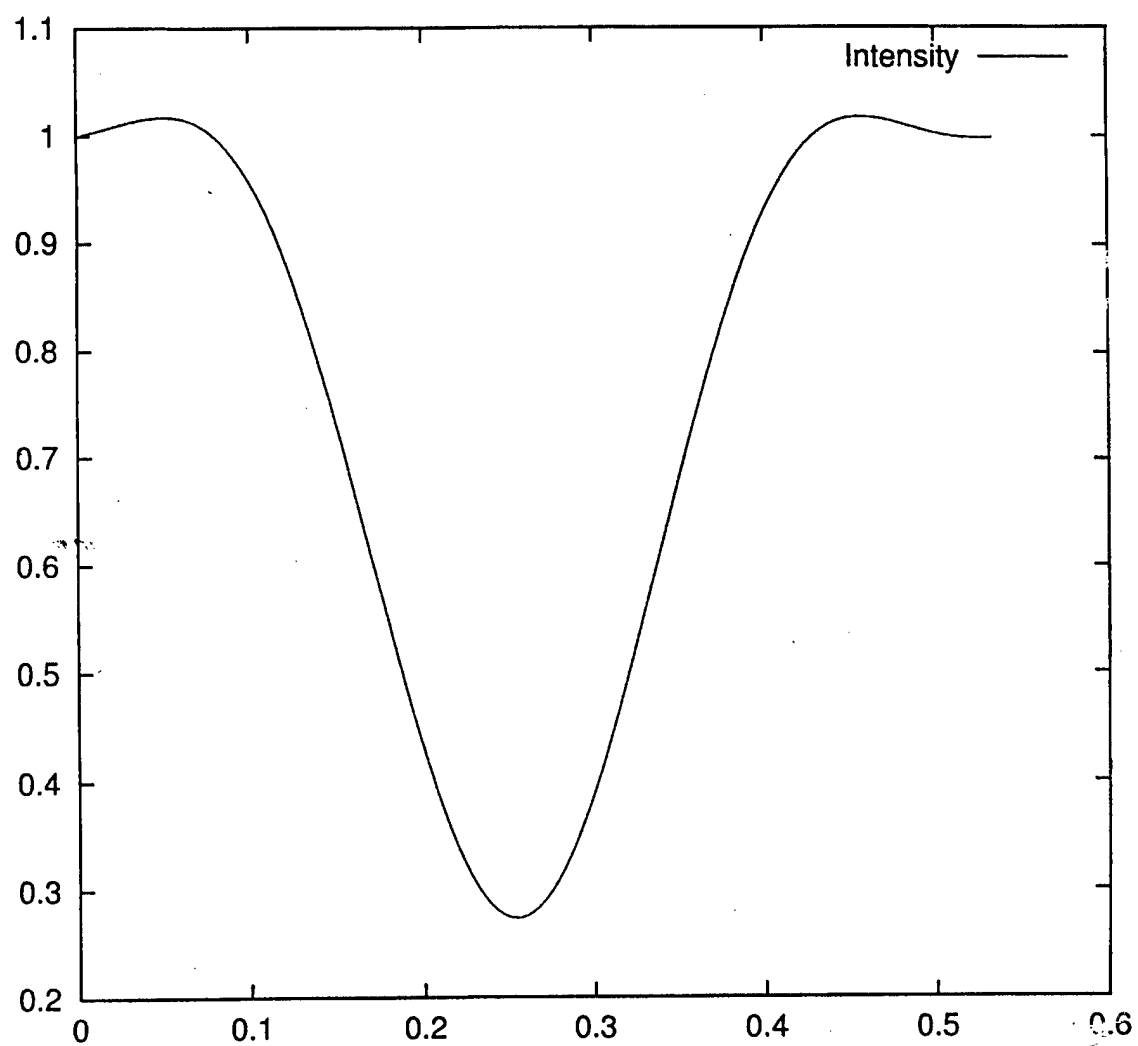
193 Vert-Hor Line Chrome 85 nm TE Multifocus



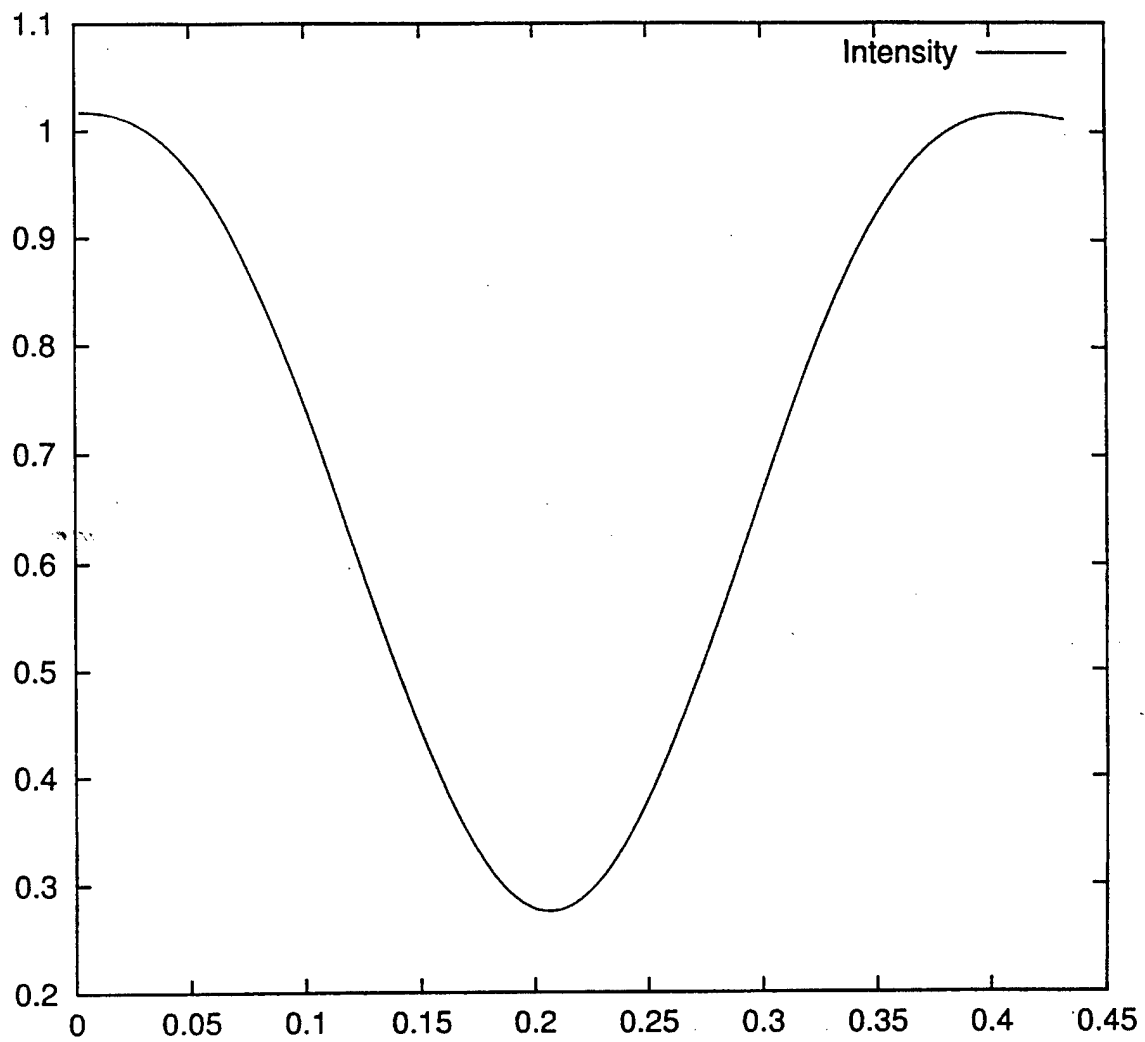
103 Vert-Hor Line Chrome 85 Cir Multifocus



193 Vert Line Cir Chrome 85 nm f=100 nm



193 Hor Line Cir Chrome 85 nm f=100 nm



2. BASIC FORMULATION

2.1. SCOPE OF WORK

The work involves the numerical simulation of the effects of polarization on aerial-image quality in 157-nm lithography. The finite-difference time-domain (FDTD) algorithm is being used to compute the electromagnetic field distribution in the near zone of a chromium photomask illuminated by a plane wave with arbitrary polarization and angle of incidence. The corresponding aerial image in the far zone is then being computed. The effects of partial coherence is being taken into account by incoherent superposition of the aerial images corresponding to different angles of incidence.

2.2. INNOVATIVE CLAIM

Three innovative features distinguish our approach from other approaches:

1. Oblique incidence is handled by the use of a Huygens surface excitation, in which the exact numerical dispersion relations and numerical reflection coefficients for the finite-difference mesh are employed to compute the steady-state field distribution within the multilayered photomask blank, for each Fourier component of the incident pulse.
2. A second-order accurate finite-difference updating equation for the electric field is used for the chromium region of the photomask structure, which is modeled by a plasma permittivity function.
3. A near-to-far field transformation based on multilayered media Green's functions is used to compute the aerial image in the far zone from the field distribution in the near zone, *without* assuming periodic boundary conditions.

The mathematical formulation of these innovative features is discussed below.

2.3. MATHEMATICAL FORMULATION

In this section, we discuss the mathematical formulation of the above innovative features of the software that is currently being developed for the simulation work.

2.3.1 HUYGENS SURFACE EXCITATION

In most existing FDTD software packages for lithography simulation, the excitation is applied to the uppermost surface of the computational domain only. Such an approach is strictly applicable only to normal incidence, since, in the case of oblique incidence, the excitation enters the computational domain from the sides also. In the general case, it is necessary to apply the excitation to all six sides of the computational domain, or, equivalently, to a Huygens surface completely enclosing the mask feature.

The technique of Huygens surface excitation was developed by Holland and Williams [1] for objects embedded in *empty* space. For lithography simulation, however, it is necessary to take into account the presence of the substrate, which in our case is the multilayered photomask blank extending essentially to infinity horizontally. Here, it is necessary to generalize Holland's method to take into account the multiple reflections of the incident plane wave inside the multilayered substrate.

Although the propagation of a plane wave in a multilayered medium is a well-known problem in classical optics, one cannot apply the well-known results of thin-film optics directly to FDTD computation. The reason is that, in the finite-difference method, one deals with a *discrete* lattice space, rather than a *continuous* space on which the thin-film optics solution is based. Indeed, a plane wave traveling in a lattice space obeys a different dispersion relation, that is, has a different phase velocity, than one traveling in continuous space. Furthermore, the Fresnel coefficients for a lattice space are different from those for a continuous space. In order to generalize Holland's method to lithography simulation, one must first determine the correct dispersion relations and Fresnel coefficients for a multilayered lattice space. Furthermore, one must consider a *plasma* lattice space, since the materials used in 157-nm lithography can have *negative* real permittivity, that is, a refractive index $n = n_r + j\kappa$ for which $\kappa > n_r$, which requires the use of a plasma permittivity function.

2.3.1.1 DISPERSION RELATION FOR A PLASMA LATTICE SPACE

The dispersion relation for a plane wave traveling in an ordinary (non-plasma) lattice space is well known. It is included here for reference:

$$\frac{\sin^2\left(\frac{k_x\Delta x}{2}\right)}{(\Delta x)^2} + \frac{\sin^2\left(\frac{k_y\Delta y}{2}\right)}{(\Delta y)^2} + \frac{\sin^2\left(\frac{k_{z1}\Delta z_1}{2}\right)}{(\Delta z_1)^2} = \frac{\mu\epsilon_1 \sin^2\left(\frac{\omega\Delta t}{2}\right)}{(\Delta t)^2}, \quad (1)$$

where $\epsilon_1 > 0$ is the permittivity of the ordinary dielectric medium.

The dispersion relation for a plasma lattice space, however, is not so well known. We have derived the following new result for a plasma lattice space with plasma parameters ω_p and ν_c :

$$\begin{aligned} \frac{\sin^2\left(\frac{k_x\Delta x}{2}\right)}{(\Delta x)^2} + \frac{\sin^2\left(\frac{k_y\Delta y}{2}\right)}{(\Delta y)^2} + \frac{\sin^2\left(\frac{k_{z2}\Delta z_2}{2}\right)}{(\Delta z_2)^2} &= \frac{\mu\epsilon_0 \sin^2\left(\frac{\omega\Delta t}{2}\right)}{(\Delta t)^2} - j\frac{\mu\epsilon_0\omega_p^2}{4} \sin(\omega\Delta t) \\ &\times \left[\alpha_0 + \frac{\alpha_1}{e^{(j\omega+\nu_c)\Delta t} - 1} \right], \quad (2) \end{aligned}$$

where

$$\alpha_0 = \frac{1}{\nu_c\Delta t} \left[1 - \left(\frac{1 - e^{-\nu_c\Delta t}}{\nu_c\Delta t} \right) \right], \quad (3)$$

$$\alpha_1 = 2 \left[\frac{\cosh(\nu_c\Delta t) - 1}{(\nu_c\Delta t)^2} \right]. \quad (4)$$

The dispersion relations Eqs. (1) and (2) are used to determine the Fresnel coefficients for the interface between two dissimilar lattice spaces, as discussed in the next section.

2.3.1.2 FRESNEL COEFFICIENTS FOR A PLASMA LATTICE SPACE

Consider the interface between two dissimilar lattice spaces as shown in Fig. 1, where the region $z > 0$ is an ordinary lattice space with permittivity ϵ_1 and the region $z < 0$ is a plasma lattice space with parameters ω_p and ν_c . Let a plane wave be incident obliquely from the upper region. For simplicity, we consider the two-dimensional case, where the wavevector of the incident wave is (k_y, k_z) with $k_x = 0$. In order to determine the Fresnel coefficients R and T for the interface, we assume the following forms for the electric and magnetic fields in the upper and lower lattice spaces, respectively:

$$\left(\begin{array}{c} E_{y,p+\frac{1}{2},q}^n \\ E_{z,p,q+\frac{1}{2}}^n \\ H_{x,p+\frac{1}{2},q+\frac{1}{2}}^{n-\frac{1}{2}} \end{array} \right) \Big|_{\text{upper region}} = \begin{pmatrix} A_1 \\ B_1 \\ 1 \end{pmatrix} e^{j(\omega n \Delta t + p k_y \Delta y + q k_{z1} \Delta z_1)} + R \begin{pmatrix} -A_1 e^{j k_{z1} \Delta z_1} \\ B_1 \\ 1 \end{pmatrix} \times e^{j(\omega n \Delta t + p k_y \Delta y - q k_{z1} \Delta z_1)} , \quad (5)$$

$$\left(\begin{array}{c} E_{y,p+\frac{1}{2},q}^n \\ E_{z,p,q+\frac{1}{2}}^n \\ H_{x,p+\frac{1}{2},q+\frac{1}{2}}^{n-\frac{1}{2}} \end{array} \right) \Big|_{\text{lower region}} = T \begin{pmatrix} A_2 \\ B_2 \\ 1 \end{pmatrix} e^{j(\omega n \Delta t + p k_y \Delta y + q k_{z2} \Delta z_2)} , \quad (6)$$

where the coefficients A_i and B_i are determined by the finite-difference field equations for the upper ($i = 1$) and lower ($i = 2$) lattice spaces, respectively. Also, k_{z1} and k_{z2} are determined by the dispersion relations Eqs (1) and (2), respectively. From Fig. 1, it can be seen that there is an electric-field node right at the interface $z = 0$. The electric field $E_{y,p+\frac{1}{2},0}^n$ at this node is given by *neither* Eq. (5) *nor* Eq. (6). Instead, we assume it to have the following form

$$E_{y,p+\frac{1}{2},0}^n = F e^{j(\omega n \Delta t + p k_y \Delta y)} , \quad (7)$$

where F is another unknown.

Altogether, there are three unknowns in the above problem, namely, R , T and F . To solve for these unknowns, one needs three equations. Two of these equations are the finite-difference updating equations for the magnetic-field nodes marked N_1 and N_2 in Fig. 1, respectively,

$$\mu(1+R)(e^{j\omega\Delta t}-1) = \frac{\Delta t}{\Delta z_1} [A_1 e^{jk_{z1}\Delta z_1} (1 - Re^{-jk_{z1}\Delta z_1}) - F] - \frac{\Delta t}{\Delta y} B_1 (1+R) \times (e^{jk_y\Delta y} - 1) , \quad (8)$$

$$\mu T(e^{j\omega\Delta t}-1) = \frac{\Delta t}{\Delta z_2} e^{jk_{z2}\Delta z_2} (F - A_2 T e^{-jk_{z2}\Delta z_2}) - \frac{\Delta t}{\Delta y} T B_2 (e^{jk_y\Delta y} - 1) . \quad (9)$$

The third equation is obtained by apply Ampere's Law to the circuit encircling the electric-field node at the interface $z = 0$ and bounded by the magnetic-field nodes N_1 and N_2 :

$$\left[\left(\frac{\epsilon_1 \Delta z_1 + \epsilon_0 \Delta z_2}{2} \right) (e^{j\omega\Delta t} - 1) + \frac{\epsilon_0 \Delta z_2 \omega_p^2 (\Delta t)^2}{4} (e^{j\omega\Delta t} + 1) \left(\alpha_0 + \frac{\alpha_1}{e^{(j\omega + \nu_c)\Delta t} - 1} \right) \right] F = e^{j\omega\Delta t} \Delta t \left[(1+R) - T e^{-jk_{z2}\Delta z_2} \right] . \quad (10)$$

Eqs. (8) to (10) allow the Fresnel coefficients R and T , as well as the interfacial unknown F , to be solved. The numerical results are illustrated in Fig. 2, which shows the computed coefficients for a uniform lattice spacing of $\Delta y = \Delta z_1 = \Delta z_2 = \lambda/15$, which is the typical mesh spacing used in an FDTD simulation. Also shown in Fig. 2 are the Fresnel coefficients given by thin-film optics for continuous space. It can be seen that, at a mesh spacing of $\lambda/15$, there are significant differences between the coefficients for the lattice space and those for continuous space. To verify the correctness of the above formulation, we repeated the calculation for a uniform mesh spacing of $\lambda/100$. For such a small mesh spacing, we expect the results for the lattice space to converge to those for continuous space. This is indeed the case, as shown in Fig. 3.

The Fresnel coefficients for the lattice space must be separately computed by the above procedure for *each* of the several dozen Fourier components needed to characterize a finite-duration, pulse excitation. The corresponding multiply reflected waves of different frequencies inside the lattice substrate must afterwards be re-assembled to produce the correct time-domain excitation waveform at each point on the Huygens surface.

2.3.2 SECOND-ORDER ACCURATE DISCRETIZATION FOR THE PLASMA REGION

The plasma model of a dispersive medium was introduced by Luebbers, et al. [2]. However, the updating equation for the electric field given by these authors is only first-order accurate in time, due in part to the use of the rectangular rule for the convolution integral. In our implementation, however, the electric field is assumed to vary linearly with time between successive time steps and the resulting convolution integral is integrated exactly. This way, the following second-order accurate updating equation for the electric field has been derived [3]:

$$\mathbf{E}^{n+1} = \frac{1}{1 + \frac{1}{2}\omega_p^2\Delta t^2\alpha_0} \left\{ \left[1 - \frac{1}{2}\omega_p^2\Delta t^2 (\alpha_0 + \alpha_1 e^{-\nu_c\Delta t}) \right] \mathbf{E}^n - \frac{1}{2}\omega_p^2\Delta t^2 \Phi^n + \frac{\Delta t}{\epsilon_0} \text{curl } \mathbf{H}^{n+\frac{1}{2}} \right\} \quad (11)$$

where α_0 and α_1 are given by Eqs. (3) and (4), respectively, and the vector Φ^n is defined as

$$\Phi^n = \sum_{m=1}^{n-1} \alpha_1 \left(1 + e^{-\nu_c \Delta t}\right) e^{-\nu_c m \Delta t} \mathbf{E}^{n-m}, \quad (12)$$

which can be computed recursively by

$$\Phi^n = e^{-\nu_c \Delta t} \left[\alpha_1 \left(1 + e^{-\nu_c \Delta t}\right) \mathbf{E}^{n-1} + \Phi^{n-1} \right]. \quad (13)$$

Numerical experiments have indicated that Eq. (11) is more accurate than the first-order accurate updating equation given by Luebbers, et al. [2] which is used in most existing FDTD software packages.

2.3.3 NEAR-TO-FAR FIELD TRANSFORMATION

An FDTD computation only gives the fields in the near zone of the mask feature. To obtain the aerial image in the far zone, one must extrapolate the near-zone fields to the far zone using the Kirchhoff integral representation. In most existing FDTD software packages, this is accomplished by integrating the fields over a horizontal surface lying just outside the photomask blank on the projection-lens side. However, since the photomask blank extends essentially to infinity horizontally, it would in principle be necessary to integrate over an *infinite* horizontal surface to compute the far-zone fields, which is clearly impractical unless the geometry is artificially truncated by assuming periodic boundary conditions, as is usually done.

We have recently developed a near-to-far field transformation which does *not* assume periodic boundary conditions but yet requires only integration over a *finite* surface S , which we shall call the Kirchhoff surface, enclosing the mask feature of interest [4]. In this method, the electromagnetic vector potentials are expressed in terms of multilayered media Green's functions for the photomask substrate,

$$\mathbf{A}_e^{(1)}(\mathbf{r}) = \mu_0 \int_S \vec{\mathcal{G}}_E(\mathbf{r}|\mathbf{r}') \cdot \mathbf{J}_e(\mathbf{r}') dS', \quad (14)$$

$$\mathbf{A}_m^{(1)}(\mathbf{r}) = \epsilon_0 \int_S \left[\vec{\mathcal{G}}_M(\mathbf{r}|\mathbf{r}') \cdot \mathbf{J}_m(\mathbf{r}') + \nabla C_M(\mathbf{r}|\mathbf{r}') J_{mz}(\mathbf{r}') \right] dS', \quad (15)$$

where $\vec{\mathcal{G}}_E$ and $\vec{\mathcal{G}}_M$ are multilayered media Green's functions,

$$\vec{\mathcal{G}}_E(\mathbf{r}|\mathbf{r}') = (\mathbf{x}\mathbf{x} + \mathbf{y}\mathbf{y})G_{xx}^E(\mathbf{r}|\mathbf{r}') + \mathbf{z}\mathbf{x}G_{zx}^E(\mathbf{r}|\mathbf{r}') + \mathbf{z}\mathbf{y}G_{zy}^E(\mathbf{r}|\mathbf{r}') + \mathbf{z}\mathbf{z}G_{zz}^E(\mathbf{r}|\mathbf{r}') , \quad (16)$$

$$\vec{\mathcal{G}}_M(\mathbf{r}|\mathbf{r}') = (\mathbf{x}\mathbf{x} + \mathbf{y}\mathbf{y})G_{xx}^M(\mathbf{r}|\mathbf{r}') + \mathbf{z}\mathbf{x}G_{zx}^M(\mathbf{r}|\mathbf{r}') + \mathbf{z}\mathbf{y}G_{zy}^M(\mathbf{r}|\mathbf{r}') + \mathbf{z}\mathbf{z}G_{zz}^M(\mathbf{r}|\mathbf{r}') . \quad (17)$$

Using the technique of asymptotic evaluation of integrals, we have derived closed-form expression for the multilayered media Green's functions for the far-zone fields:

$$G_{xx}^E(\mathbf{r}|\mathbf{r}') = \frac{e^{jk_0 r}}{4\pi r} e^{-jk_0 \sin \theta (x' \cos \phi + y' \sin \phi)} \cos \theta W_i^{\text{TM}}(\theta, z') \quad (18)$$

$$G_{zx}^E(\mathbf{r}|\mathbf{r}') = \frac{e^{jk_0 r}}{4\pi r} e^{-jk_0 \sin \theta (x' \cos \phi + y' \sin \phi)} \csc \theta \cos \phi \left[W_i^{\text{TE}}(\theta, z') - \cos^2 \theta W_i^{\text{TM}}(\theta, z') \right] \quad (19)$$

$$G_{zy}^E(\mathbf{r}|\mathbf{r}') = \frac{e^{jk_0 r}}{4\pi r} e^{-jk_0 \sin \theta (x' \cos \phi + y' \sin \phi)} \csc \theta \sin \phi \left[W_i^{\text{TE}}(\theta, z') - \cos^2 \theta W_i^{\text{TM}}(\theta, z') \right] \quad (20)$$

$$G_{zz}^E(\mathbf{r}|\mathbf{r}') = \frac{e^{jk_0 r}}{4\pi r} e^{-jk_0 \sin \theta (x' \cos \phi + y' \sin \phi)} \frac{\epsilon_0}{\epsilon(z')} W_v^{\text{TE}}(\theta, z') \quad (21)$$

$$G_{xx}^M(\mathbf{r}|\mathbf{r}') = \frac{\epsilon(z')}{\epsilon_0} G_{zz}^E(\mathbf{r}|\mathbf{r}') \quad (22)$$

$$G_{zx}^M(\mathbf{r}|\mathbf{r}') = \frac{e^{jk_0 r}}{4\pi r} e^{-jk_0 \sin \theta (x' \cos \phi + y' \sin \phi)} \cot \theta \cos \phi \left[W_v^{\text{TM}}(\theta, z') - W_v^{\text{TE}}(\theta, z') \right] \quad (23)$$

$$G_{zy}^M(\mathbf{r}|\mathbf{r}') = \frac{e^{jk_0 r}}{4\pi r} e^{-jk_0 \sin \theta (x' \cos \phi + y' \sin \phi)} \cot \theta \sin \phi \left[W_v^{\text{TM}}(\theta, z') - W_v^{\text{TE}}(\theta, z') \right] \quad (24)$$

$$G_{zz}^M(\mathbf{r}|\mathbf{r}') = G_{xx}^E(\mathbf{r}|\mathbf{r}') \quad (25)$$

where

$$W_i^{\text{TM}}(\theta, z') = \frac{k_0 (1 - R_{01}^{\text{TM}})}{\gamma_1 (1 + R_{01}^{\text{TM}} R_{12}^{\text{TM}} e^{2j\gamma_1 d_1})} \begin{cases} e^{j\gamma_1 z'} + R_{12}^{\text{TM}} e^{j\gamma_1 (2d_1 - z')} , & 0 < z' < d_1 \\ (1 + R_{12}^{\text{TM}}) e^{j[\gamma_2 (z' - d_1) + \gamma_1 d_1]} , & z' > d_1 \end{cases} \quad (26)$$

$$W_i^{\text{TE}}(\theta, z') = \frac{\gamma_1 \epsilon_0 (1 + R_{01}^{\text{TE}})}{k_0 \epsilon_1 (1 + R_{01}^{\text{TE}} R_{12}^{\text{TE}} e^{2j\gamma_1 d_1})} \begin{cases} e^{j\gamma_1 z'} - R_{12}^{\text{TE}} e^{j\gamma_1 (2d_1 - z')} , & 0 < z' < d_1 \\ (1 - R_{12}^{\text{TE}}) e^{j[\gamma_2 (z' - d_1) + \gamma_1 d_1]} , & z' > d_1 \end{cases} \quad (27)$$

$$W_v^{\text{TE}}(\theta, z') = \frac{1 + R_{01}^{\text{TE}}}{1 + R_{01}^{\text{TE}} R_{12}^{\text{TE}} e^{2j\gamma_1 d_1}} \begin{cases} e^{j\gamma_1 z'} + R_{12}^{\text{TE}} e^{j\gamma_1 (2d_1 - z')} , & 0 < z' < d_1 \\ (1 + R_{12}^{\text{TE}}) e^{j[\gamma_2 (z' - d_1) + \gamma_1 d_1]} , & z' > d_1 \end{cases} \quad (28)$$

$$W_v^{\text{TM}}(\theta, z') = \frac{1 - R_{01}^{\text{TM}}}{1 + R_{01}^{\text{TM}} R_{12}^{\text{TM}} e^{2j\gamma_1 d_1}} \begin{cases} e^{j\gamma_1 z'} - R_{12}^{\text{TM}} e^{j\gamma_1 (2d_1 - z')} , & 0 < z' < d_1 \\ (1 - R_{12}^{\text{TM}}) e^{j[\gamma_2 (z' - d_1) + \gamma_1 d_1]} , & z' > d_1 \end{cases} \quad (29)$$

and d_1 is the thickness of the chromium layer.

2.4. ALGORITHMIC IMPLEMENTATION

In this section, we discuss how the mathematical formulation discussed in Section 3 has been implemented in computer code.

For a given angle of incidence and polarization, the program reads in the geometry description contained in an input file and then proceeds to set up a finite-difference computational mesh and calculate the various parameters used in the updating equations for the electric and magnetic fields at each node. Next, the incident pulse waveform is decomposed into Fourier components. For each Fourier component, the dispersion relations in the various material regions are evaluated using Eqs.

(1) and (2). The results are substituted into the system of equations Eqs. (8) to (10) for each material interface in the multilayered photomask substrate. These equations are solved for the Fresnel coefficients R and T associated with that material interface. Using these coefficients, the steady-state field distribution in the photomask substrate for the particular Fourier component is computed and stored at all the points on the Huygens surface. This process is repeated for all the Fourier components of the incident waveform. Afterwards, the stored frequency response at each point on the Huygens surface is converted into a time-domain waveform by inverse Fourier transformation. This completes the initialization of the incident excitation on the Huygens surface.

The program then enters the main FDTD time-marching loop. The fields in the entire computational domain are initialized to zero. At the start of the n^{th} time step, the magnetic field components at all the magnetic-field nodes in the domain are updated to their values at time step $n + \frac{1}{2}$. The incident excitation for time step $n + \frac{1}{2}$ is then applied to the magnetic-field nodes on the Huygens surface. Next, the electric field components at all the electric-field nodes in the domain are updated to their values at time step $n + 1$. For electric-field nodes lying in the chromium region of the photomask structure, the second-order accurate equation Eq. (11) is used, while for the remaining electric-field nodes, the standard FDTD updating equation is used. The incident excitation for time step $n + 1$ is then applied to the electric-field nodes on the Huygens surface. The nodes on the outermost boundaries of the computational domain have yet to be updated. An absorbing boundary condition (ABC) is needed for this purpose. Various ABCs are available in the literature, from simple but less accurate ones, such as the Mur ABC, to sophisticated and highly accurate ones, such as Berenger's Perfectly Matched Layer. In our code, we have used the first-order Higdon ABC, which has been shown to give accurate results provided that the mask feature under investigation is separated from the outermost boundaries by a distance of at least one wavelength. After updating the fields on the outermost boundaries using the Higdon ABC, the FDTD loop for the n^{th} time step is completed. Before proceeding with the next time step, however, the discrete Fourier transform of the field at each node on the Kirchhoff surface S is computed recursively and saved. This way, upon completion of the FDTD loop for all the time steps, we shall immediately have available the steady-state response of the system at each point on the Kirchhoff surface, which has been used in the subsequent near-to-far field transformation.

Since a pulse of finite-duration is used for excitation, the fields in the computational domain eventually decays with time. When the fields have decayed to a sufficiently low level, the FDTD time-marching loop is exited. The computed steady-state fields on the Kirchhoff surface are then written to an output file and the FDTD program terminates. Another program is executed to perform the near-to-far field transformation on the output of the FDTD program. The program computes the far-zone fields at selected points on the entrance pupil of the projection lens using Eqs. (14) to (29). Then, the fields on the entrance pupil are propagated to the exit pupil, and from there to the wafer plane, by using the vector aerial image model [5].

The above calculations is being repeated for different angles of incidence in order to simulate the effects of partial coherence. This process has been automated by the use of shell scripts to control program execution. It should also be pointed out that our data structure has been designed in such a way as to facilitate future upgrading of the FDTD algorithm used for this work to the more powerful hybrid finite-element and finite-difference time-domain algorithm [6].

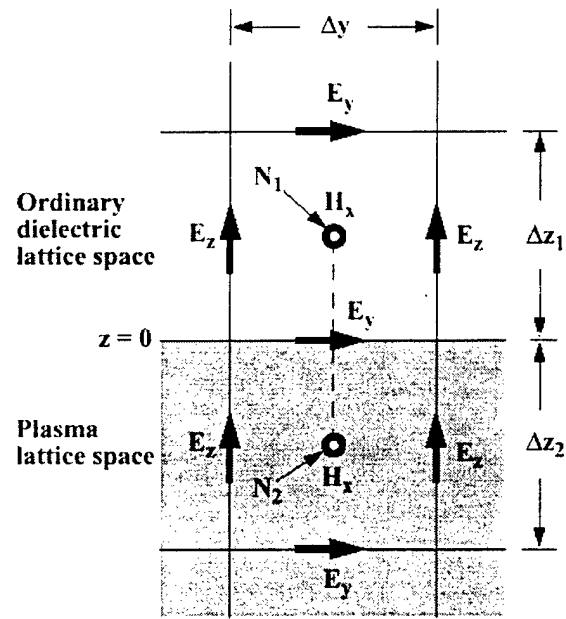


Fig. 1. Interface between an ordinary dielectric lattice space and a plasma lattice space.

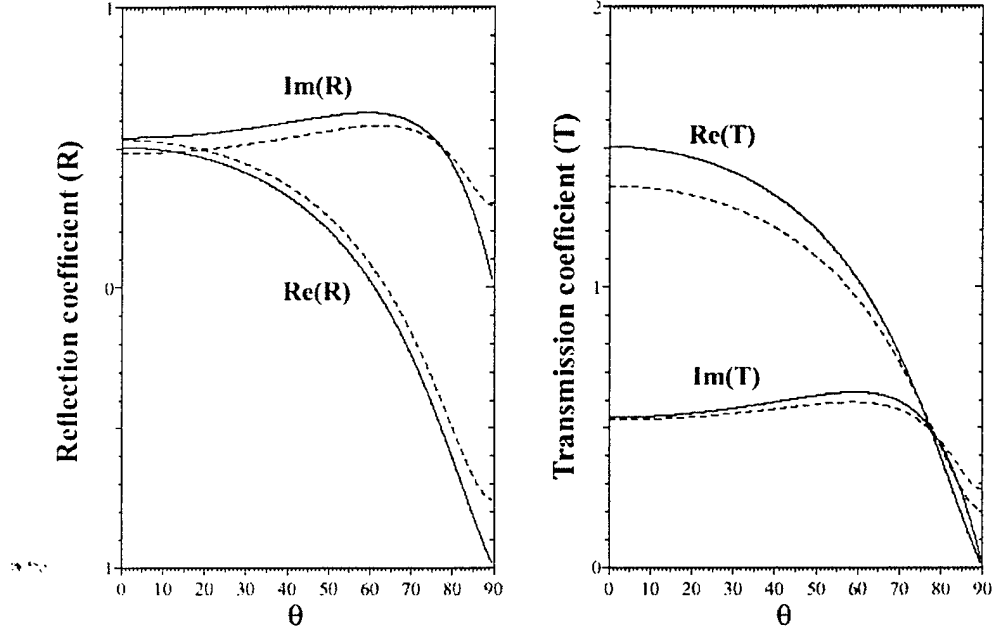


Fig. 2. Reflection and transmission coefficients for the interface between air and a plasma material with $n = 0.85 + 2.01j$. Dashed lines are for discrete lattice spaces with a uniform lattice spacing of $\Delta = \lambda/15$. Solid lines are for continuous space

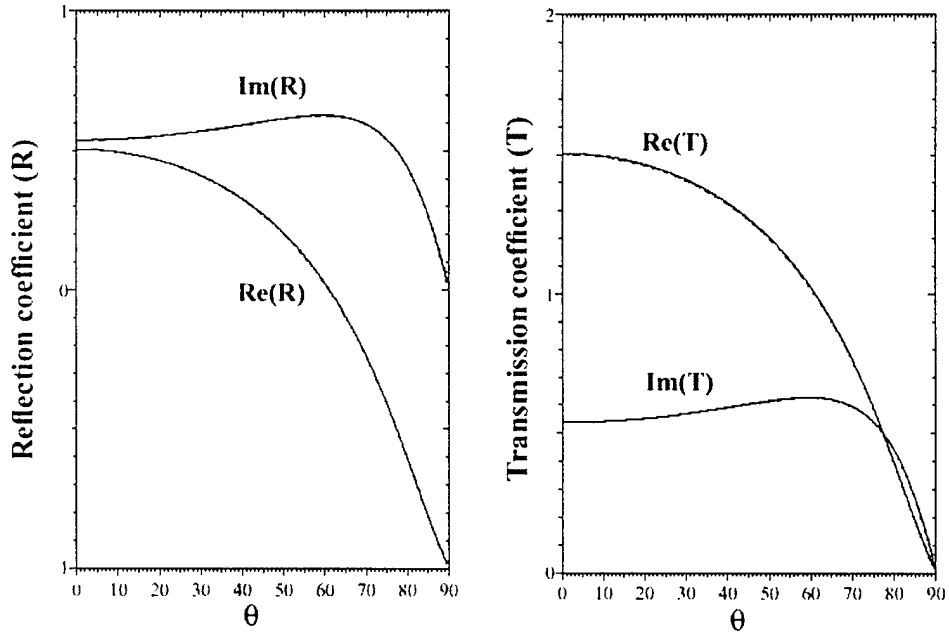


Fig. 3. Same as Fig. 2, but for a uniform lattice spacing of $\Delta = \lambda/100$.

BIBLIOGRAPHY

- [1] R. Holland and J. W. Williams, "Total-field versus scattered-field finite-difference codes: A comparative assessment", *IEEE Trans. Nuclear Science*, Vol. 30, pp. 4583-4588 (1983).
- [2] R. J. Luebbers, F. Hunsberger and K. S. Kunz, "A frequency-dependent finite-difference time-domain formulation for transient propagation in plasma", *IEEE Trans. Antennas Propagat.*, Vol. 39, pp. 29-34 (1991).
- [3] M. S. Yeung and E. Barouch, "Application of the hybrid finite-difference time-domain method to modeling curved surfaces in three-dimensional lithography simulation", *Proc. SPIE*, Vol. 3679 (1999).
- [4] M. S. Yeung and E. Barouch, "Three-dimensional mask transmission simulation using a single integral equation method", *Proc. SPIE*, Vol. 3334, pp. 704-713 (1998).
- [5] M. S. Yeung, "Modeling high numerical aperture optical lithography", *Proc. SPIE*, Vol. 922, pp. 149-167 (1988).
- [6] M. S. Yeung, "Application of the hybrid FDTD-FETD method to dispersive materials", to appear in the November 20, 1999, issue of *Microwave and Optical Technology Letters*.

APPENDIX

APPLICATION OF THE HYBRID FINITE-DIFFERENCE TIME-DOMAIN METHOD TO MODELING CURVED SURFACES IN THREE-DIMENSIONAL LITHOGRAPHY SIMULATION

1. INTRODUCTION

Electromagnetic scattering from nonplanar topography on the mask or wafer can have a significant impact on photomask performance, linewidth control or alignment precision. Computer simulation is a cost-effective way to assess the importance of such electromagnetic scattering effects in photolithography. With the scaling of devices to smaller dimensions, greater demands are placed on the accuracy of the mathematical models used in the electromagnetic simulators and the efficiency of their numerical implementation.

Over the past many years, the finite-difference time-domain method (FDTD) has become the prevalent method for solving electromagnetic scattering problems. Not only is it generally applicable to arbitrary geometries, but also it is the most efficient algorithm available, by yielding useful field information at N space points and m time points in a total of only $O(mN)$ operations. Thus, for example, a single time-domain simulation of the response of an electromagnetic system to a finite-duration incident pulse can yield the steady-state results for a large number of different frequencies by Fourier transformation.

The main disadvantage of FDTD is its inefficiency in modeling curved surfaces accurately, since the regular finite-difference mesh used in FDTD requires that curved surfaces be approximated by staircase models. To achieve accurate results using the staircase model, one usually has to use a very fine mesh and, therefore, also a very small time step due to the stability criterion.

Recently, a hybrid-FDTD method appeared in the literature [1] which combines the flexibility of the finite-element method (FEM) in modeling curved surfaces accurately with the computational efficiency of FDTD. It appears that this hybrid-FDTD method, when used in conjunction with high-performance absorbing boundary conditions, is the ideal tool for solving three-dimensional electromagnetic scattering problems arising in lithography simulation accurately and efficiently.

However, the hybrid-FDTD method in its original form is not suitable for DUV lithography simulation. This is because the original formulation cannot handle lossy materials, especially those with negative dielectric constants, such as chromium and silicon, which are commonplace in DUV lithography. The goal of this paper is to extend the original hybrid-FDTD formulation to handle lossy materials.

After reviewing the original hybrid-FDTD formulation in Section 2.1, we discuss its extensions to lossy materials with positive and negative dielectric constants separately in Sections 2.2 and 2.3.

The issues of mesh generation are discussed briefly in Section 3.1. This is followed in Section 3.2 by a presentation of numerical results comparing the hybrid-FDTD method and standard FDTD for various dielectric materials.

2. THE HYBRID-FDTD METHOD

2.1 THE ORIGINAL METHOD

The hybrid-FDTD method was originally developed by Wu and Itoh [1] for lossless dielectric objects. Consider a dielectric object bounded by a curved surface S as shown in Fig. 1. The computational domain is divided into two overlapping regions: (i) A regular finite-difference region Ω_1 spanning the interior and exterior of the object at some distance from the surface S , and (ii) an irregular finite-element region Ω_2 spanning the immediate vicinity of S on both of its sides. The two regions overlap in a single layer of finite-difference cells bounded by staircase surfaces Γ_1 and Γ_2 on each side of S .

Suppose the electric field \mathbf{E}^n is known everywhere at time step n . Using the standard Yee algorithm [2], the magnetic field $\mathbf{H}^{n+\frac{1}{2}}$ at time step $n + \frac{1}{2}$ in the regular region Ω_1 , including the overlap region, can be updated. This in turn allows the electric field \mathbf{E}^{n+1} in Ω_1 , including the boundary Γ_1 , to be updated. The electric field \mathbf{E}^{n+1} in the irregular region Ω_2 is then updated by solving the weighted-residual problem

$$\frac{\partial^2}{\partial t^2} \int_{\Omega} \epsilon \mathbf{E}^a \cdot \mathbf{E} d\Omega = - \int_{\Omega} \frac{1}{\mu} \nabla \times \mathbf{E}^a \cdot \nabla \times \mathbf{E} d\Omega , \quad (1)$$

using the electric field \mathbf{E}^{n+1} on Γ_1 as boundary condition and the previous electric fields \mathbf{E}^n and \mathbf{E}^{n-1} in Ω_2 as initial condition. Once the electric field at time step $n + 1$ becomes available everywhere, the time-marching can be continued for the next time step.

To solve the weighted-residual problem Eq. (1), the irregular region Ω_2 is subdivided into many small tetrahedral elements and the electric field in the elements is expanded in Whitney vector basis functions \mathbf{W}_j [3], with the electric field components E_j along the element edges j as the expansion coefficients. Next, the time derivative in Eq. (1) is approximated by the central difference operator and the Newmark-Beta method [1] is applied to obtain an unconditionally stable, second-order accurate, implicit time-marching scheme,

$$\left([C] + \frac{\Delta t^2}{4} [D] \right) \bar{\mathbf{E}}^{n+1} = 2 \left([C] - \frac{\Delta t^2}{4} [D] \right) \bar{\mathbf{E}}^n - \left([C] + \frac{\Delta t^2}{4} [D] \right) \bar{\mathbf{E}}^{n-1} . \quad (2)$$

Here the matrices $[C]$ and $[D]$ are given by

$$[C]_{ij} = \int_{\Omega} \epsilon_0 \epsilon_r \mathbf{W}_i \cdot \mathbf{W}_j d\Omega , \quad (3)$$

$$[D]_{ij} = \int_{\Omega} \frac{1}{\mu} \nabla \times \mathbf{W}_i \cdot \nabla \times \mathbf{W}_j d\Omega , \quad (4)$$

where ϵ_r is the dielectric constant and \bar{E}^n is the vector of expansion coefficients at time step n .

The above formulation of Wu and Itoh is applicable only to lossless dielectric objects with positive dielectric constants ϵ_r . The objects encountered in lithography simulation, however, are often lossy and, furthermore, may have negative dielectric constants, especially at DUV wavelengths. We next discuss the extensions of the formulation of Wu and Itoh to lossy media with positive and negative dielectric constants separately.

2.2 EXTENSION TO LOSSY MEDIUM WITH POSITIVE DIELECTRIC CONSTANT

A material with positive dielectric constant is one for which the real part n of its complex refractive index is greater than the imaginary part κ . Such is the case for weakly absorbing materials such as photoresist and silicon nitride. This kind of material can be modeled in the time domain by adding a conductivity term to the electric-field updating equation. The dielectric constant ϵ_r and conductivity σ are related to the complex refractive index $n + j\kappa$ by

$$\epsilon_r = n^2 - \kappa^2 , \quad (5)$$

$$\sigma = 2n\kappa \omega_0 \epsilon_0 \epsilon_r , \quad (6)$$

where ω_0 is the frequency of interest.

By using exponential time stepping [4], the updating equation for the electric field in the irregular region becomes

$$\left([C_+] + \frac{\Delta t^2}{4} [D] \right) \bar{E}^{n+1} = 2 \left([C_0] - \frac{\Delta t^2}{4} [D] \right) \bar{E}^n - \left([C_-] + \frac{\Delta t^2}{4} [D] \right) \bar{E}^{n-1} , \quad (7)$$

where the matrices $[C_{\pm}]$ and $[C_0]$ are given by

$$[C_{\pm}]_{ij} = \int_{\Omega} \epsilon_0 \epsilon_r \exp \left(\pm \frac{\sigma \Delta t}{2\epsilon_0 \epsilon_r} \right) \mathbf{W}_i \cdot \mathbf{W}_j d\Omega , \quad (8)$$

$$[C_0]_{ij} = \int_{\Omega} \epsilon_0 \epsilon_r \cosh \left(\frac{\sigma \Delta t}{2\epsilon_0 \epsilon_r} \right) \mathbf{W}_i \cdot \mathbf{W}_j d\Omega . \quad (9)$$

The time-marching scheme Eq. (7) is unconditionally stable as long as $\epsilon_r > 0$.

2.3 EXTENSION TO LOSSY MEDIUM WITH NEGATIVE DIELECTRIC CONSTANT

A material for which $n < \kappa$ has a negative dielectric constant according to Eq. (5). Silicon, chromium and tungsten are examples of such materials at DUV wavelengths. This type of material

can be modeled in the time domain by an unmagnetized plasma [5], with a complex dielectric function

$$\epsilon_r(\omega) = 1 - \frac{\omega_p^2}{\omega(\omega + j\nu_c)} . \quad (10)$$

The plasma frequency ω_p and collision frequency ν_c appearing in Eq. (10) are related to the complex refractive index of the material at the frequency ω_0 of interest by

$$\frac{\omega_p^2}{\omega_0^2} = 1 + \kappa^2 - n^2 + \frac{4n^2\kappa^2}{1 + \kappa^2 - n^2} , \quad (11)$$

$$\frac{\nu_c}{\omega_0} = \frac{2n\kappa}{1 + \kappa^2 - n^2} . \quad (12)$$

The weighted-residual problem to be solved in the irregular plasma region is

$$\begin{aligned} \frac{\partial^2}{\partial t^2} \int_{\Omega} \epsilon_0 \mathbf{E}^a \cdot \mathbf{E} d\Omega &= - \int_{\Omega} \frac{1}{\mu} \nabla \times \mathbf{E}^a \cdot \nabla \times \mathbf{E} d\Omega - \int_{\Omega} \omega_p^2 e^{-\nu_c t} \mathbf{E}^a \cdot \mathbf{E} d\Omega \\ &+ \int_{-\infty}^t dt' \int_{\Omega} \nu_c \omega_p^2 e^{-\nu_c t'} \mathbf{E}^a \cdot \mathbf{E}(t - t') d\Omega , \end{aligned} \quad (13)$$

in which a convolution term appears due to the frequency dependence of the plasma dielectric function Eq. (10). Expanding the electric field \mathbf{E} in Whitney basis functions and applying the Newmark-Beta method, we obtain the following second-order accurate, implicit time-marching scheme:

$$\begin{aligned} \left([C] + \frac{\Delta t^2}{4} \{ [D] + [\chi^{(1)}] \} \right) \bar{E}^{n+1} &= 2 \left([C] - \frac{\Delta t^2}{4} \{ [D] + [\chi^{(1)}] \} \right) \bar{E}^n \\ &- \left([C] + \frac{\Delta t^2}{4} \{ [D] + [\chi^{(1)}] \} \right) \bar{E}^{n-1} + \bar{\Psi}^n , \end{aligned} \quad (14)$$

where $[C]$ is given by Eq. (3) with $\epsilon_r = 1$ and the matrix $[\chi^{(1)}]$ is given by

$$[\chi^{(1)}]_{ij} = \int_{\Omega} \left(\frac{1 - e^{-\nu_c \Delta t}}{\nu_c \Delta t} \right) \mathbf{W}_i \cdot \mathbf{W}_j d\Omega , \quad (15)$$

The vector $\bar{\Psi}^n$ appearing in Eq. (14) is defined as

$$\bar{\Psi}^n = \sum_{m=1}^{n-1} [\chi_m^{(2)}] \bar{E}^{n-m} , \quad (16)$$

where the matrix $[\chi_m^{(2)}]$ is given by

$$[\chi_m^{(2)}]_{ij} = \int_{\Omega} 2 \left[\frac{\cosh(\nu_c \Delta t) - 1}{\nu_c \Delta t} \right] \omega_p^2 \Delta t^2 e^{-\nu_c m \Delta t} \mathbf{W}_i \cdot \mathbf{W}_j d\Omega . \quad (17)$$

Using the technique of Luebbers et al. [5], the vector $\bar{\Psi}^n$ can be computed recursively by

$$\bar{\Psi}^n = [\chi_1^{(2)}] \bar{E}^{n-1} + e^{-\nu_c \Delta t} \bar{\Psi}^{n-1} . \quad (18)$$

The same plasma model Eq. (10) can be applied to the regular FDTD region in the interior of the object. However, the traditional FDTD implementation of this model [5] is only first-order accurate in time, due in part to the use of the rectangular rule for the convolution integral. Instead, by assuming the electric field to vary linearly with time between successive time steps and performing the resulting convolution integral exactly, the following second-order accurate updating equation for the electric field in the interior FDTD region is obtained:

$$\mathbf{E}^{n+1} = \frac{1}{1 + \frac{1}{2} \omega_p^2 \Delta t^2 \alpha_0} \left\{ \left[1 - \frac{1}{2} \omega_p^2 \Delta t^2 (\alpha_0 + \alpha_1 e^{-\nu_c \Delta t}) \right] \mathbf{E}^n - \frac{1}{2} \omega_p^2 \Delta t^2 \Phi^n + \frac{\Delta t}{\epsilon_0} \text{curl } \mathbf{H}^{n+\frac{1}{2}} \right\} \quad (19)$$

where

$$\alpha_0 = \frac{1}{\nu_c \Delta t} \left[1 - \left(\frac{1 - e^{-\nu_c \Delta t}}{\nu_c \Delta t} \right) \right] , \quad (20)$$

$$\alpha_1 = 2 \left[\frac{\cosh(\nu_c \Delta t) - 1}{(\nu_c \Delta t)^2} \right] . \quad (21)$$

The vector Φ^n appearing in Eq. (19) is defined as

$$\Phi^n = \sum_{m=1}^{n-1} \alpha_1 (1 + e^{-\nu_c \Delta t}) e^{-\nu_c m \Delta t} \mathbf{E}^{n-m} , \quad (22)$$

and can be computed recursively by

$$\Phi^n = e^{-\nu_c \Delta t} [\alpha_1 (1 + e^{-\nu_c \Delta t}) \mathbf{E}^{n-1} + \Phi^{n-1}] . \quad (23)$$

To our knowledge, the second-order accurate updating equation Eq. (19) has not appeared before in the literature.

3. RESULTS

We tested the formulations discussed in Sections 2.1 to 2.3 with the problem of electromagnetic scattering by a dielectric sphere, for which the exact solution is known. The diameter of the sphere was $0.06 \mu\text{m}$ and the wavelength was $0.248 \mu\text{m}$.

3.1 MESH GENERATION

The first step in the computation was to generate a high-quality mesh for the three-dimensional irregular region Ω_2 shown in Fig. 1. After subdividing the surface of the sphere into a large number of small triangles, an unstructured tetrahedral mesh was generated in Ω_2 conforming to the surface triangulation of the sphere and the staircase boundaries Γ_1 and Γ_2 , using our automatic mesh-generation software.

The quality Q of our mesh was measured by the *minimum* of the sines of all the dihedral angles in the mesh, where $0 \leq Q \leq 1.0$. This quality measure was chosen to bias against elements with too large ($\theta_{\min} \approx 180^\circ$) or too small ($\theta_{\min} \approx 0^\circ$) dihedral angles, which would lead to poor accuracy of the finite-element interpolation or poor conditioning of the finite-element matrix, respectively [6]. It was found that our as-generated mesh had a quality Q of only 0.073, indicating the presence of poorly shaped elements in the mesh.

To remove the poorly shaped elements, we performed mesh improvement on the as-generated mesh in two steps. In the first step, the sub-mesh belonging to each *edge* in the mesh, consisting of all the tetrahedra adjacent to that edge, was examined. The edge was deleted and replaced by one or more new edges if, by doing so, the quality of the sub-mesh was improved. In the second step, the cluster belonging to each *node*, consisting of all the tetrahedra adjacent to that node and its nearest neighbors, was examined. If the quality of the cluster was below a certain threshold, the nodes in the cluster were moved to new positions which maximized the quality of the cluster. It was found that after a single pass through our mesh-improvement routine, the quality of the mesh increased to $Q = 0.335$, which was deemed satisfactory for our computation. The final mesh is shown in Fig. 2 and consists of 1195 nodes, 7158 edges and 5485 tetrahedra.

The above finite-element mesh was embedded in a regular finite-difference mesh with $20 \times 20 \times 20$ cells. For simplicity, the first-order Higdon absorbing boundary condition [8] was used on all six sides of the computational domain, which measured $0.2 \mu\text{m} \times 0.2 \mu\text{m} \times 0.2 \mu\text{m}$. A Huygens surface [9] located two cells interior to the outermost boundaries was used to excite the domain with various Gaussian pulses.

3.2 NUMERICAL RESULTS

3.2.1 LOSSLESS DIELECTRIC

We first compared our results with those of Wu and Itoh, who used a lossless dielectric sphere of refractive index $n_1 = 3.0$ and a Gaussian pulse with finite d.c. content,

$$\mathbf{E}_{\text{inc}}^n = \hat{\mathbf{x}} e^{-\left[3\left(\frac{n}{n_0}-1\right)\right]^2}, \quad (24)$$

where $n_0 = 33$. The computed results are shown in Fig. 3. Fig. 3a shows the total time-domain waveform at the center of the sphere, while Fig. 3b shows the scattered waveform at a point $0.09 \mu\text{m}$ in front of the sphere. Also shown in the figures are the exact Mie solution [7] and the results obtained with standard FDTD using the same mesh spacing as hybrid-FDTD in the regular region Ω_1 , namely, $20 \times 20 \times 20$ cells, or roughly $1/8$ of the wavelength n_1 inside the dielectric. The

results of Figs. 3a and 3b are in good agreement with those of Wu and Itoh [1]. This verifies the correctness of our computer program.

Next, the frequency-domain scattering cross section was obtained by Fourier transformation of the corresponding time-domain result. The hybrid-FDTD result is shown in Fig. 3c, together with the exact Mie solution and the results obtained with standard FDTD using $20 \times 20 \times 20$ and $40 \times 40 \times 40$ cells, respectively. It can be seen that, compared with the exact result, the hybrid-FDTD method with a coarse mesh spacing of $\lambda_1/8$ gave much better accuracy than FDTD with the same mesh spacing, and roughly the same accuracy as FDTD with the finer mesh spacing of $\lambda_1/16$. The small discrepancy between the hybrid-FDTD result and the exact result is due in part to the approximate absorbing boundary conditions used.

3.2.2 LOSSY DIELECTRIC WITH POSITIVE DIELECTRIC CONSTANT

We tested the formulation of Section 2.2 by using a lossy dielectric sphere of refractive index $n_1 = 2.0 + j0.5$. The time derivative of a Gaussian pulse was used for excitation to avoid introducing a d.c. offset into the solution,

$$\mathbf{E}_{\text{inc}}^n = -\hat{\mathbf{x}} 3\sqrt{2}e \left(\frac{n}{n_0} - 1 \right) e^{-\left[3\left(\frac{n}{n_0} - 1 \right) \right]^2}, \quad (25)$$

where $n_0 = 33$. The computed time-domain waveforms are shown in Figs. 4a and 4b, together with the exact results and the results obtained with standard FDTD using the same mesh spacing as hybrid-FDTD, or roughly 1/12 of the wavelength inside the dielectric. It can be seen that the hybrid-FDTD and FDTD results are both in good agreement with the exact results, although the FDTD results have slightly more overshooting at the valleys of the waveforms.

The result for the Fourier transformed scattering cross section is shown in Fig. 4c, together with the FDTD results obtained with a coarse and a fine mesh spacing. It can be seen that, as in the lossless dielectric case, the hybrid-FDTD method with a coarse mesh spacing of $\lambda_1/12$ gave much better accuracy than FDTD with the same mesh spacing, and roughly the same accuracy as FDTD with the finer mesh spacing of $\lambda_1/24$.

3.2.3 LOSSY DIELECTRIC WITH NEGATIVE DIELECTRIC CONSTANT

We tested the formulation of Section 2.3 by using a lossy dielectric sphere of refractive index $n_1 = 0.85 + j2.01$, which is the refractive index of chromium at $0.248 \mu\text{m}$ [10]. The time-derivative Gaussian pulse Eq. (25) with zero d.c. content was used for excitation to avoid the singularity of the plasma dielectric function Eq. (10) at $\omega = 0$.

The computed time-domain waveforms are shown in Figs. 5a and 5b, together with the exact results and the results obtained with standard FDTD using the same mesh spacing as hybrid-FDTD, or roughly 1/29 of the wavelength inside the dielectric sphere. It can be seen that, whereas the hybrid-FDTD results are in good agreement with the exact results for all times, the FDTD results show marked departures from the exact results at late times.

The result for the Fourier transformed scattering cross section is shown in Fig. 6, together with the FDTD results obtained with a coarse, a fine and a *very* fine mesh spacing. It can be seen that, whereas the hybrid-FDTD result is in good agreement with the exact result, the FDTD results for all three mesh spacings, namely, $\lambda_1/29$, $\lambda_1/58$ and $\lambda_1/116$, show large departures from the exact result. Since the second-order accurate updating equation Eq. (19) was used for the FDTD computations, these departures cannot be due to inaccurate implementation of the plasma dispersion model of Section 2.3, but, rather, must be due to inaccuracy of the staircase model of the spherical surface used in standard FDTD. These results highlight the need to use the hybrid-FDTD method to model curved surfaces accurately in the case of lossy dielectric materials with negative dielectric constants.

4. CONCLUSIONS

Extensions of the original hybrid-FDTD method to handle lossy materials with positive and negative dielectric constants have been discussed separately. The correctness of our computer program has been verified by comparing our computed results with those in the literature and with the exact results. Our results have shown that, for lossless dielectric and lossy material with positive dielectric constant, the hybrid-FDTD method is much more accurate than standard FDTD when the same mesh spacing is used in both methods, while the two methods have roughly the same accuracy when the mesh spacing used in standard FDTD is half that used in hybrid-FDTD. For lossy material with negative dielectric constant, the difference between the two methods is much more pronounced. In this case, the hybrid-FDTD method with a mesh spacing of Δ is much more accurate than standard FDTD even when a mesh spacing of $\frac{1}{4}\Delta$ is used in the latter method. These results indicate that the hybrid-FDTD method is far superior to standard FDTD for lithography simulation at DUV wavelengths, where lossy materials with negative dielectric constants are commonplace.

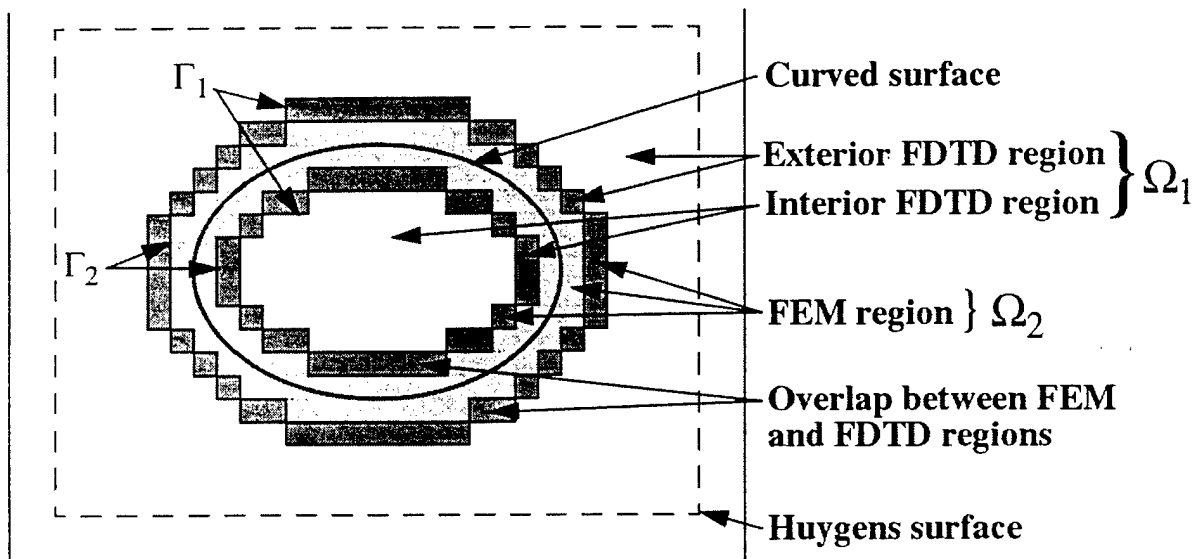


Fig. 1. The hybrid-FDTD computational domain consisting of overlapping FDTD (Ω_1) and FEM (Ω_2) regions. Γ_1 and Γ_2 are the exterior and secondary boundaries, respectively, of the overlap region. An incident wave is applied to the Huygens surface.

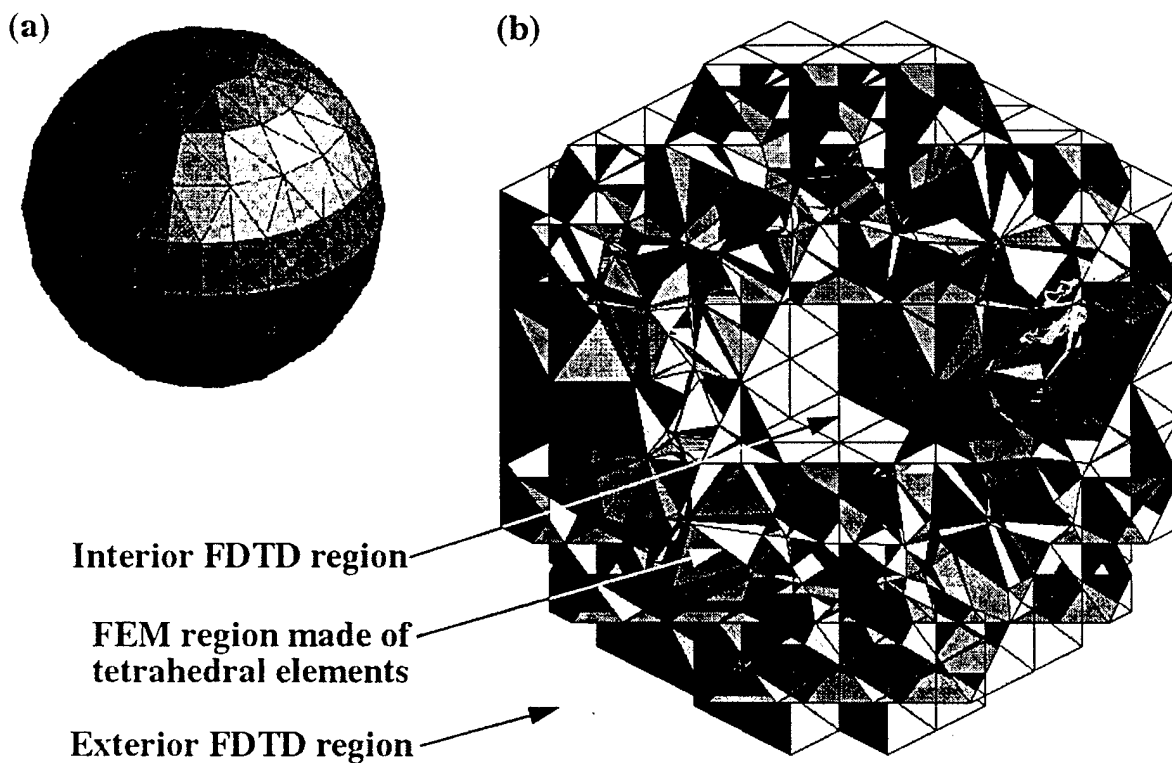


Fig. 2. (a) The surface of a sphere of diameter $0.06 \mu\text{m}$ modeled by 352 triangles. (b) Cutaway view of the FEM mesh consisting of 5485 tetrahedral elements.

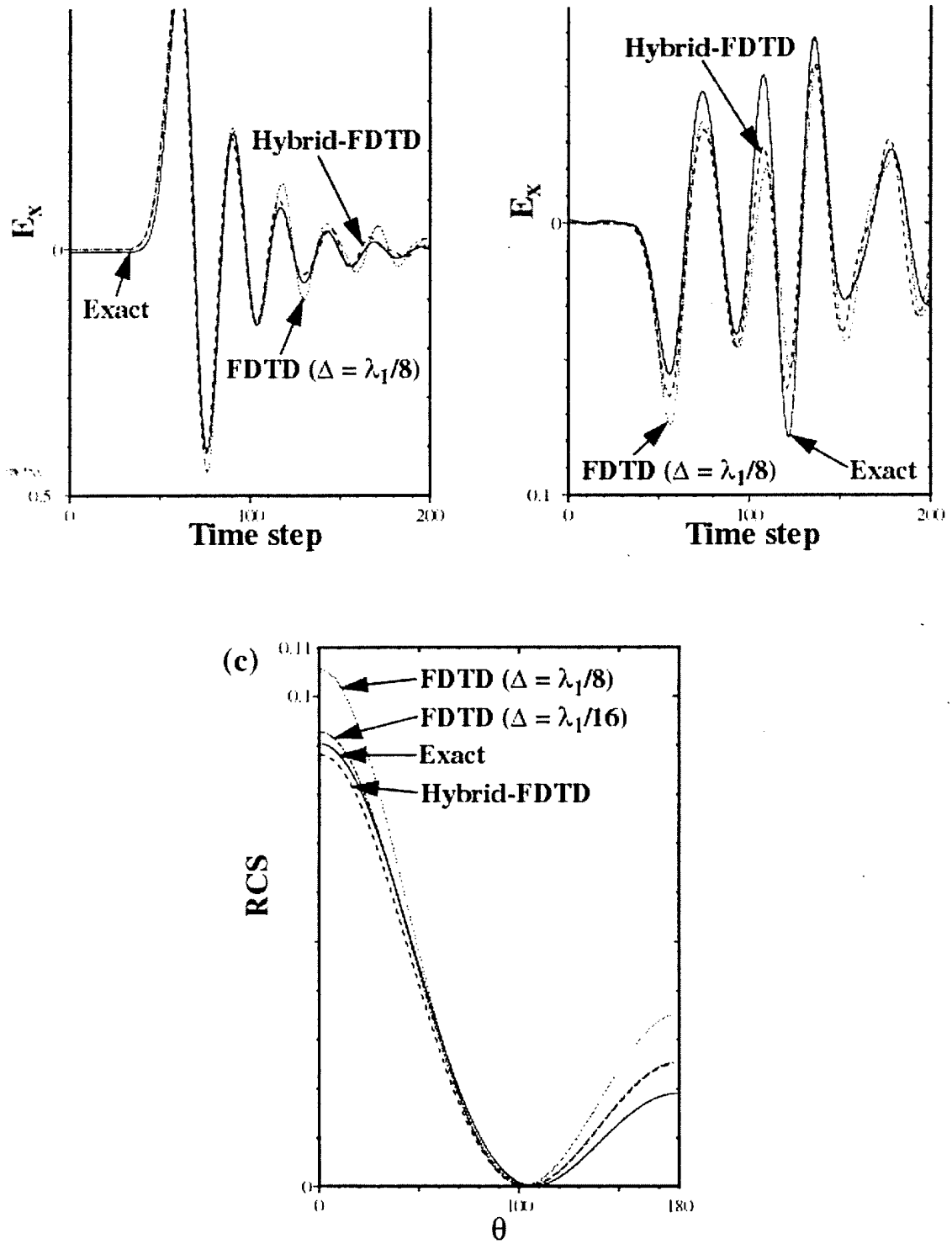


Fig. 3. Results for a lossless dielectric sphere of refractive index $n_1 = 3.0$. (a) and (b): Time domain waveforms at center of sphere and at a point $0.09 \mu\text{m}$ in front of the sphere. (c): Radar cross section obtained by Fourier transformation of the time-domain result

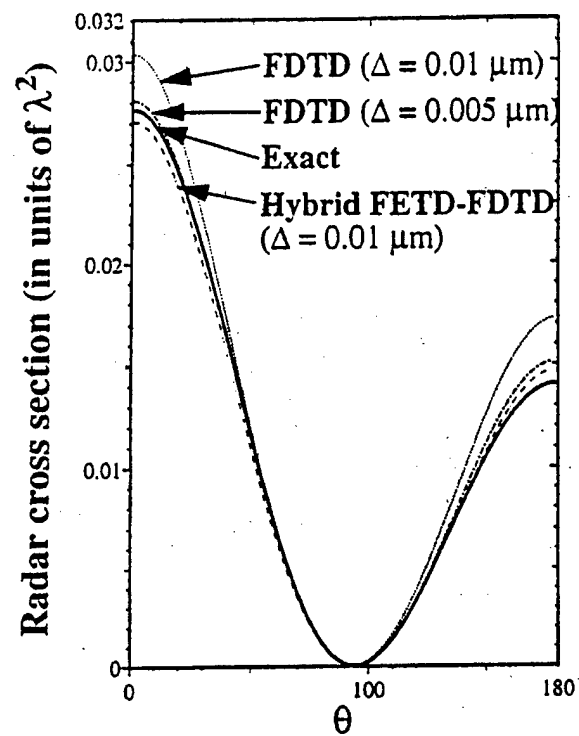


Fig. 4. Radar cross section of a lossy sphere of refractive index $2.0 - 0.5j$, obtained by Fourier transformation of the time-domain results.

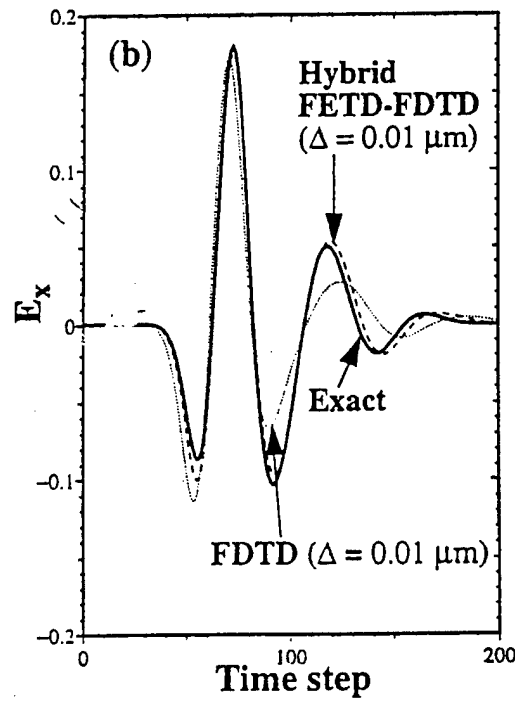
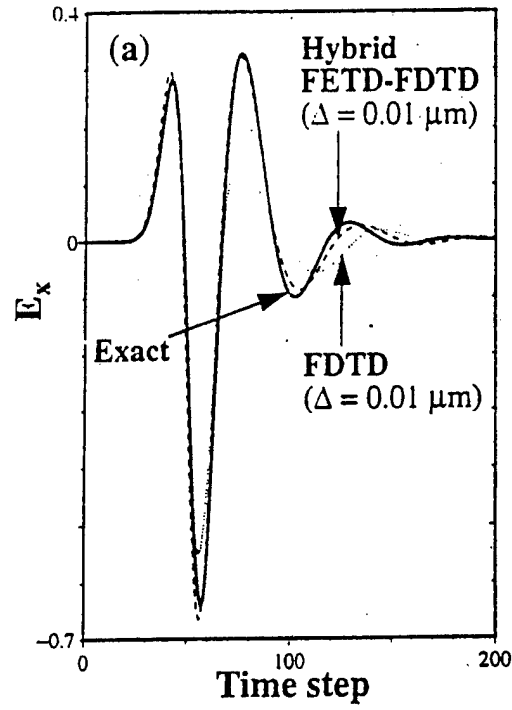


Fig. 5. Time-domain waveforms for a lossy sphere of refractive index $0.85 - 2.01j$, modeled by a plasma model. (a) Total wave at the center of the sphere. (b) Scattered wave at a point $0.09 \mu\text{m}$ in front of the sphere.

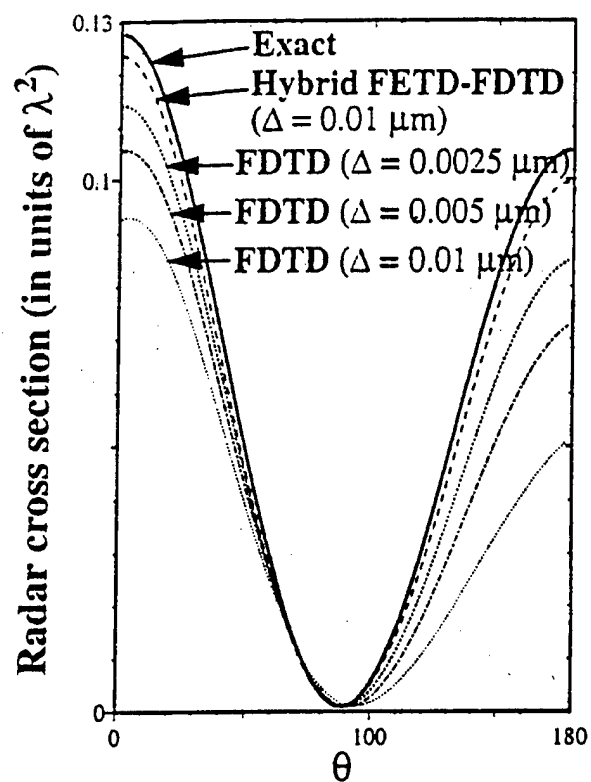


Fig. 6. Radar cross section of a lossy sphere of refractive index $0.85 - 2.01j$, obtained by Fourier transformation of the time-domain results.

BIBLIOGRAPHY

- [1] R. B. Wu and T. Itoh, "Hybrid finite-difference time-domain modeling of curved surfaces using tetrahedral edge elements", *IEEE Trans. Antennas Propagat.*, Vol. 45, pp. 1302-1309 (1997).
- [2] K. S. Yee, "Numerical solution of initial boundary value problems in isotropic media", *IEEE Trans. Antennas Propagat.*, Vol. 14, pp. 302-307 (1966).
- [3] A. Bossavit, "Simplicial finite elements for scattering problems in electromagnetism", *Comput. Methods Appl. Mech. Engrg.*, Vol. 64, pp. 299-316 (1989).
- [4] R. Holland, "Finite-difference time-domain (FDTD) analysis of magnetic diffusion", *IEEE Trans. Electromagnetic Compatibility*, Vol. 36, pp. 32-39 (1994).
- [5] R. J. Luebbers, F. Hunsberger and K. S. Kunz, "A frequency-dependent finite-difference time-domain formulation for transient propagation in plasma", *IEEE Trans. Antennas Propagat.*, Vol. 39, pp. 29-34 (1991).
- [6] I. Fried, "Condition of finite element matrices generated from nonuniform meshes", *AIAA Journal*, Vol. 10, pp. 219-221 (1972).
- [7] J. A. Stratton, "Electromagnetic Theory", (McGraw-Hill, 1941).
- [8] R. L. Higdon, "Absorbing boundary conditions for difference approximations to the multi-dimensional wave equation", *Math. Comp.*, Vol. 47, pp. 437-459 (1986).
- [9] R. Holland and J. W. Williams, "Total-field versus scattered-field finite-difference codes: A comparative assessment", *IEEE Trans. Nuclear Science*, Vol. 30, pp. 4583-4588 (1983).
- [10] A. K. Wong and A. R. Neureuther, "Rigorous three-dimensional time-domain finite-difference electromagnetic simulation for photolithographic applications", *IEEE Trans. Semiconductor Manufacturing*, Vol. 8, pp. 419-431 (1995).